/
Article / Book Information

（　）	
Title(English)	Studies on anisotropy in thermal expansion of isotactic polypropylene and thermoplastic elastomer blends
（　）	
Author(English)	
（　）	：　　　　　， ：　　　　， ：　6778　， ：2007　3　26　， ：　　　， ：
Citation(English)	Degree:Doctor of Engineering, Conferring organization: Tokyo Institute of Technology, Report number:　6778　, Conferred date:2007/3/26, Degree Type:Course doctor, Examiner:
（　）	
Type(English)	Doctoral Thesis

Doctoral Dissertation

Studies on Anisotropy in Thermal Expansion of Isotactic Polypropylene and Thermoplastic Elastomer Blends

Organic and Polymeric Materials

Graduate School of Science & Technology

Tokyo Institute of Technology

Michio Ono

Contents

Chapter 1 :

General introduction

1-1. Background:

It has been nearly 100 years since an automobile was born into the world. Until 1940s, automobiles had been mainly consisted of metals such as steel or aluminum. In 1950s, various types of polymers so called "plastics" were commercially available, which were adopted as one of the automobile components in the US and European countries. This trend spread over Japan as well and has been more and more accelerated from 1960s. The amount of polymers used in an automobile have showed the highest growth rate compared with other materials during the last 30 years, and have reached to about 8.0 wt% (27 vol%) in 2001 as shown in Figure 1 [1].
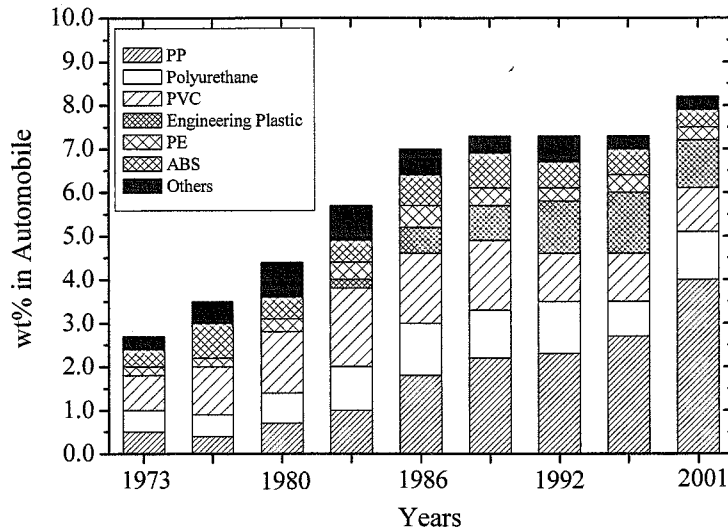
Figure 1: Weight percentage of Plastics in an automobile by the year shown

Without polymers, an automobile can't exist any more. Hence, time has come when polymers have played a leading role on the automobile materials instead of metals. Among the polymers used in an automobile, polypropylene (PP) shows the highest growth. PP takes many advantageous points over any other polymers; lower density, good mechanical properties, excellent recycle ability and suitability for environment. In terms of the forth point, CO_2 emission after combustion on the basis of density is shown in Figure 2 [2].
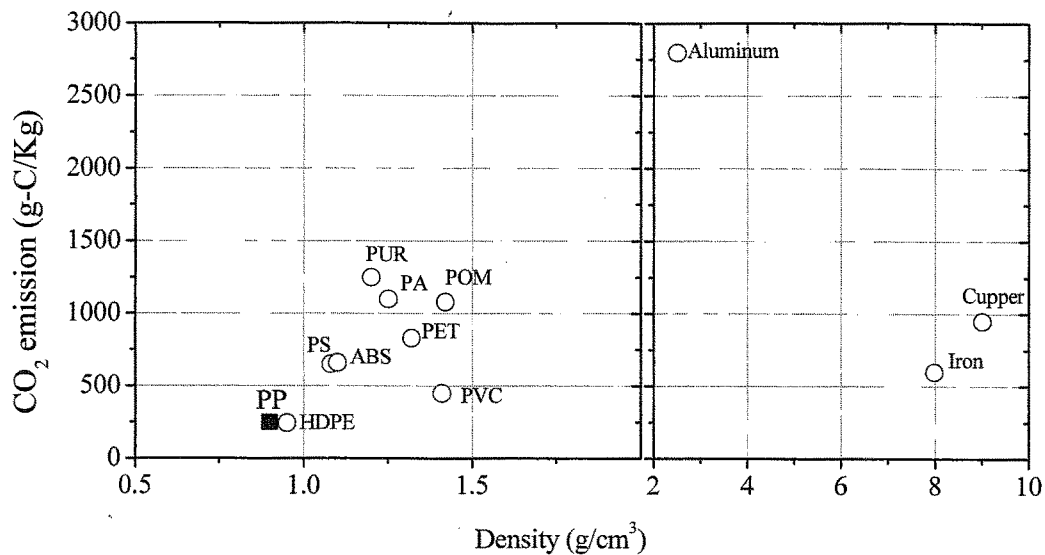
Figure 2: CO_2 emission *vs* Density for polymers

As you can see, PP is the lowest density material with the least CO_2 emission, meaning that PP is the lightest and the most environment-friendly polymer, which will be met with "protection of environment" as a social requirement.

Nowadays, trends and requirements for the PP-based parts have changed drastically. In the case of the exterior parts such as bumper fascias and fenders, they have been integrated with other small parts, thus becoming large-sized, and they have been regarded as a part of exterior panels. Hence, appearance quality as a design part, in addition to the role of the impact absorber, has been also demanded.

As for the interior parts such as instrument panels, pillar garnishes and door trims, the design complexity has been required as people's demands for the interior design have been more and more diversified. It is very difficult to fabricate the molding part

with such complicated design just in one mold. Thus it has been the conventional way to assemble small articles fabricated with different molds to finish such large and complicated part.

1-2. Motivation of this study:

Most of the PP based parts are usually in use under severe thermal conditions ranging from -50 $^{\circ}$C for the exterior parts to 100 $^{\circ}$C for the interior parts. Hence, dimensional stability under such temperature variation has been required recently. It has been well-known that the PP has a high thermal expansion ($\sim$14-15 (10^{-5} /$^{\circ}$C)) [3], compared to metal ($\sim$0.1 (10^{-5} /$^{\circ}$C)) [4] and other amorphous polymers ($\sim$7.0-9.0 (10^{-5} /$^{\circ}$C)) [3]. Because of this, a gap resulting from the dimensional mismatch between the iPP-based parts, the metal parts and/or the other assembled parts may arise toward temperature change, leading to deteriorating the appearance quality.

One of the conventional ways to solve the above issue is adding inorganic fillers with high aspect ratios (talc, glass fiber or mica) to the iPP, and suppressing bulk expansion by a simple mechanical constraint. Figure 3 shows the CLTE for various filled PP content grades.

4
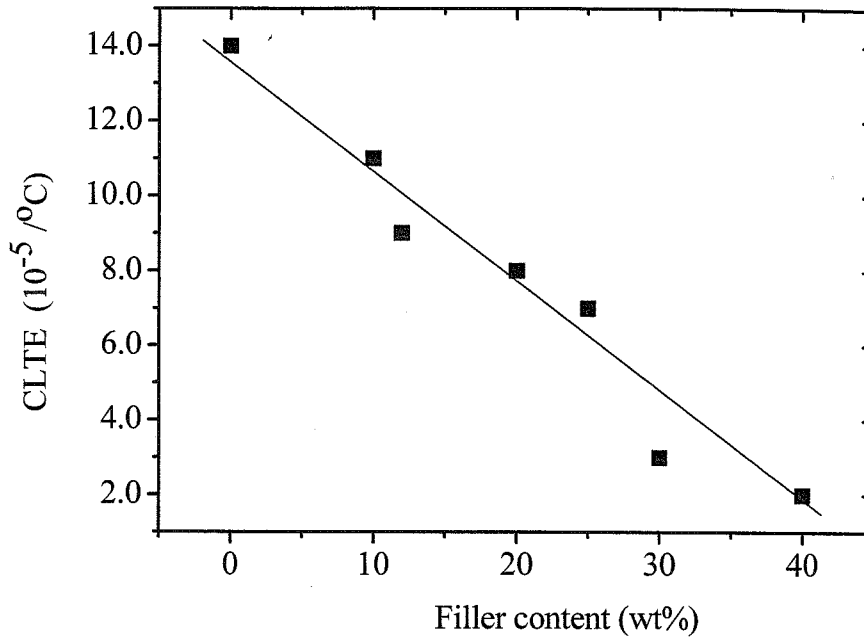
Figure 3 : CLTE as a function of filler content.

As increasing the fillers, the CLTE linearly decrease. However, incorporating the inorganic fillers has brought about worsening the car mileage resulting from the weight increase in the molded articles due to containing higher density inorganic fillers. In addition, the filler-reinforced PP is not appropriate for the environmentally-friendly material because of ash remained after combustion.

Hence, the filler-less PP compatible with the low CLTE has been extensively investigated by automobile makers and PP material suppliers.

1-3. Previous studies:

However, few studies on the CLTE control for the filler-less PP have been officially reported so far [5-8]. Yamamori *et al.* [5] firstly reported that, in the injection-molded PP and ethylene-propylene rubber (EPR) blend, the CLTE in flow direction (FD) showed a comparable value to that of the filler-reinforced PP by adjusting MFR of the EPR to be a given value. They also reported that the EPR domains were highly deformed along FD, and formed co-continuous structure with the PP matrix.

Koizumi *et al.* [6] also reported, using an injection-molded iPP/EPR system, the anisotropy in CLTEs depending on the injection directions, low CLTE in FD whereas high in ND, and highly elongated EPR domains along FD (maybe co-continuous structures). They vaguely pointed out that the driving force caused by such CLTE anisotropy was the retraction from the deformed EPR; suppression of the CLTE in FD and enhancement of the one in ND instead.

Wu *et al.* [8] also reported similar CLTE behaviors in viscosity-controlled PP/EPR systems; micro-layer structures due to the EPR domains co-continuously dispersed with the PP matrix suppressed the thermal expansion of the PP matrix along FD.

However, these previous studies reported abnormal CLTE behavior only in the case of the PP/EPR system, and the plausible factor for it was attributed only to the retraction form the deformed EPR. The retraction would be caused by either the interfacial force of molten EPR domains or the rubber elastic force of tense EPR molecules. These papers used the term "retraction" without distinguishing them. No quantitative analysis was made.

1-4. Contents of this thesis:

The author, a member of SunAllomer Ltd., has developed the filler-less PP having the low CLTE with comparable to that of metals for over 4 years. This thesis collects a part of the fundamental studies in terms of his low CLTE PP development. This thesis consists of 8 chapters including this chapter.

In Chapter 2, we will introduce abnormality of CLTE behavior for an injection-molded iPP/Poly(ethylene-*co*-octene) rubber (EOR) blend. We will report that large CLTE anisotropy is found in this system, which is closely related with the arrays of the elastomer domains and the PP crystal orientation.

In Chapter 3, three-dimensional structures of the EOR domains in the injection-molded iPP/EOR will be observed directly using a transmission electron microtomograpy (TEMT). We will discuss the correlation of the CLTE anisotropy in directions with the 3D structures of the EOR domains.

In Chapter 4, the dependence of the CLTE anisotropy on the arrays of the EOR domains will be reported. The injection-molded iPP/EOR blends with different types of the EOR shapes, lamella-like sheet, cylinder, lamella-sheet/cylinder mixture, slab and sphere are prepared, and their CLTE anisotropies are compared.

In Chapter 5, we will investigate the correlation of the CLTE anisotropy with difference in the chemical composition and co-unit content in the elastomer for injection-molded iPP/thermoplastic elastomer (TPE) blends consisting of various types of TPEs. Some ethylene-based TPEs, polyethylenes, poly(ethylene-co-propylene) rubber, poly(ethylene-co-butene) rubber and poly(ethylene-co-octene) rubber are chosen as the TPEs.

In Chapter 6, real-time morphological change with temperature variation will be observed in the iPP/EOR blends with different EOR morphology, lamella-like sheet and spherical array.

In Chapter 7, the nano-scale elastic modulus of the elastomer domains in the iPP/EOR blend will be evaluated from the force-curve by AFM, and we will discuss the correlation of it with the macro scale CLTE behavior of the blend.

1-5. References:

[1] Yasuda T.; *JETI*, 2002, **50**, 35

[2] Fujita Y.; *Mirai Zairyo*, 2005, **5**, 9

[3] Brandup J. and Immergut E.H.; *"Polymer Handbook"*, 3rd ed, Wiley, New York, 1989

[4] Ushigi H., Sato T. and Hashitani T.; *"Kagaku Binran Kisohen II"*, Maruzen, Tokyo, 1993

[5] Yamamori Y., Iwamoto K. And Miwa Y.; *JSAE Rev.*, 1991, **12**, 61

[6] Koizumi J., Okumoto T., Mizutani H. and Shichida Y.; *Seikei-Kakou*, 1994, **6**, 697

[7] Nomura T., Nishio T., Taniguchi H., Hirai I. and Hisamura N.; *Kobunshi Ronbunshu*, 1994, **51**, 505

[8] Wu G., Nishida K., Takagi K., Sano H. and Yui H.; *Polymer*, 2004, **36**, 3085

Chapter 2:

Abnormal CLTE Behavior of Injection-molded Isotactic Polypropylene (iPP) and Poly(ethylene-co-octene) Rubber (EOR) Blend

1. Introduction

Rubber toughened isotactic polypropylene (iPP) has widely been in industrial use, such as automotive, electric appliance, food packaging, films and sheet applications, due to its superior cost performance and recycling capability over other plastics [1].

In the injection-molded articles in the automobile application, iPP-based materials are subject to severe thermal conditions ranging from -50 °C for a bumper fascia to 150 °C for a fan shroud in the engine room. It has been well-known that the iPP has quite high thermal expansion coefficient (CLTE) ($\sim$14-15 (10^{-5} /°C)) [2]. Hence, dimensional mismatch between the iPP-based part and the metal or other polymers one has been critical due to the difference of the CLTE in metal ($\sim$0.1 (10^{-5} /°C)) [3] and iPP .

Incorporation of inorganic fillers with high aspect ratios into the iPP has been employed as a conventional way to cope with that issue. However, adding the inorganic fillers has brought about worsening the car mileage resulting from the weight increase of the molded article due to containing higher density fillers. In addition, the filler-reinforced iPP composites are not appropriate for the environment-friendly materials because of ash remained after combustion.

10

Despite the practical importance of CLTE in PP, few systematic studies were performed [4-11]. In particular, only limited attempts have been made so far to lower CLTE using filler-less iPP system [10-11].

In this study, the author investigated the difference in the CLTE behaviors between injection- and compression molded isotactic polypropylene (iPP) and poly(ethylene-*co*-octene) rubber (EOR) binary blend. It was found that in the injection-molded blend quite large anisotropy in the CLTE along each direction was observed; very low in both flow- (FD) and transverse-to-flow direction (TD) while quite high in normal-to-flow direction (ND).

2. Experimental

2-1. Sample preparation:

The materials used in this study were iPP from SunAllomer (2.5 dg/min of melt flow rate (MFR) at 230 °C, 98.5 % of mmmm pentad sequences determined by ^{13}C-NMR) and EOR from Dow Chemical (10.0 dg/min of MFR at 230 °C and 0.870 g/cm^3 of specific gravity). The blend of iPP/EOR with 70/30 (v/v) was prepared first by being dry-blended in presence of anti-oxidant additive (0.2 wt%) followed by being melt-blended using a twin screw extruder with 30 mm in cylinder diameter and 52.5 of L/D (TEX30α; Japan Steel Works) under the conditions with 160 °C of cylinder setting temperatures, 500 rpm of screw revolution and 30 kg/h of through-put. The resulting blend was then injection molded to obtain a slab-shaped specimen (125 (length) by 20 (width) by 3.0 (thickness) mm^3) using an injection machine at 200 °C of cylinder setting temperature. The injection rate, injection time to full-pack and the tool temperature were 40 mm/s, 2.8 s and 40 °C, respectively. The compression-molded specimen with the size

of 100 (length) by 100 (length) by 3.0 (thickness) mm^3 was obtained at 230 °C under

30MPa pressure using a hot-press machine. The directions and cross sections of both

types of the specimens are illustrated in Figure 1.
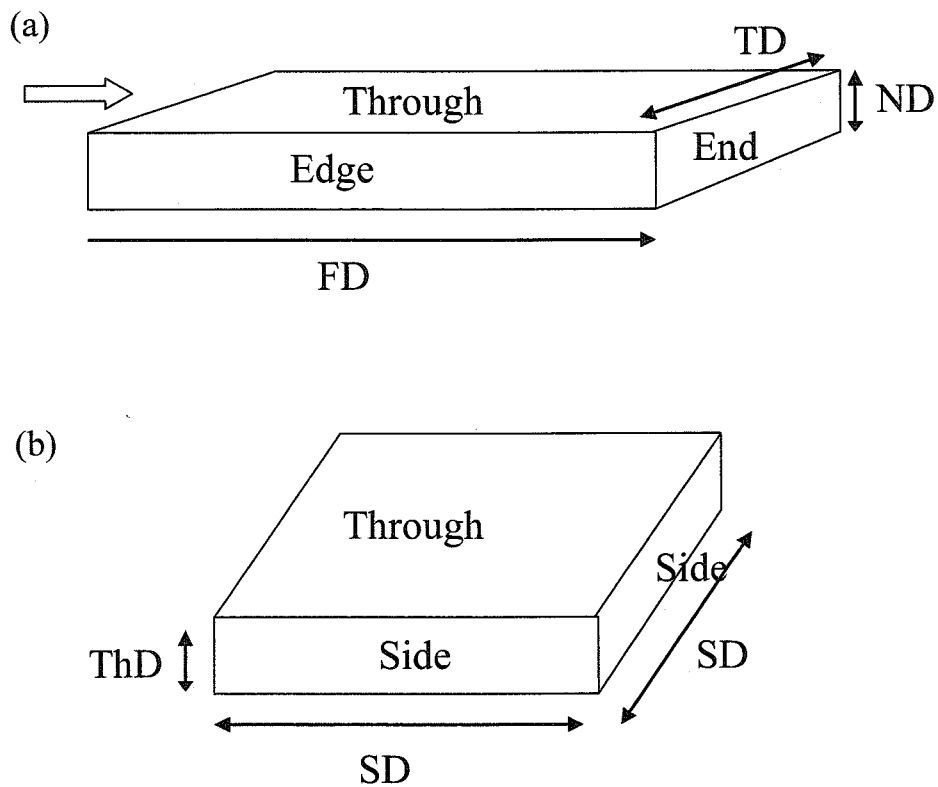
Figure 1 : Nomenclature of direction and cross section.
(a) injection-molded specimen; For directions, FD (parallel to flow
direction) , TD (transverse to flow direction) and ND (normal to flow
direction). For cross sections, Edge- (parallel to FD), End- (parallel to
TD) and Through view (parallel to ND).

(b) compression-molded specimen. For directions, SD (parallel to width
or length direction) and ThD (parallel to thickness direction). For cross
sections, Side view (parallel to SD) and Through view (parallel to ThD)

2-2. CLTE evaluation:

A specimen for the CLTE evaluation was punched out from the central part of the slab obtained; the size of the specimen was 13.0 (height) by 5.0 (length) by 3.0 (width) mm^3 for the CLTE measurement along FD, TD (injection) and SD (compression), and 3.0 (height) by 5.0 (length) by 3.0 (width) mm^3 for that along ND (injection) and ThD (compression). Each specimen was prepared so as the "length" direction can coincide with each measured direction. Note that the cross-section was adjusted to be 3.0 by 5.0 mm^2 in all cases on which the same thermal stress was imposed. The specimens were then annealed at 100 °C for 24 Hr allowing the secondary crystallization. The CLTE measurement was carried out in a compression mode at a heating rate of 4.0 °C/min using a thermo-mechanical analyzer (TMA) (MTS9000; Sinku Riko). The applied load was 0.039 N, being sufficient to ensure that the probe remains in contact with the sample and small enough to allow the compression strain to be neglected (discussed later). The CLTE was monitored as a function of temperature in three directions, FD, TD and ND for the injection-molded specimen and SD and ThD for the compression-molded one. Each measurement was independently made on a different specimen.

The CLTE (α_J) is expressed as equation (1)

$$\alpha_J = \frac{1}{Ls_J}\left(\frac{\partial L_J}{\partial T}\right)_P \tag{1}$$

where the subscript J means the directions, FD, TD and ND for the injection-molded specimen and XD and ThD for the compression-molded one. L_J is the length of J direction and Ls_J is the standard length at a reference temperature (23 °C in this work) along J direction, T is the temperature and P is pressure (atmospheric pressure in this study, thus considered to be constant throughout the measurement).

2-3. Morphological observation by TEM:

The morphologies of the edge-, end- and through-view for the injection-molded specimen and side view for the compression-molded one were observed using a transmission electron microscopy (TEM) (JEM1200EX; JEOL) operated at 120 kV of an accelerating voltage. An ultra-thin section having 70-80 nm of thickness microtomed at -100 °C was taken from the core layer of the slab after being stained with RuO_4 vapor at 35 °C for 5 hours.

2-4. iPP crystalline structure by WAXD:

The iPP crystalline structures in three cross-sections, edge-, end- and through-view for the injection-molded specimen were investigated by wide angle X-ray diffractometer (WAXD) (RAD-3X; Rigaku) in a reflection mode using Ni-filtered Cu-Kα radiation (λ=1.5418 Å) operated at 40 mA and 40kV. The X-ray incident beam was irradiated normal to each view.

3. Results and Discussion

## 3-1. Temperature Dependence of CLTE:

Figure 2(a) and (b) show the CLTE profiles of the injection-molded blend along FD, TD and ND and of the compression-molded one along XD as a function of temperature T, respectively.

In Fig. 2(a), both α_{FD} and α_{TD} increase with T with an inflection point at T~0 °C when T<50 °C, then slightly decrease when T>50 °C. On the other hand, α_{ND} increases with T at T<0 °C, and then almost levels off until 30 °C, followed by the drastic increase with T above 30 °C via an inflection at 70 °C.

At T~0 °C, the T_g of iPP, micro-Brownian motion of the iPP amorphous chains occurs, hence α_{FD} and α_{TD} increase due to the inelastic effect; the decrease in α_{ND} would be the Poisson's effect. When T>50 °C, the EOR with T_m~55 °C is in a molten state, the EOR domains thus deform so as to minimize their interfacial energy. Retraction thus takes place in both FD and TD, while expands in ND under such circumstances. Consequently, α_{FD} and α_{TD} decrease, while α_{ND} increases, when T>50 °C as observed in Fig. 2(a).

On the other hand, as for the CLTE behavior in the compression-molded specimen as shown in Fig. 2(b), α_{SD} monotonically increase with an inflection at ~65 °C. However, there has no sharp CLTE drop as observed in the α_{FD} or α_{TD}. In the case of α_{ThD}, similar CLTE behavior as that of the α_{ND} is observed, i.e., the α_{ThD} increases with T via steady state from 0 to 30 °C and an inflection point at 70 °C. The CLTE increase above 30 °C, which would enhance the α_{ThD} throughout the entire temperature range, is not as pronounced as that observed in the α_{ND}. Little anisotropy is found between the α_{SD} and α_{ThD} in this case in contrast to the injection specimen.

The deformation based on the difference in modulus between 0 and 50 °C, Δl_{load}, may underestimate CLTE. The deformation ratio, [(deformation by load)/(thermal expansion)] $= \Delta l_{load}/\Delta l_{Thermal} = (F/A(\alpha\Delta T))(1/E_{50°C}-1/E_{0°C})$, was estimated to be 2.6×10^{-3}, being negligible. In this calculation, F(applied load)=0.039 N, A(cross section)=1.5×10^{-5} (m^2), α_{FD}=5.7 (10^{-5} /°C), ΔT(temperature difference)=50 °C, $E_{50°C}$(Young's modulus at 50 °C) =300 MPa and $E_{0°C}$(modulus at 0 °C)=1,000 MPa.
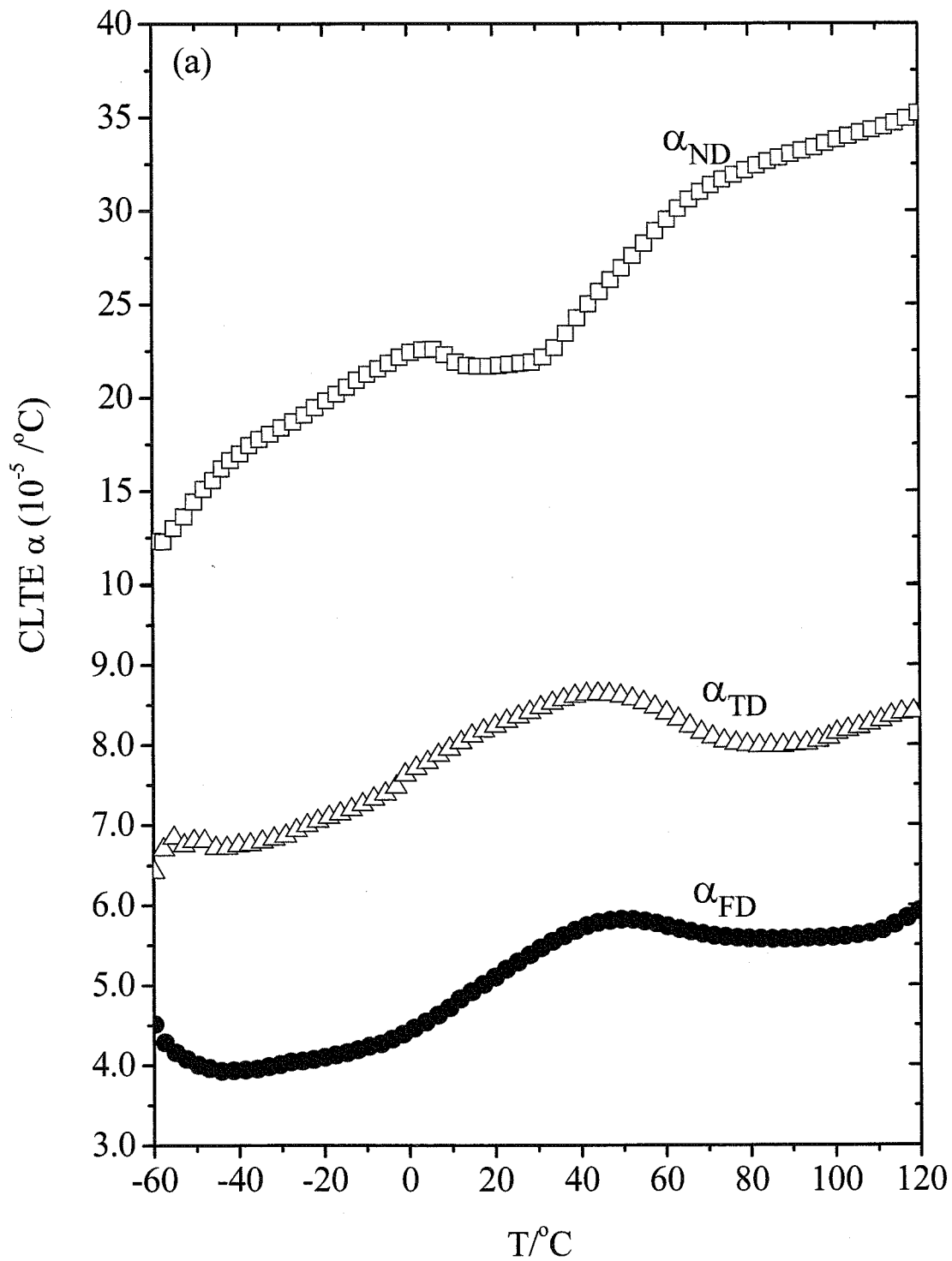
Figure 2(a) : CLTE profiles of the injection-molded specimens as a function of temperature
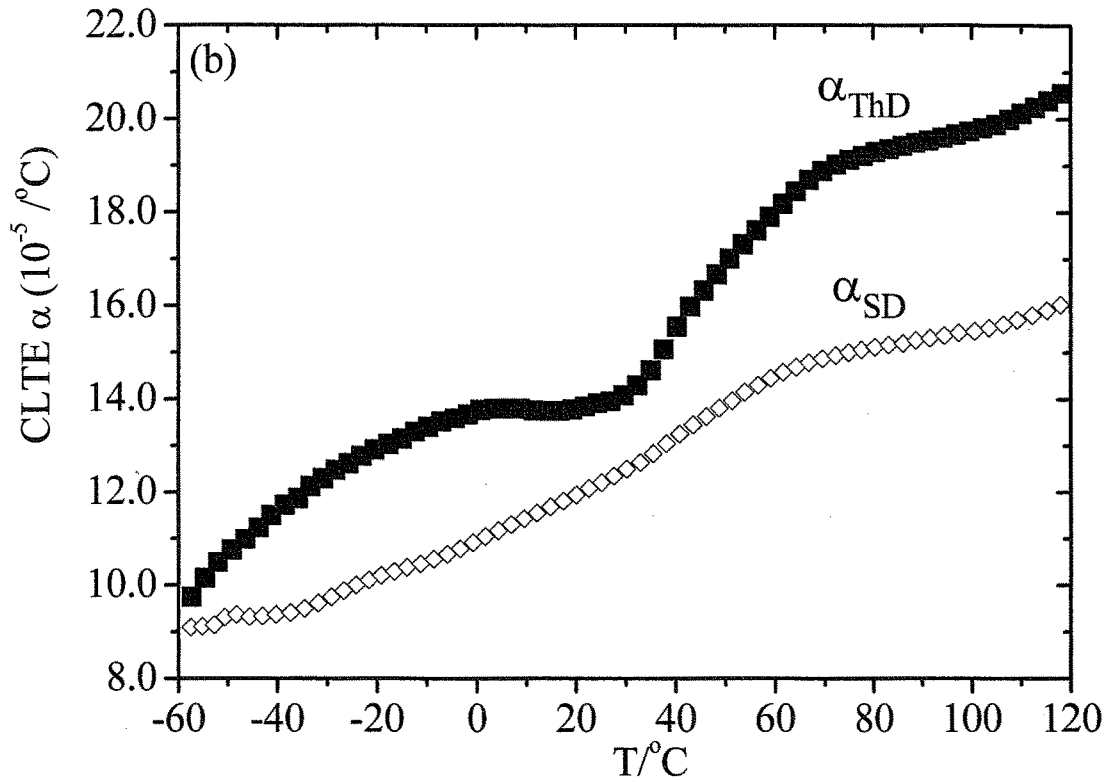
Figure 2(b) : CLTE profiles of the compression-molded specimens

It should be pointed out that the CLTE in the injection-molded specimen shows strong anisotropy on the basis of the average CLTEs of each direction, α_{FD}=5.7 (10^{-5} /°C), α_{TD}=8.2 (10^{-5} /°C) and α_{ND}=35.0 (10^{-5} /°C). It will be discussed later. On the other hand, little anisotropy is found in the CLTE in the compression-molded specimen; α_{SD}=16.0 (10^{-5} /°C) and α_{ThD}=21.0 (10^{-5} /°C).

17

3-2. TEM Observation:

Figures 3(a), 3(b) and 3(c) show TEM micrographs of edge-, end- and through-view in the injection-molded specimen, respectively. The dark- and bright region represent the elastomer (EOR) rich phase and the iPP rich phase, respectively. In both edge- and end-view, the EOR domains are highly deformed, while in the through-view, the EOR domains are disorderly located. The shape of the EOR domains is thus lamella-like sheet, the normal vector of which is parallel to ND.

TEM micrographs at a higher magnification reveal that PP crystal lamellae aligned normal to the EOR domains (Figure 4(a) and 4(b)) Rectangular pattern based on a cross-hatched structure, i.e., epitaxial growth of tangential lamellae on radial lamellae, is observed in through view (Figure 4(c)). Similar morphologies were reported in a PP/EPR/talc system [4, 12]. It should be noted that no shish-kebab structure is observed in PP crystal. Somani *et al.* showed that in isotactic PP, shish-like structure appeared under flow at a high crystallization temperature (T_c=165 $^{\circ}$C) [13], while only lamella structure was observed at lower temperature T_c=145 $^{\circ}$C [14]. In the present case, the mold temperature was 40 $^{\circ}$C. T_c would thus be <145 $^{\circ}$C, suggesting no shish-like structure.

Figures 5(a) and (b) show TEM micrograph of the compression-molded specimen at lower- and higher magnification, respectively. At lower magnification as shown in Fig. 5(a), the spherical morphology of the EOR domains was observed. The fibrous EOR shape as observed in the injection would be formed during the injection process. In the TEM micrographs at higher magnification (Fig. 5(b)), the iPP lamellae also penetrate into the EOR domains, however, no regular alignment of them along the EOR domains is observed as compared with Fig. 4(a) and (b). In other words, no anisotropy

18

of the iPP crystal would be expected in this case.
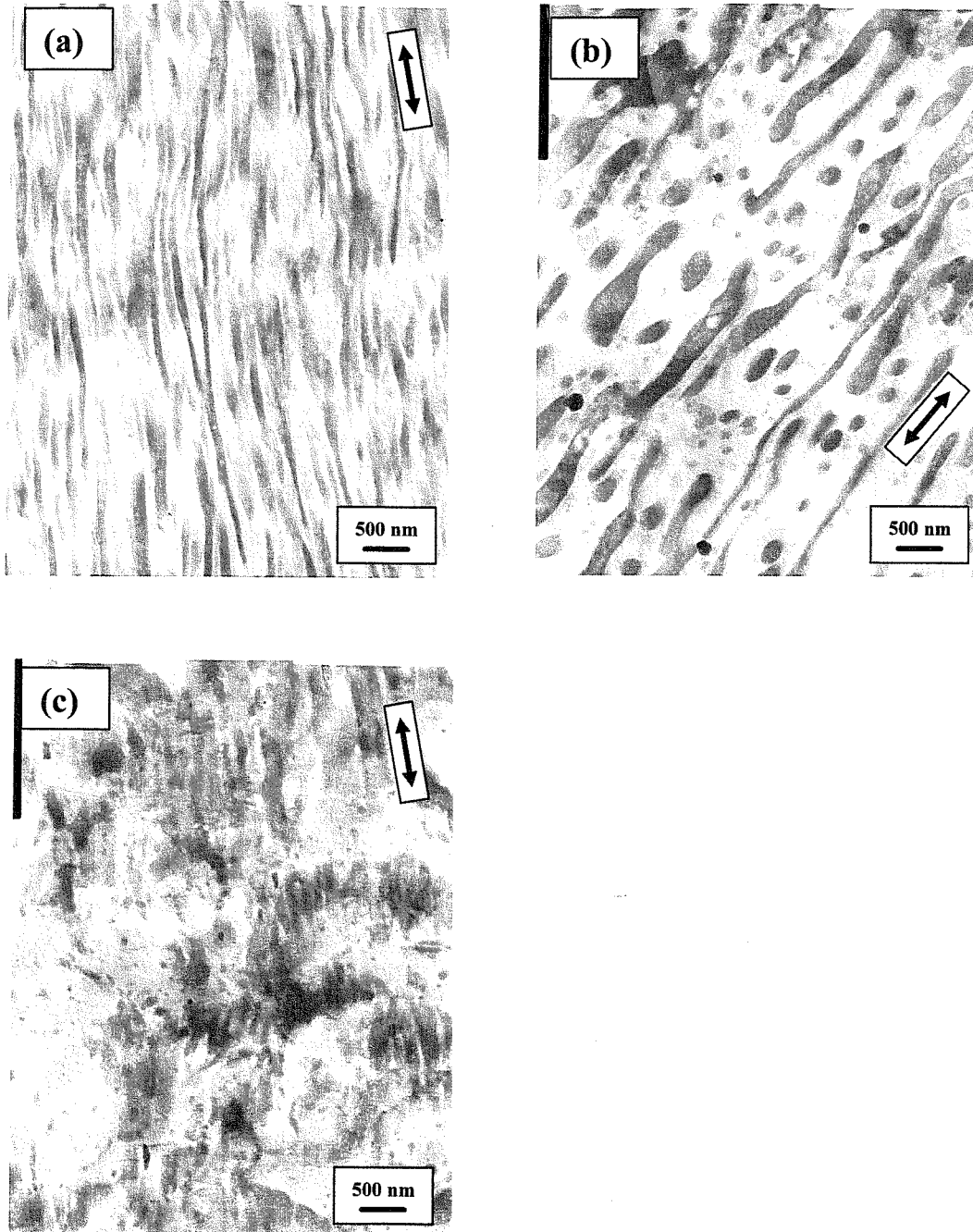
Figure 3: TEM micrographs of the injection-molded specimen
at low magnification. (a) from the edge view, (b) from the end view and
(c) from the through view, respectively.
The arrow indicates the FD in (a) and (c) and the TD in (b).
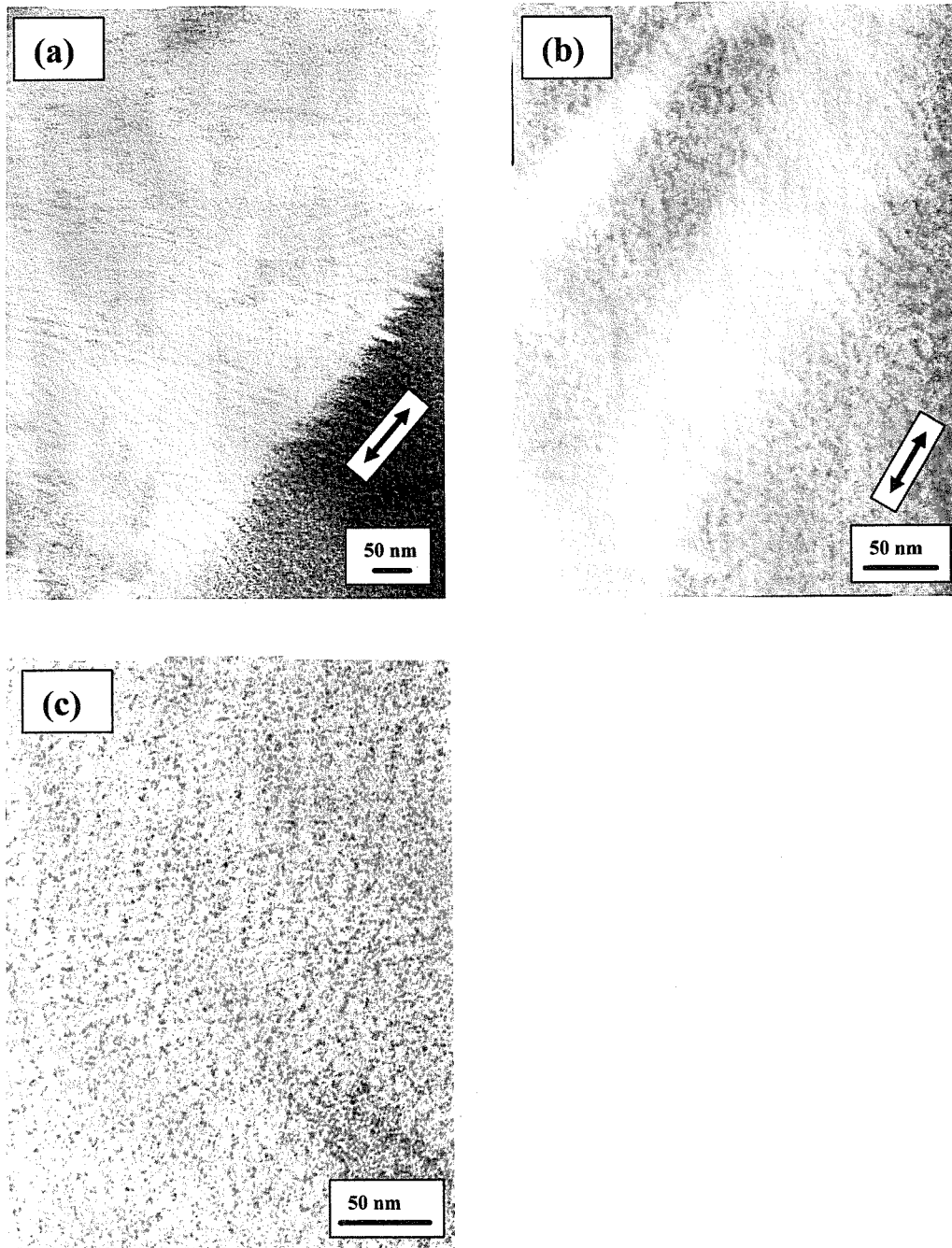
Figure 4: TEM micrographs of the injection-molded specimen at high magnification. (a) from the edge view, (b) from the end view and (c) from the through view, respectively.
The arrow indicates the FD in (a) and the TD in (b).
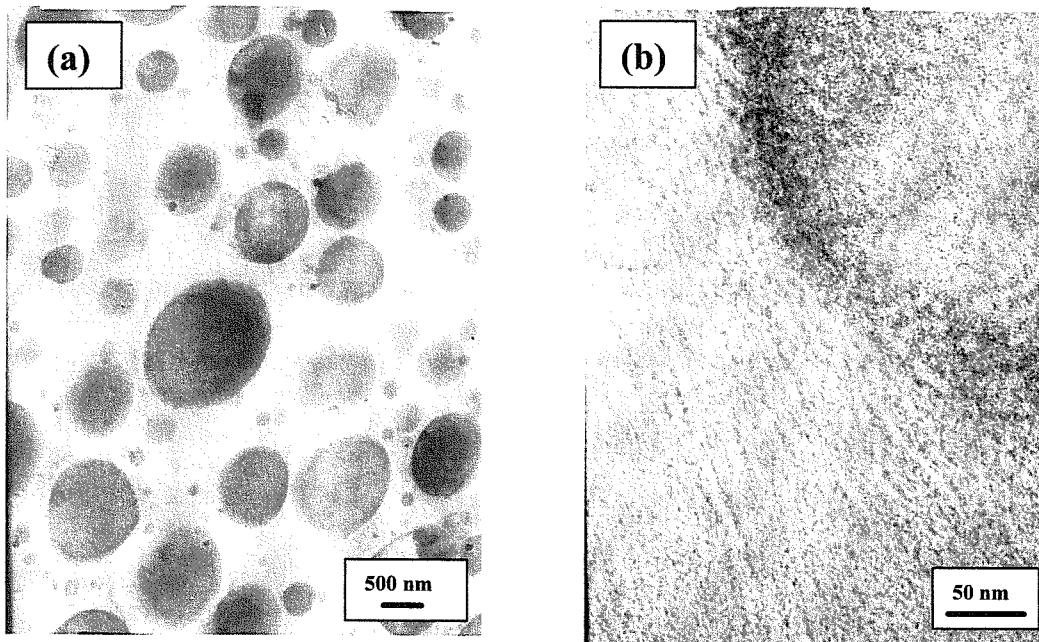
Figure 5: TEM micrographs from the side view of the compression-molded specimen at low- (a) and high magnification (b), respectively.

3-3. Anisotropy of CLTE:

The anisotropy in CLTE arises from the anisotropy in morphology as well as from that in the three components, PP (crystal and amorphous) and EOR.

The CLTE of the PP/EOR system can be given by equations (1) and (2) [15], where all components are assumed to be isotropic.

$$\alpha_{FD}(calc) = \alpha_{TD}(calc) = \frac{\alpha_{PP}E_{PP}\phi_{PP} + \alpha_{EOR}E_{EOR}\phi_{EOR}}{E_{PP}\phi_{PP} + E_{EOR}\phi_{EOR}} \tag{1}$$

$$\alpha_{ND}(calc) = (1 + v_{PP})\alpha_{PP}\phi_{PP} + (1 + v_{EOR})\alpha_{EOR}\phi_{EOR} - (v_{PP}\phi_{PP} + v_{EOR}\phi_{EOR})\alpha_{FD} \tag{2}$$

The subscripts PP and EOR represent PP and EOR, respectively. E, v and φ represent Young's modulus, Poisson's ratio, and volume fraction, respectively. Inserting α_{PP}=17.0 [16], α_{EOR}=26 (10^{-5} /$^{\circ}$C) (measured), E_{PP}=1,650 MPa, E_{EOR}=20 MPa, φ_{PP}=0.70, φ_{EOR}=0.3, v_{PP}=0.45, and v_{EOR}=0.5 into equations (1) and (2), we obtained α_{FD}(calc) (=α_{TD}(calc)) and α_{ND}(calc) to be 17.0 and 21.0 (10^{-5} /$^{\circ}$C), respectively. These results still show massive difference from those observed, suggesting that the anisotropy in PP (crystal and amorphous phases) as well as in EOR would be conceivable.

Figure 6 shows the WAXD spectra of the injection-molded specimen from the three views; egde-, end-, and through view form top to bottom, respectively. Each peak is assigned as (110), (040), (130) and (111)/(041) from lower to higher angles.

In edge view perpendicular to TD, relatively strong is the (110) peak which is related with the a-axis of iPP crystal. In the WAXD spectra form the end view perpendicular to FD, relatively strong are the (111)/(041) peaks which are correlated with the c-axis. The peak (040), relevant to the b-axis, is very strong from through view perpendicular to ND in comparison with others. It suggests that strong anisotropy in the iPP crystal axes is also found, and the a-axis, the c-axis and the b-axis would be

exclusively oriented parallel to TD, FD and ND, respectively.

Nomura *et al.* demonstrated in the PP/EPR/talc system that the b-axis of PP crystal had strong orientation along ND when the MFR ratio, MFR_{PP}/MFR_{EPR} was small, where the shapes of EPR domains were slab [4,5,12]. Diez-Gutierrez *et al.* also reported similar type of the b-axis orientation in a PP/surface treated talc system [6].

Gu *et al.* reported that the CLTE of PP crystal along the b-axis was 2.6 folds greater than that along the a-axis. Additionally, the CLTE along the c-axis was ~10% of the a-axis, and hence much smaller than that along the b-axis [17]. The CLTE of a specimen in a direction parallel to the b-axis is therefore greater than other directions, and the one parallel to the c-axis would become much smaller. In the present case, the b- axis corresponds to ND and the c-axis to FD as mentioned in the above. Indeed, Choy *et al.* reported in the stretched film PP that the CLTE showed anisotropy associated with PP crystal orientation, where the higher the draw ratio (λ) the greater the anisotropy when $\lambda < 4$ [7].

In the case of PP amorphous, the anisotropy between FD and TD (not between FD and ND) would be the largest since molecular chains (c-axis) tend to align parallel to FD under flow. In addition, EOR was observed to be isotropic ($\alpha_{FD} = \alpha_{TD} = \alpha_{ND}$) when specimens were prepared under the same conditions. Thus, the anisotropy neither in the PP amorphous phase and EOR could be operative mechanisms. The orientation of PP crystals would thus be one of the operative mechanisms for the anisotropy in CLTE ($\alpha_{ND} \gg \alpha_{TD} > \alpha_{TD}$). For more detailed analysis, precise knowledge on the orientation of PP seems to be necessary, deserving for the successive sections.
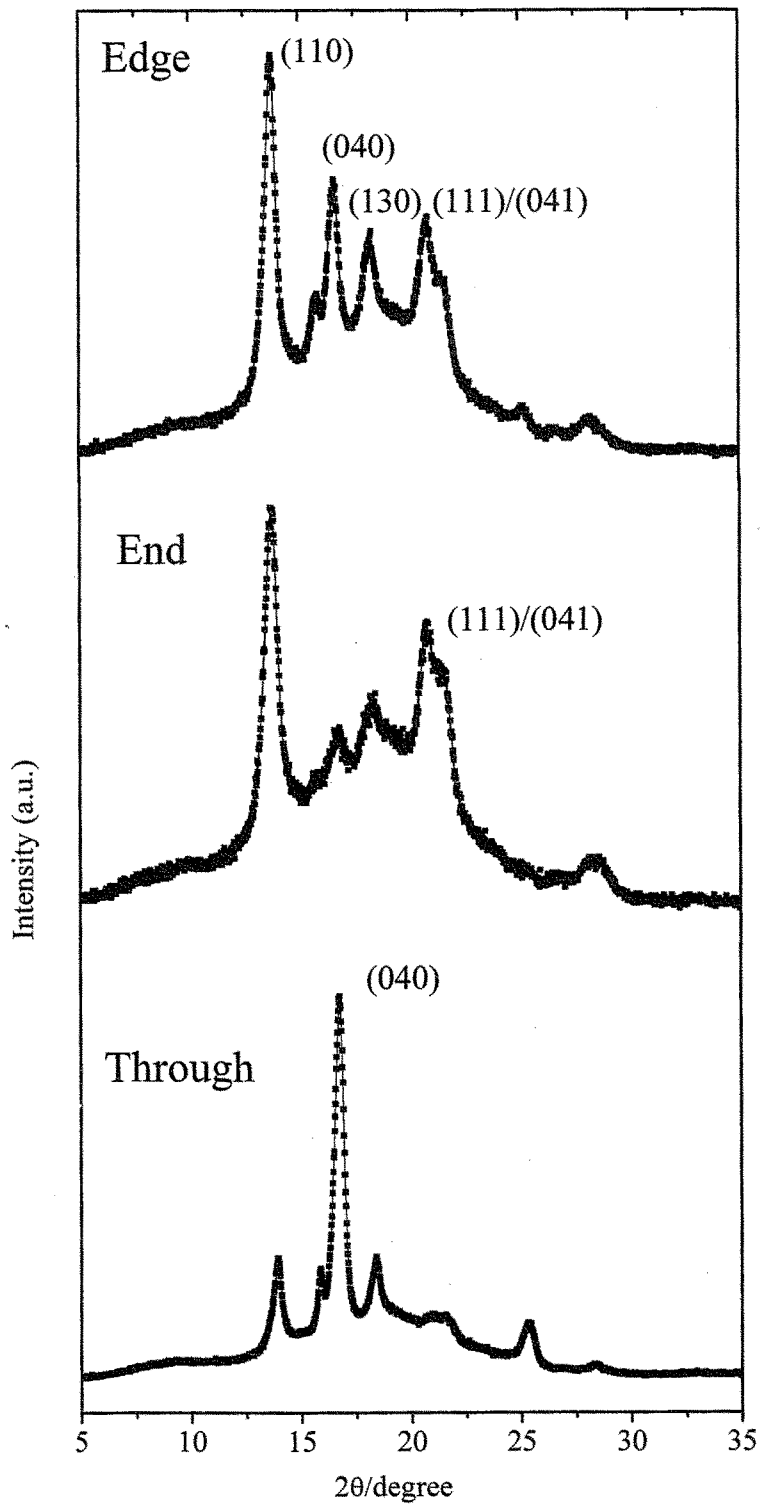
Figure 6: WAXD spectra of the injection-molded specimen from the three views.

4. Conclusions

The author investigated the linear thermal expansion coefficients (CLTE) of the specimens fabricated by both the injection- and the compression-molded polymer blend consisting of isotactic polypropylene (iPP) and poly(ethylene-*co*-octene) rubber (EOR). For the injection, the CLTE depended strongly on the directions, e.g., the CLTE in FD, TD and ND were observed to be α_{FD}=5.7, α_{TD}=8.2 and α_{ND}=35.0 (10^{-5} /°C), respectively. On the other hand, little or no anisotropy was observed in the CLTE of the compression-molded specimen.

As for the injection specimen, TEM observations revealed that the shape of the EOR domains was lamella-like sheet, the normal vector of which was parallel to ND. The anisotropy in morphology was found to account well for the largest CLTE along ND direction. In addition, WAXD analysis revealed that each crystal axis, a, b and c was oriented exclusively parallel to TD, FD and ND. Considering that the CLTE of PP crystal along the b-axis was 2.6-folds greater than the a-axis and that along the c axis was negligibly small, two conceivable mechanisms, anisotropy in morphology and PP crystal orientation, would be operative for the anisotropy in CLTE.

5. References

[1] Moore, Jr E.P.(Ed); *" Polypropylene Handbook "*, Hander, Münich, 1996

[2] J. Brandrup J. and Immergut E.H.(Eds.); *" Polymer Handbook "*, 3rd ed., Wiley, New York, 1989

[3] Ushigi H., Sato T. and Hashitani T.; *"Kagaku Binran Kisohen II"*, Maruzen, Tokyo, 1993, p17

[4] Nomura T.; *Ph.D. Thesis* Nagoya University, 1994

[5] Nomura T., Nishio T., Taniguchi H., Hirai I. and Hisamura N.; *Kobunshi Ronbunshu*, 1994, **51**, 505

[6] Diez-Gutierrez S., Rodriguez M.A., Saja J.A. and Velasco J.I.; *J. Appl. Polym. Sci.*, 2000, **77**, 1275

[7] Choy C.L., Chen F.C. and Ong E.L.; *Polymer*, 1979, **20**, 191

[8] Choy C.L., Chen F.C. and Young K.; *J. Polym. Sci.; Polym. Phys. Ed.*, 1981, **19**, 335

[9] Yamamori Y., Iwamoto K. and Miwa Y.; *JSAE Rev.*, 1991, **12**, 61

[10] Koizumi J., Okumoto T., Mizutani H. and Shichida Y.; *Seikei-Kakou*, 1994, **6**, 697

[11] Wu G., Nishida K., Takagi K., Sano H. and Yui H.; *Polymer*, 2004, **36**, 3085

[12] Nomura T., Nishio T., Tanaka H. and Mori K.; *Kobunnshi Ronbunshu*, 1995, **32**, 90

[13] Somani R.H., Yang L. and Hsaio B.S.; *Physica A*, 2002, **304**, 145

[14] Somani R.H., Yang L., Hsiao B.S. and Fruitwala H.; *J. Macromol Sci. Sci. Part B-Phys.*, 2003, **B42**, 515

[15] Shapery R.A.; *J. Composite Mater.*, 1968, **2**, 380

[16] Zoller P. and Walsh D.J.; *"Standard Pressure-Volume-Temperature Data for Polymers"*, Technomic Publishing Co., Inc., 1995

[17] Gu F., Hikosaka M., Toda A., Ghosh S.K., Yamazaki S., Arakaki M. and Yamada K.; *Polymer*; 2002, **43**, 147

Chapter 3:

Direct Observation of Three-dimensional Structures of Injection-molded iPP/EOR by Transmission Electron Microtomography (TEMT)

1. Introduction

In Chap. 2, the author described that in injection-molded iPP/EOR blend, the CLTE along each flow direction had quite different value; the lowest CLTE value along the FD and the highest along ND. By two-dimensional TEM observations from two directions, the elastomers inclusions were highly deformed both along FD and transverse-to-flow (TD) direction and co-continuously dispersed with the iPP. One of conceivable factors inducing such anisotropic CLTE behaviors would be the anisotropic morphologies of the EOR inclusions.

The EOR morphologies, dominant factor on the CLTE control, were investigated using transmission electron microscopy (TEM) in Chap. 2. In the other previous works regarding the CLTE control in iPP/Elastomer blends [1-3], TEM or scanning electron microscopy (SEM) was used to investigate the elastomer morphologies. However, the images obtained by these methods are just two-dimensional (2D) projections of the 3D morphologies. Hence, there had some uncertainty in discussing the CLTE anisotropy (3D property) on the basis of the TEM or the SEM images on each direction (2D images).

28

The advent of transmission electron microtomograpy (TEMT) has enabled us to acquire the visual information of the 3D morphologies [4-5]. TEMT uses a series of TEM micrographs taken at various tilt angles, which are reconstructed on the basis of the computerized tomography (CT) to generate 3D images. Spatial resolution of the TEMT is ca. 1 nm and the 3D images can be used to calculate quantitatively the "scattering profile" by Fourier-transformation of the images [6]. Hence it has been applied to investigate the structural analysis for polymeric materials [7-8]; the network structures for block copolymers [9-11] and the nanostructure in polymer/clay nanocomposites [12].

In this study, the author observed the 3D morphologies by TEMT for the injection-molded iPP/EOR binary blend system, which showed massive anisotropy in the CLTE along each direction described in Chap. 2. The 3D arrays and morphology of the EOR domains, which were just speculation by the TEM images taken from two cross-sections, were visually confirmed to be the stacking lamella-like sheets. Moreover, we discussed the correlation of the 3D morphology observed by the TEMT with the CLTE anisotropy.

2. Experimental

2-1. Materials and blend sample preparation:

Isotactic polypropylene (iPP)(kindly donated from SunAllomer) used in this study had zero shear viscosity at 200 °C of 56,000 Pa s, mmmm pentad sequences of 98.7 % determined by ^{13}C-NMR, a melting temperature of 165 °C determined by differential scanning calorimetry (DSC) at a scanning rate of 10 °C/min. Poly(ethylene-*co*-octene) (EOR) (purchased from Dow Chemical) having zero shear viscosity of 450 Pa s at 200

°C and melting temperature of 64 °C (broad) by DSC was used.

The blend sample consisting of iPP/EOR (70/30 (v/v) in the presence of an anti-oxidant additive (0.2 wt%) was prepared by a co-rotating twin-screw extruder with L/D of 52 (TEX30α; Japan Steel Works) under cylinder setting temperatures of 160 °C, 500 rpm of and screw rotation and throughput of 25 kg/h. It was then fabricated by the injection-molding with an injection machine (α100C; Funac) under cylinder setting temperatures of 200 °C, full-package time of 2.8 sec, and cooling temperature of 40 °C to obtain a slab used in this study.

The slab shape, the directions and the cross-sections used in this study were used as the same definition used in Chap. 2 (see Fig. 1 in Chap. 2); FD as the flow direction, TD as the transverse-to-flow direction and ND as the normal-to-flow direction and the edge view and the end view as the cross-sections parallel to FD and parallel to TD, respectively.

The thermal property of the obtained slab, which had been annealed at 100 °C overnight, was measured with DSC ranging from 0 to 230 °C. Three endothermic peaks were observed at 38, 64 (broad) and 165 °C. The peaks at 64 and 165 °C correspond to the melting point (T_m) of the EOR and the iPP, respectively. The peak at 38 °C would be considered to be the Tm of imperfect EOR crystallites thus thinner lamellae developing upon injection molding or annealing. The EOR molecules with being highly oriented along the flow direction [Fig. 3 in Chap. 2 and the TEMT results in this study] will be more easily crystallized than that without any orientation.

2-2. Transmission electron microtomography (TEMT) observation:

The ultra-thin sections for the TEMT measurement with the thickness of ca. 200 nm were prepared using a cryo-microtome at -100 °C, and then stained with RuO_4 vapor at room temperature for half an hour. The ultra-thin sections were taken from the core layer for the edge view of the slab. Hence, the TD coincided with the thickness direction of the ultra-thin section.

The TEMT observations for the edge view were carried out on a JEM2200FS (JEOL) operated at 200 kV [13]. Elastically scattered electrons from the ultra thin section were used to obtain TEM images through a magnetic prism (Ω filter). This enables us to obtain chromatic aberration-free images and thus high contrast and distinctive TEM images were obtained even at high tilt angles. For the 3D reconstruction, the 2D TEM images at various tilt angles ranging from $-58°$ to $60°$ in 1° increment were taken by a CCD camera (2048×2048 pixels) (US1000; Gatan), and then reconstructed by using a software 'Tomograpy' (JEOL). The 3D-images were presented in volume-rendered fashion.

Note that the ideal 180° range of tilt angles is required to give a perfect 3D image reconstruction. Because reconstructing the 3D image using 2D projection images taken at limited tilt angles would result in a loss of resolution and generating ghost images which never exist in the original image. To avoid them, we applied the latest signal reconstruction technique for the 3D image reconstruction in the present study, which decrease the ghost images, thus giving a high contrast 3D image [14].

In addition, during tilting the specimen, misalignment in the digitized images are also inevitable due to the imperfect eucentricity of the specimen stage. Hence, alignment of the digitized images is necessary, which was carried out by sequential

cross-correlation of the projection images obtained in this study.

2-3. CLTE evaluation:

The CLTE evaluation was carried out according as the same procedure as Chap. 2

except for the temperature ranges; -100 to 100 °C in this study.

The specimens were annealed at 100 °C for 24 Hrs to remove their thermal history and

residual stress and to enhance secondary crystallization of the iPP.


3. Results and discussion

3-1. TEMT observation:

Figures 1(a) and (b) show the 3D image obtained from the edge view; (a) the snap

shot at low magnification chosen from the movie and (b) the snap shot at high

magnification from the movie, respectively. The bright regions and the dark regions

show the EOR-rich and the iPP-rich phase, respectively. The contrast is inverted from

the original TEMT images. The definition of the axes X, Y, and Z used in the TEMT

measurement is also designated in Fig. 1(a). The Z-axis is taken parallel to TD. The FD

and ND were also designated in Fig. 1(a).

As shown in Fig. 1(a), the EOR inclusions are dispersed as co-continuous with

the iPP matrix in the XY-plane and also highly deformed along FD.

It is found that, in the XY plane, the EOR domains are highly oriented along the

FD and they stack periodically along ND. Specifically observing the Figure 1(b), the

EO domains appear to be oriented along the Z axis direction, namely to TD. The overall

morphology of the EOR sheets along TD requires the EOR sheets information outside

the Z-axis frame. Combining the 2D-TEM picture from the end view (Figure 2) with the

3D pictures (Figure 1(a) and (b)), the EOR domains outside the Z-axis frame would be expected to be also highly deformed along TD as revealed that in Figure 2, most of the EOR inclusions have fibril structures having much longer length than that in the Z-axis frame.

These results suggest that the EOR domains are periodically arranged as the lamella-like sheets stacking along ND. Such EOR arrays were more firmly speculated by the TEMT method in combination with the 2D-TEM from the end view, compared with the speculation based on the 2D-TEM pictures observed from the two cross-sections, the edge- and end view as shown in Fig. 3 in Chap. 2.
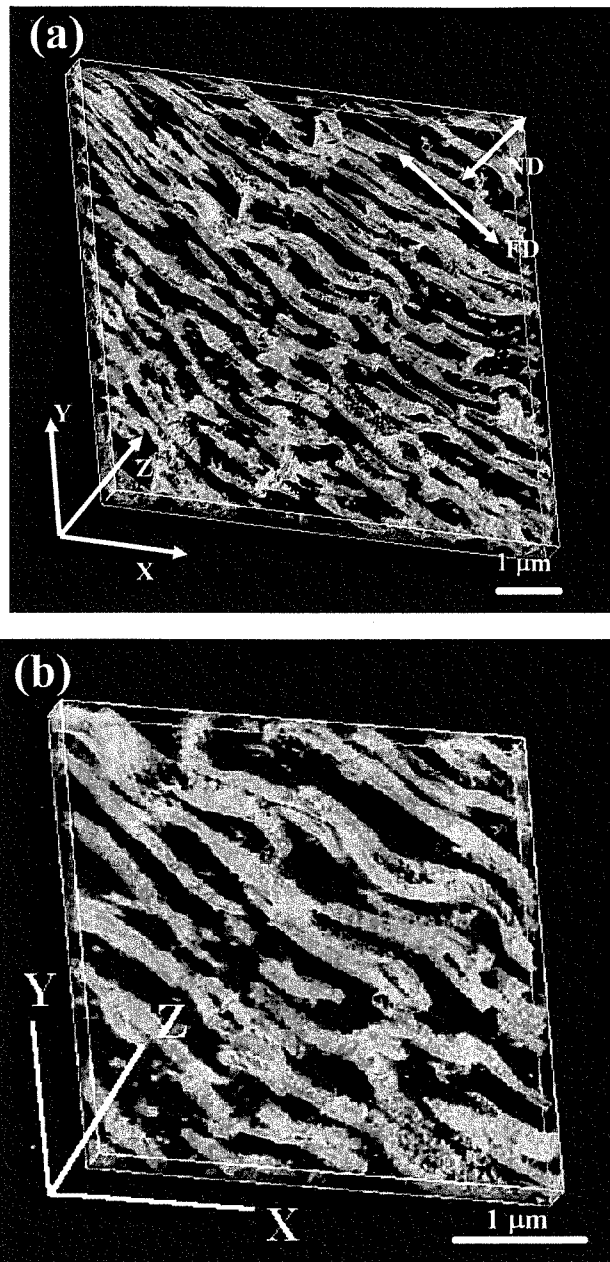
Figure 1: 3D image reconstructed as a volume-rendering.; (a) the snap shot chosen from the movie at low magnification, (b) the snap shot chosen from the movie at high magnification. The frames in the Figure 2(a) and (b) are shown in reconstructed perspective geometry, length (X-axis), width (Y-axis) and thickness (Z-axis). The Z-axis frame in Figure 2(b) is 277 nm which coincides with the thickness of the ultra-thin section. The arrows in the Figure 2(a) indicate flow direction (FD) and also normal (ND) direction. The Z-axis is taken parallel to TD, the definition of which is applied to the other Figures.
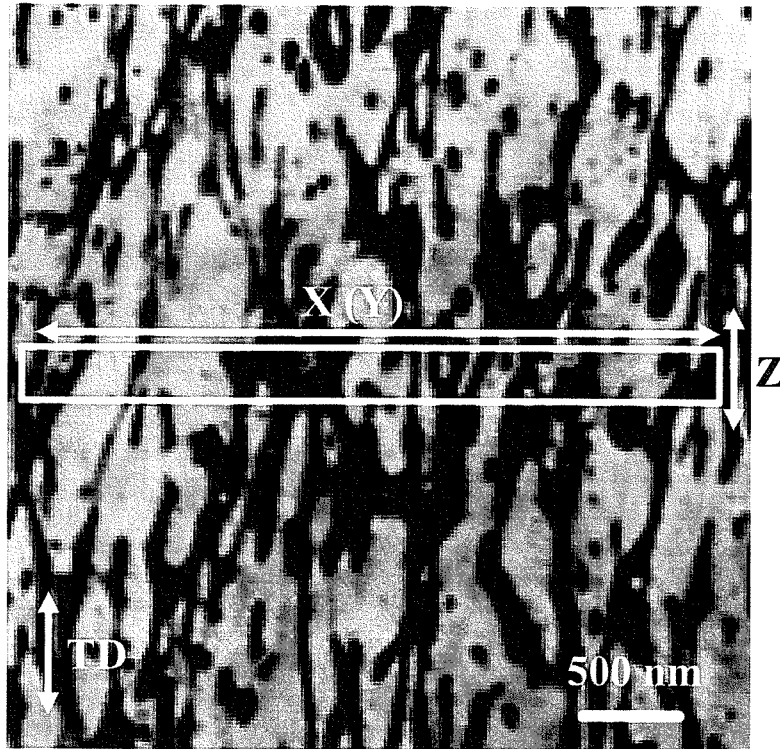
Figure 2: End-view image by 2D-TEM. The frame shown in the Figure represents XZ- or YZ- cross section.

In the XY-plane, the lamella-like sheets of the EOR domains have relatively regular intervals between the sheets and constant thickness of the sheets, indicating that the EOR domains in FD are relatively regularly arranged.

The YZ- and XZ-slice images provide information about the more detailed internal structures of TD. The YZ-slice image (Figure 3(a)) represents a view chosen from the YZ-plane movie moving along the X-direction. The XZ-slice image (Figure 3(b)) is the selected views from the XZ-plane movie along the Y-direction. In these figures, the EOR-rich phases (white regions) appear as a stripe pattern.

In Fig. 3(a), the white stripes appear at relatively regular intervals and widths, indicating that the EOR sheets are regularly arranged in the YZ-plane. However, distorted and/or thick EOR phases, the irregular intervals between the EOR sheets are often observed in the XZ-plane (Fig. 3(b)). In addition, another slice image (Figure 3(c)), a selected view of oblique cross-section along the flow direction obtained from the movie, demonstrated that the EOR domains appeared as wavy band structures.

These results suggest that the lamella-like sheets of the EOR domains don't always have a uniform shape over the entire region. Such irregularities tend to be observed more frequently in the entire TD, considering that large amount of irregular structures were observed in the EOR sheets in TD even within the Z-axis framework. By introducing the irregular EOR sheet structures observed in TD, the schematic diagram of the EOR morphology is shown in Figure 4.

In general, shear rates, temperatures and pressures applied upon molded articles will not be uniform in the entire region during injection-molding and they will be dependent on the distance from the gate and the depth from the surface [15-16]. It will induce the morphological heterogeneity; hence the structural irregularities on the lamella-sheets of the EOR domains. In addition, the principal normal stress, making the EOR domains orient along TD, tend to be much stronger than the shear stress operating along the FD upon injection-molding, which would generate more short-fibrils and/or coarse fibrils frequently observed in the TD as a result of the completion of the fibril-to-droplet transition [17-18].
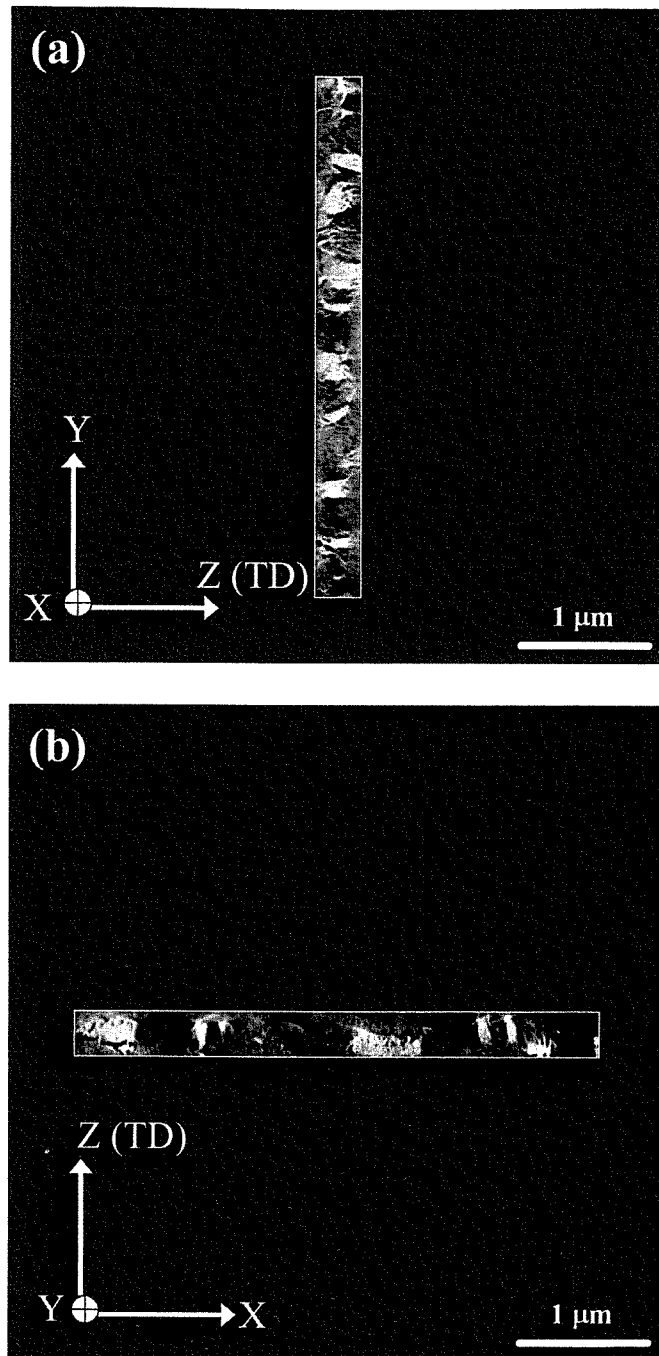
Figure 3: TEMT slice images; (a) the image chosen from the movie in the XY-plane moving along the Z-axis, (b) the image from the movie in the YZ-plane moving along the X-axis and (c) the image from the oblique slice movie moved perpendicularly to FD.
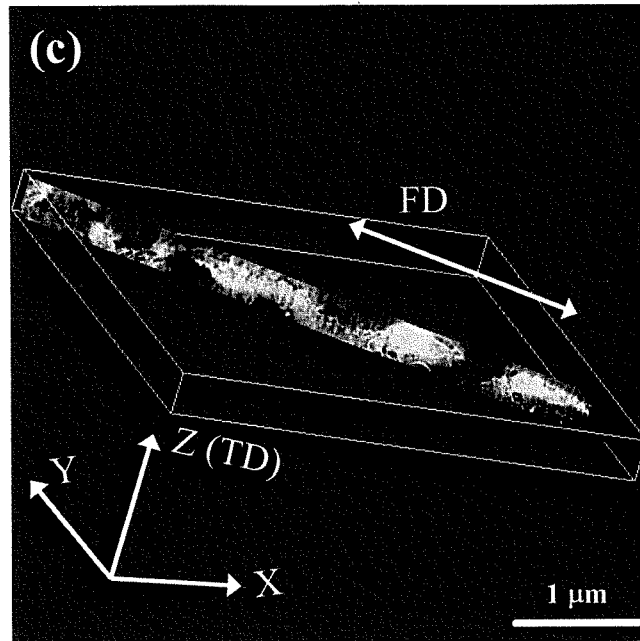
Figure 3(c): TEMT slice images; (c) the image from the oblique slice movie moved perpendicularly to FD.
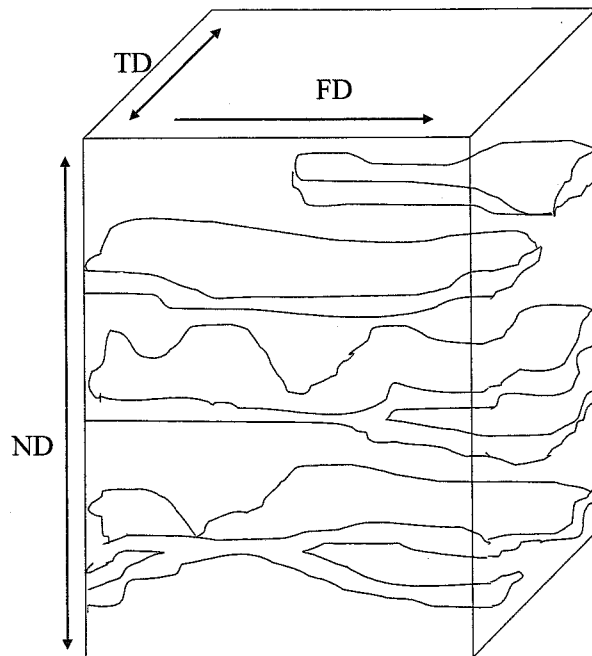
Figure 4: Schematic arrays by considering real EOR structures.

3-2. Correlation of CLTE anisotropy with irregularities in the EOR lamella-like sheets:

Figure 5 shows the CLTE profiles on FD, TD, and ND as a function of temperature. Large anisotropy in the overall values of CLTE depending on the directions, i.e., $\alpha_{ND} >> \alpha_{TD} > \alpha_{FD}$ can be clearly observed. The author have previously pointed out that the driving forces to generate such a massive anisotropy were 1) arrangement of the EOR domains with lamella-like sheets, 2) retraction of the elastomers with being highly deformed and co-continuous with the iPP [2] and 3) PP crystal orientation [3]. In this study, we focused on the investigation of the influence of the former two factors on the CLTE anisotropy.

As demonstrated in Figure 4, the EOR domains with the lamella-like sheets were arranged in parallel to both FD and TD while in series to ND. Such arrangement may result in large CLTE in ND because the total thermal strain in ND is the summation of that of each lamella-like sheet. In addition, the retraction of highly oriented EOR along both FD and TD is effective in suppressing the thermal expansion in both FD and TD while in enhancing the thermal expansion on ND.

In Figure 5, the CLTE values in FD and TD drop off sharply above 35 °C (T_m of the EOR in the blend) whereas the CLTE in ND shows a sudden upturn at this temperature, thus indicating that the lamella-like sheets arrays and the retraction by the interfacial tension of the molten-state EOR inclusions will have correlation with the CLTE anisotropies on the injection directions.

In addition, the CLTE in TD above 35 °C tends to decrease more gently than in FD, which would be ascribed to the irregularities of the thickness of the EOR sheets, namely wider distribution of the aspect ratio of the EOR sheets. The EOR sheets having

small aspect ratio (thick EOR sheets) would less contribute to the suppression of the oriented EOR domains by the retraction of the molten-state EOR sheets.

Furthermore, the irregularities of the lamella-like sheets frequently observed in TD can somewhat account for the CLTE differences in TD and FD, i.e., $\alpha_{TD} > \alpha_{FD}$. From -100 to 35 °C, the CLTE in TD always show higher value compared to that in FD and the peak at -55 °C (Tg of the EOR in the blend) is clearly observed in the CLTE profile in the FD while it is not found in TD. That would, in part, result from more frequent irregularities of the arrangement of the lamella-like sheets observed in TD, namely wider distribution of the EOR sheet arrays in the TD than that in FD.

Using the TEMT method, we could investigate the influence of the arrays and the irregularities of the EOR domains on the CLTE anisotropy in detail. However, in addition to them, the other factors, iPP crystal orientation pointed out in Chap. 2 and the tie molecules pulled out from the iPP crystalline region [19-20] will also be deeply connected with this anisotropic CLTE phenomenon. The author will now carry out the analysis of the CLTE anisotropy by introducing these factors together with the TEMT results obtained in this study. It will be reported in the future.
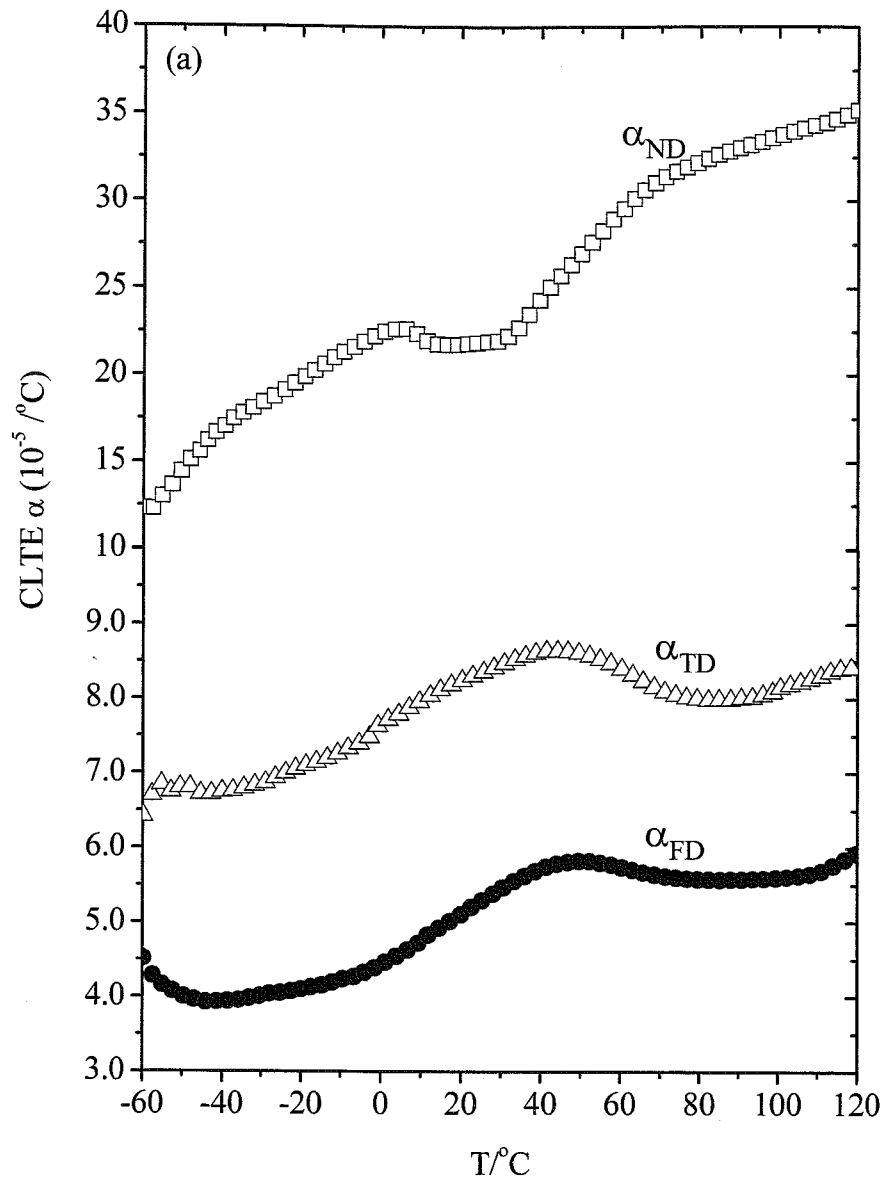
Figure 5 : CLTE profiles of the injection-molded specimens as a function of temperature

4. Conclusions

In this study, the author presented the 3D morphologies for the phase-separated structures of the injection-molded iPP/EOR binary blend. Combining the TEMT method and 2D-TEM, we confirmed that the EOR domains were highly deformed to FD as well as TD, thus forming the lamella-like sheets stacked parallel to ND, and were also dispersed co-continuously with the matrix iPP. According to the YZ-, XZ-images and the obliquely sliced image, the EOR lamellae-sheets didn't always have uniform shape over the entire region but some irregular structures; distorted shape, irregular thickness and nonuniform intervals between the EOR lamella-sheets, which were expected to be pronounced in the EOR lamella-like sheets in the TD. The presence of such irregularities caused, to some extent, the CLTE anisotropy, especially the difference for $\alpha_{TD} > \alpha_{FD}$.

5. References

[1] Yamamori Y., Iwamoto K. and Miwa K.; *JSAE Rev.*, 1995, **5**, 129

[2] Wu G., Nishida K., Takagi K., Sano H. and Yui H.; *Polymer,* **45**, 3085 (2004)

[3] Nomura T., Nishio T., Taniguchi H., Hirai I. and Hisamura N.; *Kobunshi Ronbunshu,* 1994, **51**, 505

[4] Frank J.; *"Electron tomography: three-dimensional imaging with the transmission electron microscope"*, Plenum, New York (1992)

[5] Midgley P. A. and Weyland M.; *Ultramicroscopy,* 2003, **96**, 413

[6] Jinnai H.; *"Interface in Rubber and Elastomer"*, Ed., Nishi T., CMC Pub., Tokyo (2003) p. 50.

[7] Jinnai H., Nishilkawa Y. and Nishi T.; *Kobunshi Ronbunshu,* 2005, **62**, 488

[8] Jinnai H., Nishikawa Y., Ikehara T. and Nishi T.; *Adv. Polym. Sci.,* 2004, **170**, 115

[9] Spontak R. J., Fung J. C., Braunfeild M. B., Sedat J. W., Agard D.A., Kane L., Smith S. D., Satkowski M. M., Ashraf A., Hajduk D. A. and Gruner S. M.; *Macromolecules,* 1996, **29**, 4494

[10] Spontak R. J., Williams M. C. and Agard D. A.; *Polymer,* 1988, **29**, 387

[11] Yamaguchi K., Takahashi K., Hasegawa H., Iatrou H., Hadjichristidis N., Kaneko T. and Furukawa Y.; *Macromolecules,* 2003, **36**, 6962

[12] Nishioka H., Niihara K., Keneko T., Yamanaka J., Inoue T., Nishikawa Y., Nishi T. and Jinnai H.; *Composite Interface,* in press

[13] Nishikawa Y., Jinnai H., Furukawa H. and Naruse M.; *Kinozairyo,* 2002, **22**, 11

[14] Saito T.; *"Gazou Shori Arugorizumu"*, Kindai Kogakusha, Tokyo (1993)

[15] Jang B.Z., Uhlmann D.R. and Vander Sande J.B.; *Polym. Eng. Sci.,* 1985, **25**, 64

[16] Karger-Kocsis J. and Cskai I.; *Polym. Eng. Sci.,* 1987, **27**, 241

[17] Vadas E.B., Goldsmith H.L. and Mason S.G.; *Trans. Soc. Rheol.,* 1976, **20,** 373

[18] Han C.D. and Kim Y.W.; *Trans. Soc. Rheol.,* 1975, **19,** 245

[19] Choy C.L., Chen F.C. and Young K.; *J. Polym. Sci.: Polym. Phys. Ed.,* 1981, **19,** 335

[20] Choy C.L., Chen F.C. and Ong E.L.; *Polymer,* 1979, **20,** 1191

6. Acknowledgement

Chapter 4:

Difference in CLTE Anisotropy by Shapes and Arrays of Elastomer Domains in Injection-molded iPP/EOR Blends

1. Introduction

The author pointed out that, in the injection-molded iPP/EOR blends, the CLTE anisotropy was greatly dependent on the arrays and shape of the EOR domains and on the iPP crystal orientation induced by the EOR deformation during injection-molding.

Nomura *et al.* [1] pointed out in PP/EPR/talc system that the retraction force of EPR domains contributed to the reduction in CLTE in FD, and hence would increase the CLTE in ND. They also pointed out that the PP crystal orientation was important to control CLTE. Recently Wu *et al.* reported that the injection-molded specimen with iPP/EPR blend systems showed quite large anisotropy in CLTE [2]; note that no talc was added. They suggested that the driving force on the anisotropy was assigned to be the thermal deformation of EPR domains forming co-continuous micro-layers in iPP near the skin portion of specimens.

These reports including the author's one focused on the CLTE control and its conceivable mechanism in the iPP/elastomer blends with highly deformed elastomer co-continuously dispersed with the iPP matrix. No reports on the relationship of the CLTE anisotropy with other morphology in the elastomer domains were made so far.

This study focuses on the correlation of the CLTE anisotropy with the influence

of morphology of elastomer domains which are changed purposely as being spherical, fibrous and lamella-like. In addition, the PP crystal orientation and retraction effect on the anisotropy in the CLTE are investigated.

2. Experimental

2-1. Materials:

Isotactic polypropylenes (iPP) and poly(ethylene-*co*-octene) rubber (EOR) used in this study were from SunAllomer and from Dow Chemical, respectively. The structural and rheological properties are listed in Table I. For determining the zero-shear viscosity listed in the table, the author conducted steady shear measurements at 220 °C and the shear rate range from 0.01 to 50 s^{-1} by a dynamic mechanical spectrometer (ARES; Rheometric Scientific) using parallel-plate fixture with 25 mm in diameter and 1 mm in gap height; the zero-shear viscosity η_0^* of each raw material was determined as the complex viscosity η^* with remaining nearly constant at low shear rate. The specimens with 1 mm thickness used for the viscosity determination were fabricated by compression-molding at 230 °C.

Five binary blends, PP-1/EOR, PP-2/EOR, PP-3/EOR iPP-4/EOR and iPP-5/EOR consisting of 70/30 of iPP/EOR (vol/vol) were prepared by using a co-rotating twin-screw extruder (KTX-30; Kobe Steel) at 160°C. The characterization of the blends was summarized in Table II.

Each blend was injection-molded to obtain a slab (125 (length) × 20 (width) × 3.0 (thickness) mm^3) using an injection molding machine (Fanuc α100C; Fanuc) at 200°C. The injection rate, injection time to full-pack and the tool temperature were 40 mm/sec, 2.8 sec and 40 °C, respectively. The author used the same definition of the directions

and cross-sections in this section as those in Chap. 2 (see Fig. 1 in Chap. 2).

The crystallinity of the iPP and each blend were determined using the heat of fusion per gram divided by that of perfect crystalline iPP, 209 J/g [3]. The heat of fusion and melting temperatures (T_m) were measured with a differential scanning calorimeter (DSC) (DSC-7; Perkin Elmer) at a scanning rate of 10 $^\circ$C/min.

Table I Sample information of raw materials

Sample designation	Types of Polymers	MFR[1] (dg/min.)	Flexure modulus (MPa)	Tm (°C)	Crystallinity (%)	zero-shear viscosity (Pa-s)
iPP-1	Isotactic PP	0.35	1,600	166.0	51.2	12,700
iPP-2	Isotactic PP	2.5	1,650	165.5	47.2	5,600
iPP-3	Isotactic PP	30	1,700	163.9	51.3	497
iPP-4	Isotactic PP	70	1,700	163.4	53.2	150
iPP-5	Isotactic PP	800	1,770	161.9	48.7	36
EOR	Poly(ethylene-co-octene)	10	20	55.3	n.d.[2]	455

1) measured at 230°C.
2) Negligibly small

48

Table II Sample information for blends

Sample designation	Viscosity Ratio	Tm (°C)	Crystallinity (%)
PP-1/EOR	0.036	165.2	35.5
PP-2/EOR	0.081	164.2	34.3
PP-3/EOR	0.92	164.9	35.2
PP-4/EOR	3.0	164.7	35.2
PP-5/EOR	13	161.0	36.1

2-2. Linear thermal expansion coefficient (CLTE):

The CLTE evaluation in this study was carried out according as the similar procedures described in Chap. 2 except for the CLTE definition and measured temperature range (23 to 100 °C in this study).

The CLTE (α^{obs}_J) in this study was calculated by equation (1)

$$\alpha^{obs}_J = \frac{1}{L_1} \frac{L_2 - L_1}{T_2 - T_1} \qquad (1)$$

where, L_1 is the length at T_1 (T_1=23 °C in this work) and L_2 is the length at T_2 (T_2=100°C). The subscript J means the directions, FD, TD and ND.

2-3. Morphology observation:

An ultra thin section (thickness; 50-60 nm) was microtomed in edge-, end- and through-views at -100 °C; the thin section was obtained form the core layer for each specimen after being stained in RuO_4 aqueous solution (0.5 wt%) at room temperature for over 24 hours. The morphology was observed by transmission electron microscopy (TEM) (JEM1200EX; JEOL) operated at 120 kV.

2-4. PP crystal orientation by WAXD:

Wide angle X-ray diffractometer with a pole figure attachment (WAXD)(RAD-3X; Rigaku) using Ni-filtered Cu-Kα radiation (λ=1.5418 Å) operated at 40 mA and 40 kV was used to investigate the crystalline orientation of PP. The reference axis was chosen to FD. The samples were sliced to 1mm thickness by removing skin layers and mounted on a sample holder so that FD in the sample coincide with the vertical axis in the pole figure. Accordingly, TD and ND in the sample coincide with transverse- and normal direction in the pole figure, respectively. Two angle scannings, polar angle (α), and azimuthal angle (β), were made. The transmission mode scanning was made with the α ranging from 0 to 40 ° and the β ranging from 0 to 360 °, and the scans in the reflection mode were carried out with the α from 40 to 90 ° and the β from 0 to 360 °. The angular step of 5 ° was performed or α and the β scanning was made at a scan speed of 180 ° or both diffraction modes.

The mean square co sine $<\cos^2\phi_{c,J}>$, $<\cos^2\phi_{a,J}>$ and $<\cos^2\phi_{b,J}>$ which were evaluated using the diffraction from (040) (2θ=16.9 °) and (110) (2θ=14.1 °) planes where $\phi_{040,J}$ (or $\phi_{110,J}$) is the angle between the normal of (040) plane (or (110) plane) and J direction [4]. The Herman's orientation function for each a-, b- and c-axis, i.e., f_a,

f_b and f_c was then determined by the following equations [5]

$$f_{p,J} = \frac{3 < \cos^2 \phi_{p,J} > -1}{2} \tag{2}$$

$$f_{p,FD} + f_{p,TD} + f_{p,ND} = 0 \tag{3}$$

where p is the crystallographic axis (p=a,b and c).

2-5. CLTE of PP crystal axes:

The lattice spacing as a function of temperature was measured by WAXD equipped with a thermocouple. The measurement was carried out at 23 °C and 100 °C. The sliced specimen used in the section 2.4 was mounted on the holder with X-ray exposure parallel to the through view, and warmed up to the testing temperature and held at each testing temperature for 10 minutes prior to X-ray exposure. Using a goniometer, a 2θ sacn in the range from 5-35 ° was carried out in the reflection mode at a scan rate of 2 °/min.

The α-form PP crystal has a monoclinic crystal structure and showed five strongest reflections 110, 040, 130, 111 and 131 in the WAXD measurement. The lattice constants, a, b, c, and β were determined.

The CLTE ($\alpha^{cr}{}_X$) of the lattice constant was defined viz equation (4)

$$\alpha^{cr}{}_X = \frac{1}{X_1} \frac{X_2 - X_1}{T_2 - T_1} \tag{4}$$

where X denoted lattice constant a, b and c, X_1 and X_2 denoted the lattice constant at T_1 (T_1=23 °C in this work) and T_2 (T_2=100 °C), respectively.

3. Results and Discussion

3-1. Influence of viscosity ratio on CLTE:

Figure 1 shows the CLTEs along FD, TD and ND directions (designated as α^{obs}_{FD}, α^{obs}_{TD} and α^{obs}_{ND}) as a function of a viscosity ratio of EOR to iPP, $\eta_0^*(EOR)/\eta_0^*(iPP)$. It is found that the α^{obs}_{FD} and α^{obs}_{TD} increased, while the α^{obs}_{ND} decreases as the viscosity ratio increases except for the iPP-1/EOR blend. In addition, the anisotropy becomes stronger when the viscosity ratio is smaller as demonstrated in the PP-2/EOR system. In the case of the iPP-1/EOR blend having the smallest viscosity ratio, however, the CLTEs of both FD and TD are higher and that of ND lower compared with the CLTEs of the iPP-2/EOR blend having the higher viscosity ratio. It will be discussed in the following chapter.

The volumetric thermal expansion (CVTE) obtained by the summation of α^{obs}_{FD}, α^{obs}_{TD} and α^{obs}_{ND} is 56, 60, 62, 48 and 53 (10^{-5} /°C) for iPP-1/EOR, iPP-2/EOR, iPP-3/EOR, iPP-4/EOR and iPP-5/EOR, respectively. It should be pointed out that small difference in the CVTE among the blends is found despite the massive difference in the CLTE in FD, TD and ND. Wu *et al.* also reported the variation in CVTE to be small even when anisotropy was large [2]. The present observation is thus in accordance with the results by Wu *et al.*.
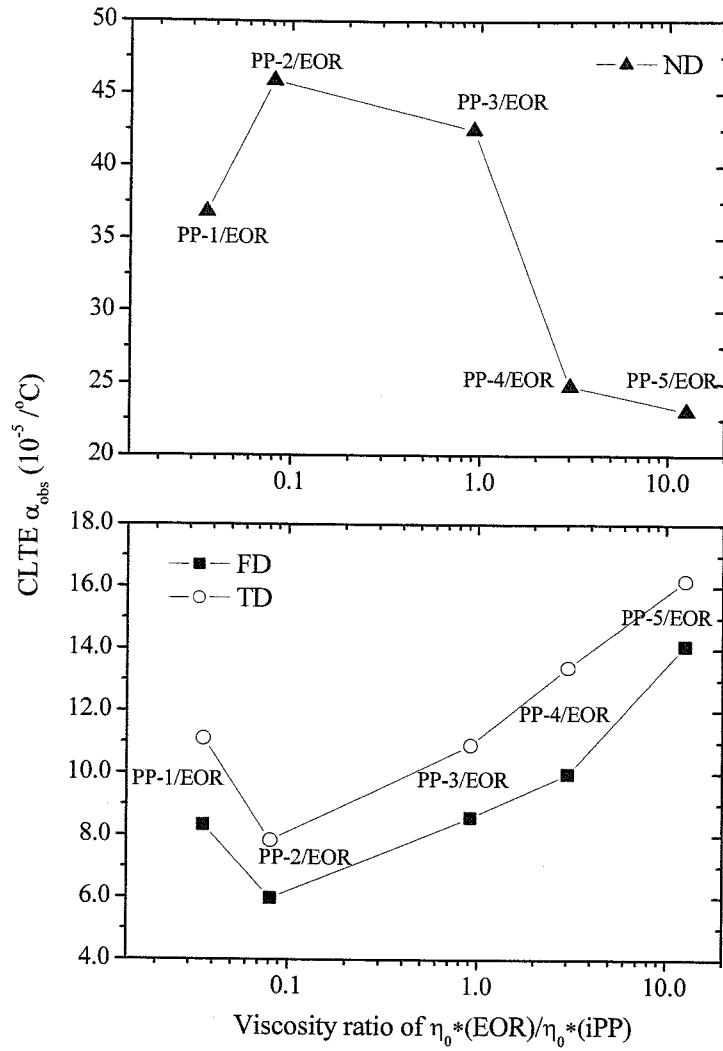
Figure 1: CLTE values from three directions, FD, TD and ND as a function of viscosity ratio.

3-2. Morphology observation by TEM:

(1) iPP-1/EOR

Figures 2(a) and (b) show TEM micrographs at low magnification of edge- and end-view for PP-1/EOR, respectively. The dark and bright phases indicated EOR-rich and iPP-rich phases, respectively. The EOR domains are observed as rod-shaped grains both from the edge- and end-view, thus the shape of the EOR domains would be a slab.

(2) iPP-2/EOR

Figures 3(a) and (b) show TEM micrographs at low magnification of edge- and end-view for PP-2/EOR, respectively. The EOR domains, in this case, are found to be highly deformed, being fibrous in shape both along FD and TD, thus the EOR domains would be lamellae-like sheets in shape stacked normal to ND.

Figures 3(c)-(e) show high magnification TEM photographs from the edge-, end- and through-view, respectively, giving the iPP lamellae structures. The iPP crystal is found to be oriented normal to the EOR domain as observed in Fig. 3(c) and (d). The cross-hatching structure as a result of tangential lamellae epitaxially grown onto radial lamellae is observed in Fig. 3(e). These observations suggest that epitaxial growth of PP crystals based on the EOR phase. Such a pillar structure was also reported in PP/EPR/talc systems [6]. The PP crystal orientation in the PP-2/EOR system would thus be strong.

(3) iPP-3/EOR

The low magnification TEM photographs are shown in Figure 4(a) (edge-view) and 4(b) (end-view), respectively. The fibrous EOR is observed along FD and TD as

seen in the iPP-2/EOR blend system. However, ellipsoid-shaped grain is sporadically observed in the end-view (parallel to TD), thus the shape of EOR domain would be the mixture of lamellae-like sheet and cylinder.

(2) iPP-4/EOR

Figures 5(a)-(c) show TEM micrographs of edge- and end-view for iPP-4/EOR, respectively. The images of the EOR domains in edge- and end-views are found to be fibrous and circular, respectively, indicating that the shape of the EOR domains would principally be cylindrical. It should be noted that slab-like domains of EOR are also observed sporadically as shown in Fig. 5(c) (end-view).

Figures 5(d) and (e) show TEM micrographs at higher magnification of edge-and end-view for PP-4/EOR, respectively. As similar to the PP-2/EOR system, the PP lamellae are found to be oriented normal to the EOR domain in the edge-view as observed in Fig. 5(d), while in the end-view, the PP lamellae penetrate randomly into EOR domains (see Fig. 5(e)). The PP crystal orientation in the PP-2/EOR system would thus be weaker than that in PP-2/EOR system.

(3) iPP-5/EOR

Figures 6(a) and (b) show TEM micrographs of edge- and end-view for PP-5/EOR, respectively. The images of the EOR domains in edge-and end views are found to be circular in all directions, indicating that the shape of the EOR domains would be spherical (ellipsoid).

Figures 6(c) and (d) show TEM micrographs at higher magnification of the edge-and end-view, respectively. As similar to the iPP-4/EOR in the end-view as seen in Fig.

55

5(e), the iPP lamellae are found to be penetrated randomly into the EOR domains. The PP crystal orientation in the PP-5/EOR system would thus be random.

More detailed study on the PP crystal orientation will be made using X-ray diffraction method in the following section.

As a result, the arrays of the EOR domains vary with the viscosity ratio (λ) of EOR to iPP as the slab for the iPP-1/EOR, the lamella-like sheet for the iPP-2/EOR, the mixture of the slab and cylinder for the iPP-3/EOR, the cylinder for the iPP-4/EOR and the sphere for the iPP-5/EOR, respectively in the ascending order of λ. Therefore, one of the factors giving rise to the CLTE anisotropy of each blend along the directions, which is greatly dependent on λ, would be the differences of the arrays of the EOR domains. In addition, the lamella-like sheet arrays of the EOR domains would induce the biggest CLTE anisotropy, suppressing the CLTE both in FD and TD and enhancing the one in ND.
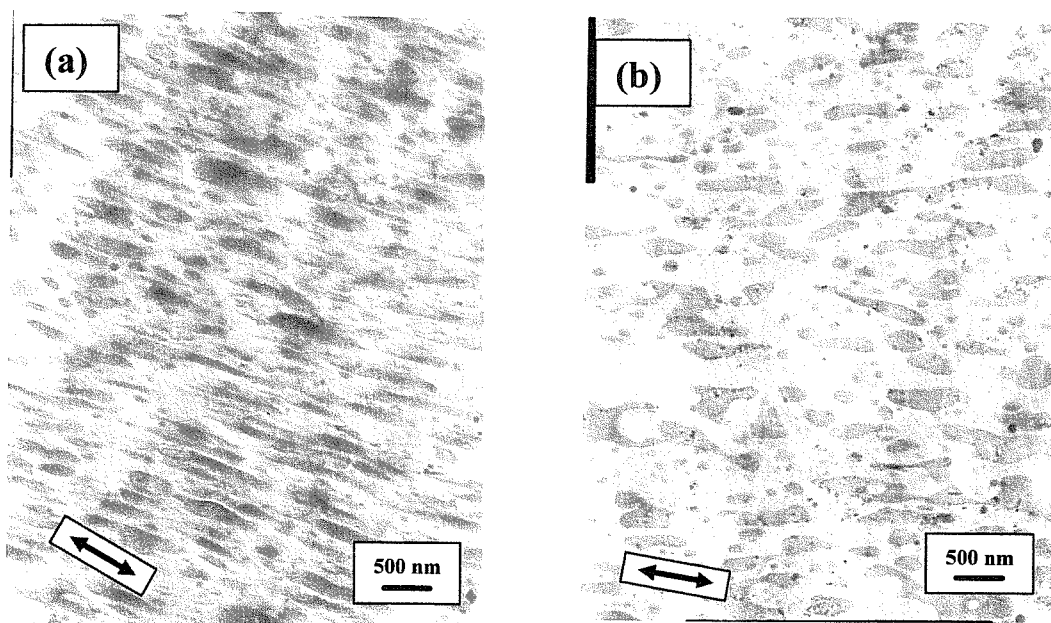
Figure 2: TEM micrographs of the PP-1/EOR blend at low
magnification. (a) from the edge view and (b) from the end
view, respectively. The arrow indicates FD in (a) and TD
in (b).
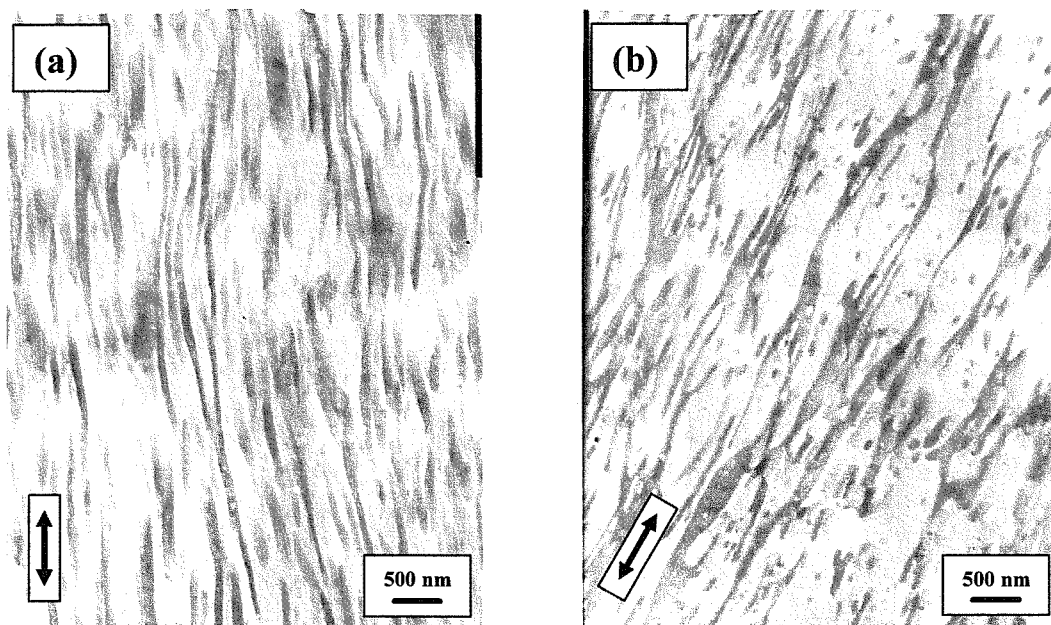
Figure 3: TEM micrographs of the PP-2/EOR blend; (a) from
the edge view and (b) from the end view at low
magnification, respectively. The arrow indicates FD in (a)
and TD in (b).
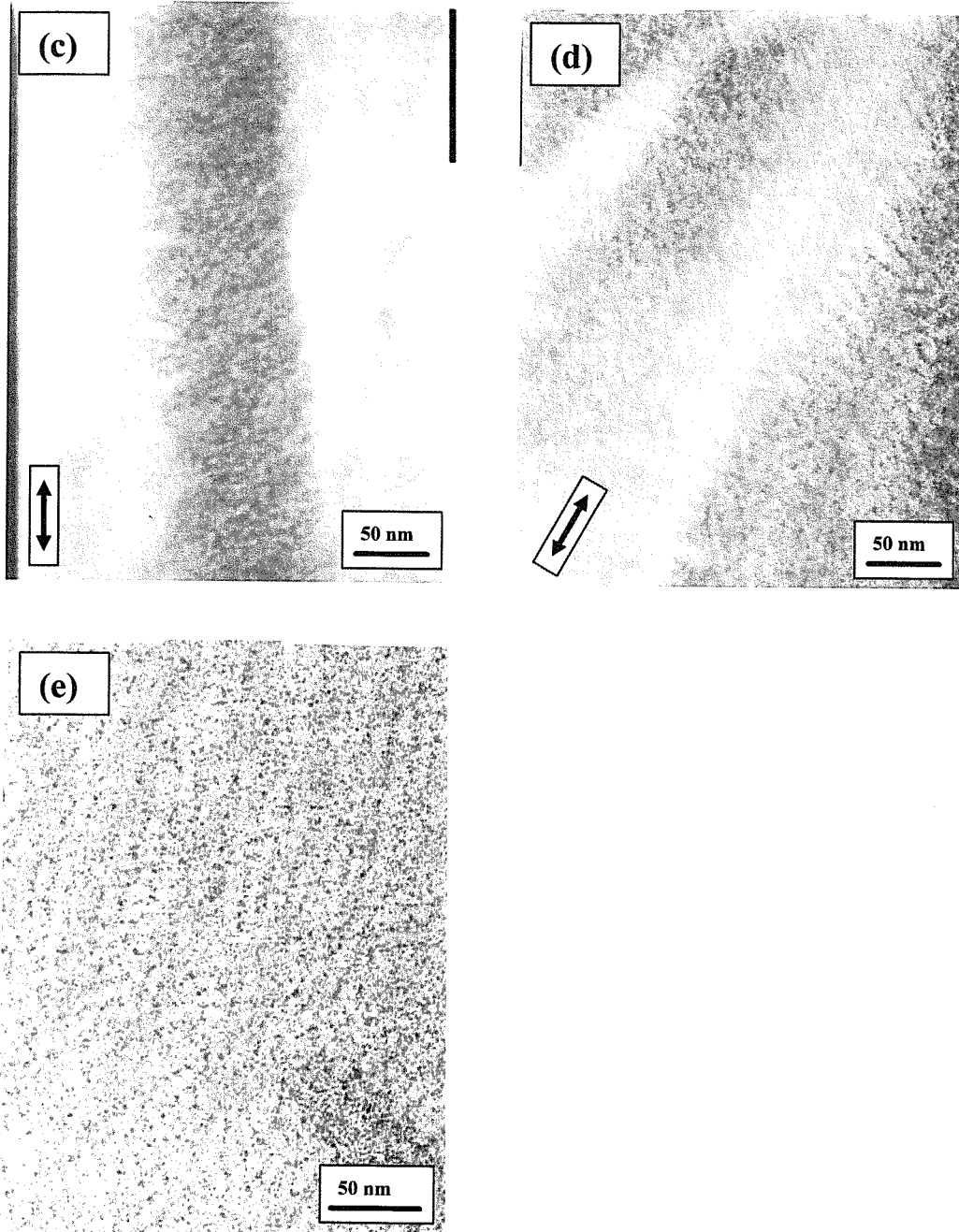
Figure 3(Continued): at high magnification; (c) from the edge view, (d) from the end and (e) from through view, respectively. The arrow indicates FD in (c) and TD in (d).
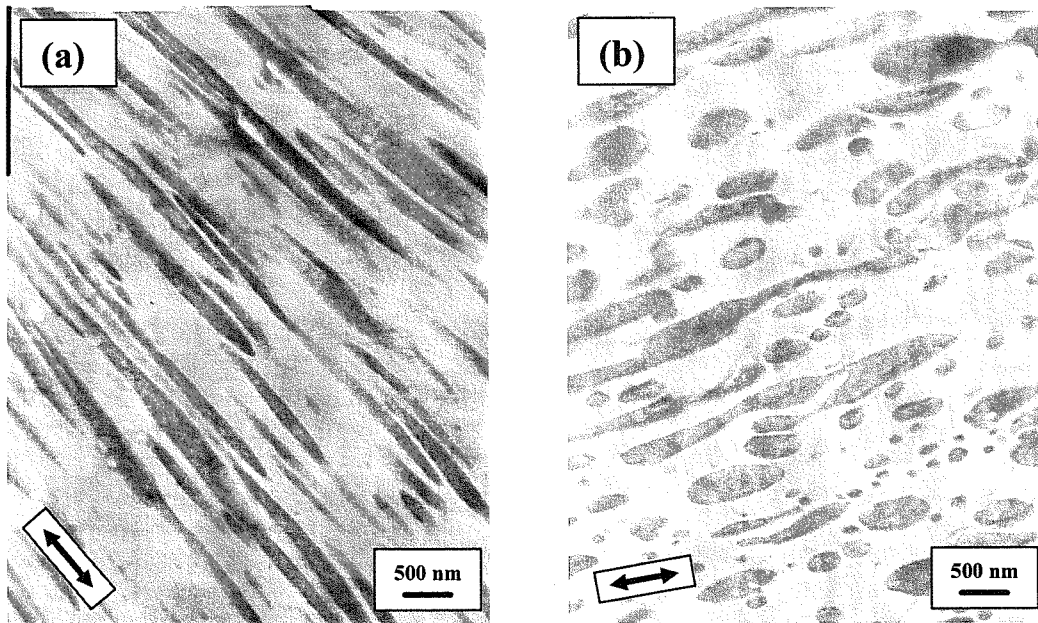
Figure 4: TEM micrographs of the PP-3/EOR blend at low magnification; (a) from the edge view and (b) from the end view, respectively. The arrow indicates FD in (a) and TD in (b).
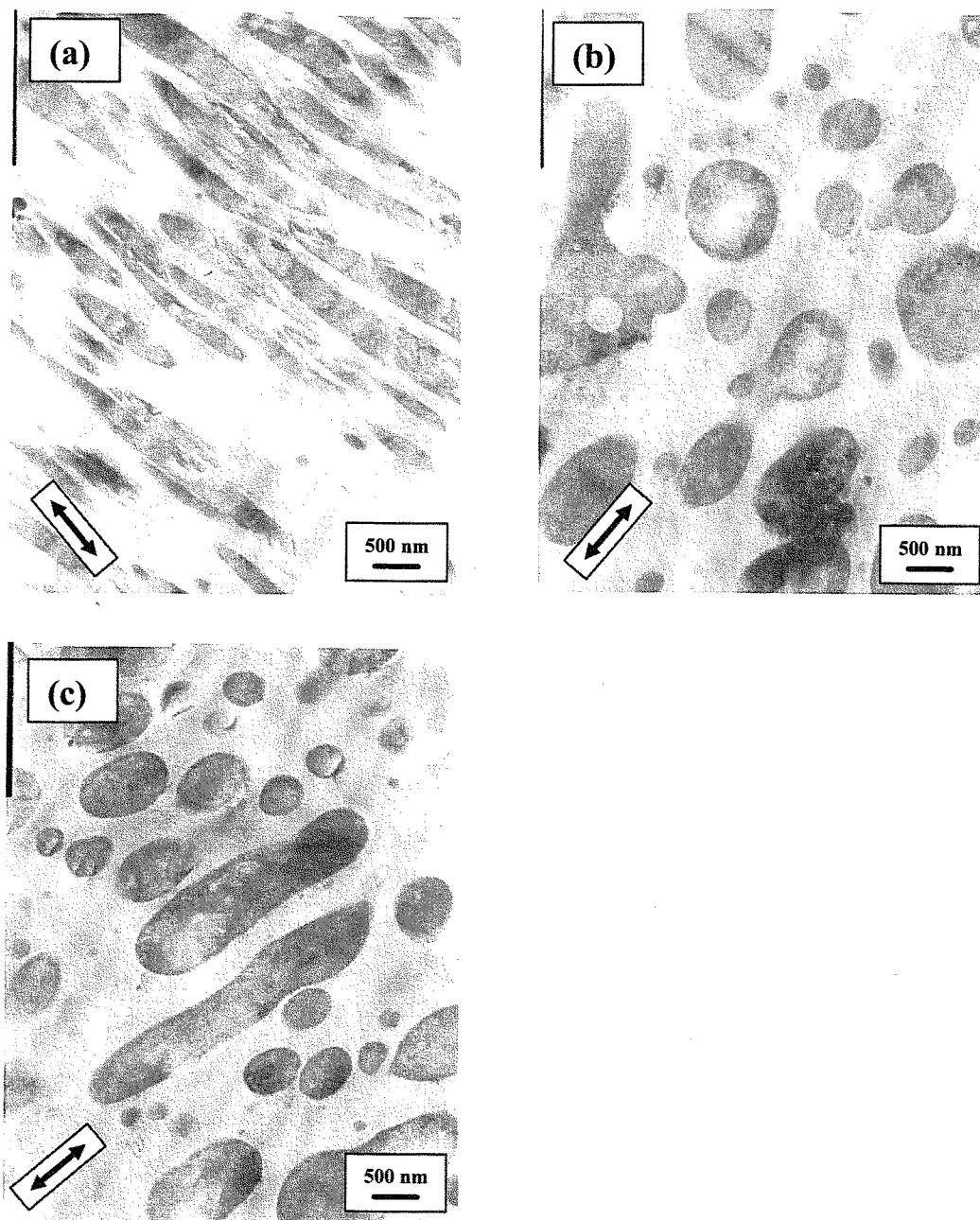
Figure 5: TEM micrographs of the PP-4/EOR blend; (a) from the edge view, (b) from the end view and (c) from the end view at different position, respectively. The arrow indicates FD in (a) and TD in (b) / (c).
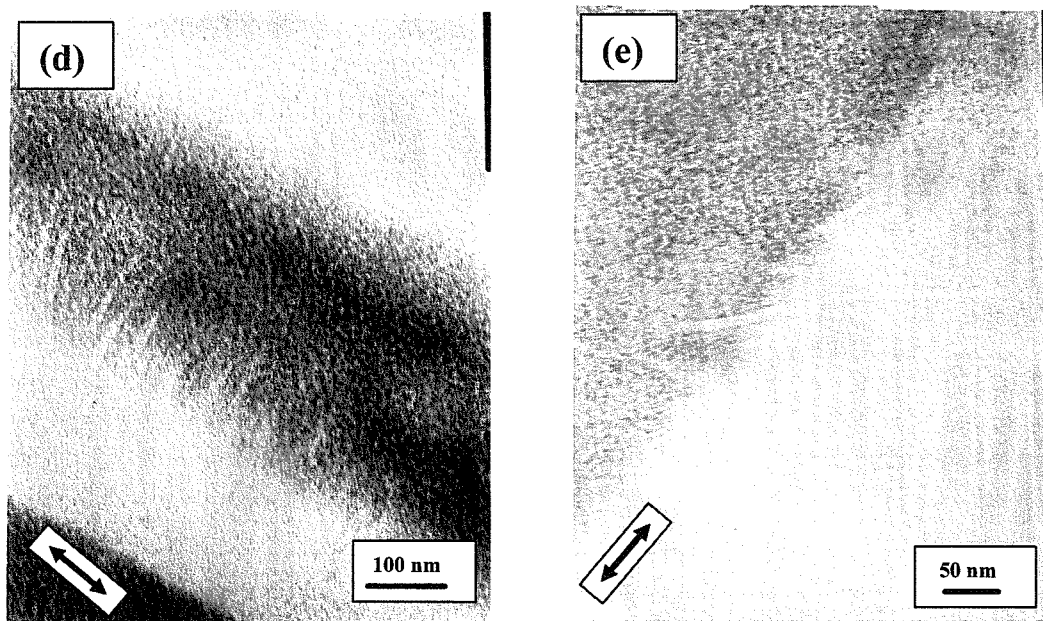
Figure 5(Continued): at high magnification; (d) from the edge view and (e) from the end and (e), respectively. The arrow indicates FD in (d) and TD in (e).
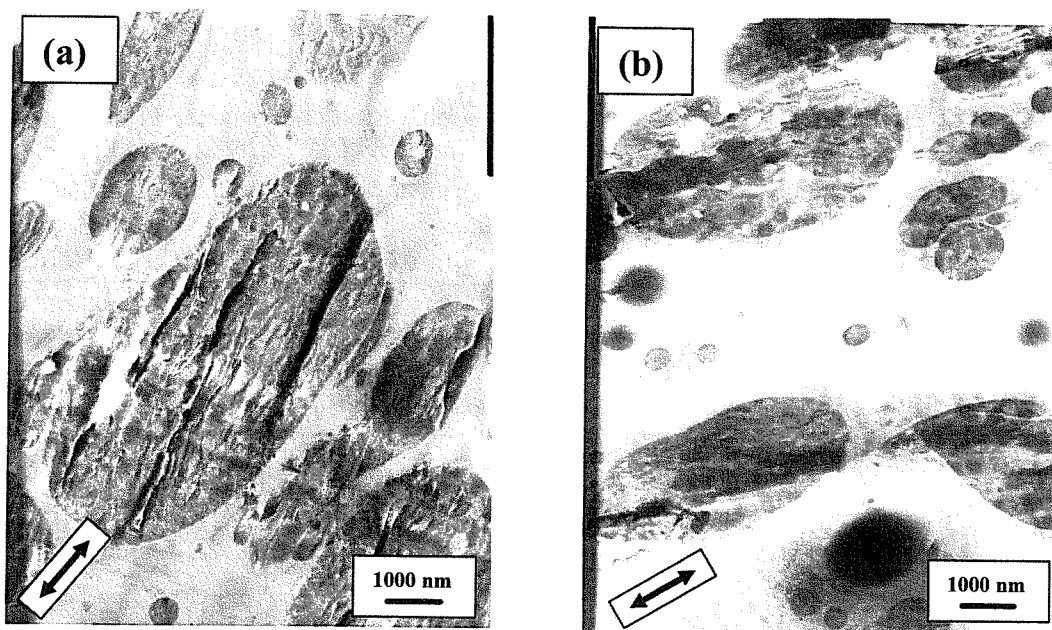
Figure 6: TEM micrographs of the PP-5/EOR blend; (a) from the edge view and (b) from the end view, respectively. The arrow indicates FD in (a) and TD in (b).
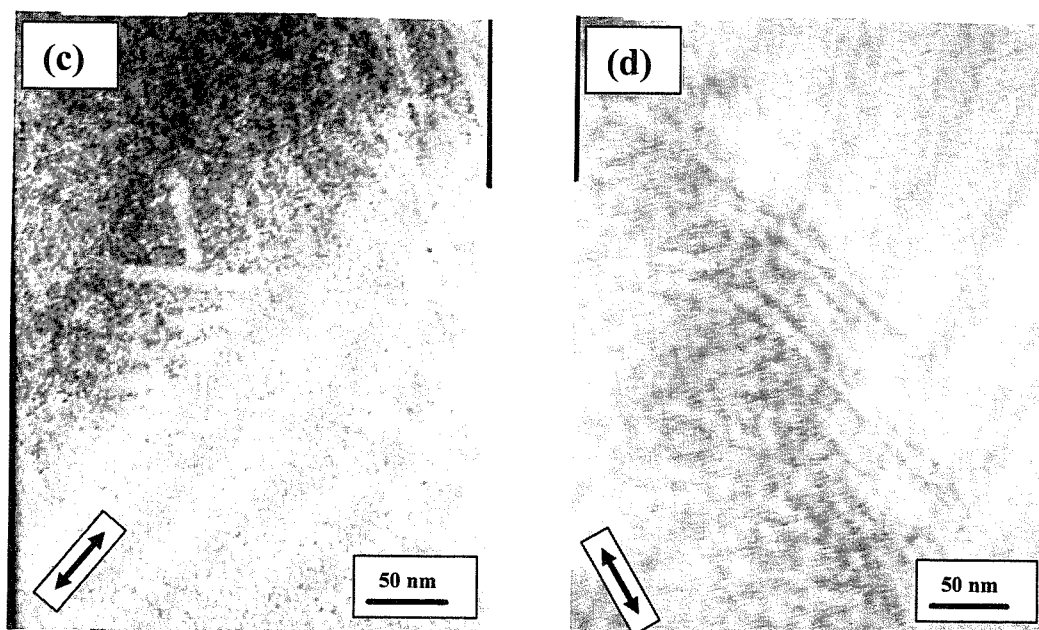
Figure 6(Continued): at high magnification; (c) from the edge view and (d) from the end and (e), respectively. The arrow indicates FD in (c) and TD in (d).

3-3. PP crystal orientation:

From the morphological observation by TEM, the difference of the arrays of the EOR domains would give rise to the orientation of the iPP lamellae, i.e., anisotropy of the iPP crystal orientation. It would also closely correlate with the CLTE anisotropy. In this section, the author investigates the correlation of the iPP crystal orientation in terms of three different types of the EOR arrays, the lamella-like sheet (iPP-2/EOR), the cylinder (iPP-4/EOR) and the sphere (iPP-5/EOR).

The orientation function f_a, f_b and f_c obtained from the WAXD for each direction are summarized in Table III. In the case of iPP-2/EOR, the f_c is the largest in both FD and TD, and the f_b the largest in ND, indicating that c-axis is principally oriented to FD and TD, whereas b-axis to ND. In the case of PP-4/EOR, similar orientation is found. It should however be noted that the f_c in FD for PP-2/EOR is nearly two-fold higher and the f_b in ND for PP-2/EOR is more than three times larger in comparison with those in the PP-4/EOR system. These observations indicate that the c-axis and the b-axis orientation to FD and ND in PP-2/EOR are much stronger than those in the PP-4/EOR system. In the PP-5/EOR system, the orientation of PP crystal seems to be relatively weaker in comparison with other two.

It should be pointed out from the X-ray and TEM studies that the PP crystal orientation depends strongly on the morphology (shape) of the elastomer domains in these systems.

64

Table III Orientaion function of PP crystalline part in the blend

Sample designation	Orientation function	Direction		
		FD	TD	ND
PP-2/EOR	f_a	0.0090	-0.029	0.012
	f_b	-0.24	-0.082	0.26
	f_c	0.23	0.11	-0.28
PP-4/EOR	f_a	0.010	-0.064	0.0050
	f_b	-0.13	-0.021	0.081
	f_c	0.12	0.085	-0.086
PP-5/EOR	f_a	-0.023	0.028	-0.077
	f_b	0.096	-0.084	-0.022
	f_c	-0.073	0.056	0.099

3-4. CLTE of lattice constants:

The CLTE for the lattice constant (α^{cr}_a, α^{cr}_b, and α^{cr}_c) was summarized in Table IV. It is found, from Table IV, that $\alpha l^{cr}_c < \alpha l^{cr}_a << \alpha l^{cr}_b$ and αl^{cr}_c are negative. Gu *et al.* reported that the thermal expansion of iPP crystal along the b-axis was 2.6 folds greater than that along the a-axis: that along the c-axis was ~10% of the a-axis [7]. The present results are thus in consistent with Gu *et al.*. It should be pointed out that each lattice constant for iPP-2 and the three blends is found to be equal, indicating that the presence of elastomers and their arrays have no influence of the CLTE of iPP crystal.

We estimate the anisotropy of the CLTE in the iPP phase by taking account the anisotropy in the CLTE and orientation of PP crystals. Based on the assumption that PP

amorphous phase is involved in the PP matrix (no compatibility with EOR), isotropic and connected in series with the iPP crystal phase, the CLTE of PP was given by equation (5) [8]

$$\alpha^{PP-X}{}_J = (1-c)\alpha^{am} + c\alpha^{cr}{}_J \qquad (5)$$

where c, α^{am} and α^{cr} denote crystallinity, CLTE of iPP amorphous part and CLTE of iPP crystal part, respectively. The superscript iPP-X denotes PP-2, PP-4 and PP-5, and the subscript J represents FD, TD and ND. The $\alpha^{cr}{}_J$ in equation (5) is given by $f^J{}_a\alpha_a + f^J{}_{b}\alpha_b + f^J{}_{c}\alpha_c$. Finally we obtain equation (6) for the CLTE of iPP for each direction J (=FD, TD and ND).

$$\alpha^{PP-X}{}_J = (1-c)\alpha^{am} + c(f^J{}_a\alpha^{cr}{}_a + f^J{}_b\alpha^{cr}{}_b + f^J{}_c\alpha^{cr}{}_c) \qquad (6)$$

Here, the α^{am} is assumed to be isotropic and, hence, being one third of the coefficient volume thermal expansion ($\alpha^{am} = 23$ (10^{-5} /°C)) [9]. Note that anisotropy in the amorphous phase would not be critical because the c-axis shows orientation along FD rather than ND (our focus). Indeed, Choy et al. [10] treated the amorphous phase to be isotropic.

Table IV CLTE for lattice constants from 23 to 100°C

Sample designation	Viscosity Ratio	CLTE ($10^{-5}/°C$)		
		α^{cr}_a	α^{cr}_b	α^{cr}_c
PP-2	-	5.20	17.7	-0.41
PP-2/EOR	0.081	9.90	19.0	-1.20
PP-4/EOR	3.0	6.80	16.0	-0.85
PP-5/EOR	13	8.90	17.6	-0.40

3-5. CLTE modeling:

There were a number of theoretical studies on the CLTE for filler reinforced plastics [11-18]. These investigations revealed that the CLTE anisotropy greatly depended upon the shapes, arrays or directions of filler inclusions. In the present case, the elastomer domains correspond to the filler inclusions. In addition, the effect of morphology and anisotropy in PP crystal (in CLTE) could be incorporated to the model.

Prior to the CLTE modeling, the following assumptions are made; (1) Consisting of two components, PP and EOR (no compatibility between PP and EOR), (2) Perfect adhesion between PP and EOR, and (3) No retraction from the EOR domains.

Taking account into the anisotropy effect of PP, we derived the formulae of CLTE for PP-2/EOR (lamella-like sheet), PP-4/EOR (cylindrical) and PP-5/EOR (spherical). As discussed in APPENDIX A, the anisotropic effect of elastic constants would be negligible, so that we assume the elastic constant to be isotropic.

(1) PP-2/EOR with lamella-like sheet EOR array

In this case, the elastomers align parallel to both in FD and TD and in series in ND. The thermal stress, σ (=αlΔTE) developed in FD and TD is thus the summation of a thermal stress for each component. As for ND, a thermal strain, ε (=αlΔT) in ND is the summation of a thermal strain for each component [18]. The final formula of CLTE for each direction is given by equation (7)-(9).

$$\alpha^{PP-2}{}_{FD}(calc) = \frac{\alpha^{PP-2}{}_{FD}\phi^{PP-2} + \alpha^{EOR}\zeta\phi^{EOR}}{\phi^{PP-2} + \zeta\phi^{EOR}} \tag{7}$$

$$\alpha^{PP-2}{}_{TD}(calc) = \frac{\alpha^{PP-2}{}_{TD}\phi^{PP-2} + \alpha^{EOR}\zeta\phi^{EOR}}{\phi^{PP-2} + \zeta\phi^{EOR}} \tag{8}$$

$$\alpha^{PP-2}{}_{ND}(calc) = \alpha^{PP-1}{}_{ND}\phi^{PP-2} + \alpha^{EOR}\phi^{EOR} \tag{9}$$

where $\zeta = E^{EOR}/E^{PP-2}$.

(2) PP-4/EOR with cylindrical EOR array

The CLTE model for fiber-reinforced plastics is applicable to this system. The model by Shapery [15] would be the most suitable for the present case. This model assumed that the complementary energy accompanying by a thermal stress was equal to the Gibbs's free energy of the entire body. The calculated CLTE are then given by equations (10), (11) and (12).

$$\alpha^{PP-4}{}_{FD}(calc) = \frac{\alpha^{PP-4}{}_{FD}\phi^{PP-4} + \alpha^{EOR}\zeta\phi^{EOR}}{\phi^{PP-4} + \zeta\phi^{EOR}} \tag{10}$$

$$\alpha^{PP-2}{}_{TD}(calc) = (1 + v^{PP-4})\alpha^{PP-4}{}_{TD}\phi^{PP-4} + (1 + v^{EOR})\alpha^{EOR}\phi^{EOR}$$
$$- (v^{PP-4}\phi^{PP-4} + v^{EOR}\phi^{EOR})\alpha^{PP-4}{}_{FD} \tag{11}$$

$$\alpha^{PP-4}{}_{ND}(calc) = (1 + v^{PP-4})\alpha^{PP-4}{}_{ND}\phi^{PP-4} + (1 + v^{EOR})\alpha^{EOR}\phi^{EOR}$$
$$- (v^{PP-4}\phi^{PP-4} + v^{EOR}\phi^{EOR})\alpha^{PP-4}{}_{FD} \tag{12}$$

where $\zeta = E^{EOR}/E^{PP-4}$.

68

(3) PP-5/EOR with spherical EOR array

In this case, the arrangement of elastomers is considered to be isotropic in all directions. Consequently, the model by Wang and Kwei [16] would be applied to this case. This model assumed that induced thermal stress at the interface between filler and plastics was limited only to the neighborhood of the interface; CLTE was then given by

$$\alpha^{PP-5}{}_{J}(calc) = \alpha^{PP-5}{}_{J}\left[1 - \phi^{EOR}(1 - \frac{\alpha^{EOR}}{\alpha^{PP-5}})\theta\right] \qquad (13)$$

where

$$\theta = \frac{3\xi(1 - v^{PP-5})}{\xi[2\phi^{EOR}(1 - 2v^{PP-5}) + (1 + v^{PP-5})] + 2(1 - 2v^{EOR})(1 - \phi^{EOR})} \qquad (14)$$

with $\zeta = E^{EOR}/E^{PP-5}$.

In these eqs. (7)-(14), E, v and v denote Young's modulus, Poisson's ratio and volume fraction (of each component), respectively.

3-6. Comparison with experiment:

In the present case, $\phi^{PP-2} = \phi^{PP-4} = \phi^{PP-5} = 0.70$ and $\phi^{EOR} = 0.30$. The Young's modulus of each component, E^{PP-2}, E^{PP-4}, E^{PP-5} and E^{EOR}, is summarized in Table I.

The Poisson's ratio v for PP-2, -4, -5 and EOR are assumed to be $v^{PP-2} = v^{PP-4} = v^{PP-5} = 0.4$ and $v^{EOR} = 0.50$. The α^{EOR} is 19 (10^{-5} /°C) as one third of the measured CVTE determined with pressure-volume-temperature (PVT) analysis [9]. Moreover, the anisotropy in the CLTE of EOR in the blend would be negligibly small because the each CLTE for FD, TD and ND in injection-molded specimen with pure EOR showed almost identical value [12]. Substituting the necessary values summarized in Table I ~ IV into eqs. (6)-(14), we estimate the CLTE of the blends. The results are summarized in Table V and compared with the observed results.

It is found from Table V that the calculated CLTEs for the PP-4/EOR and PP-5/EOR blends are in good agreement with the observed ones. The discrepancy between the calculated and observed CLTEs in ND may be negligible considering the large experimental errors in this direction. As a result, the CLTE anisotropy in the PP-4/EOR with cylindrical rubber array and the PP-5/EOR with spherical array are accounted for by the effect of the array of the elastomer inclusions and the iPP crystal orientation.

In the case of PP-2/EOR blend, we pointed out in Chap. 2 that a simple composite model (lamella-like sheet array), which incorporated no anisotropy in iPP phase, was not able to account for the massive discrepancy between the observed and calculated CLTEs in FD and ND; in PP-2/EOR, $\alpha_{ND}/\alpha_{FD}{\sim}1.2$ (calc.) and $\alpha_{ND}/\alpha_{FD}{\sim}7.6$ (obs.). In the present model incorporating the iPP crystal orientation as well as the array of the elastomer domains, discrepancy is a bit improved for the CLTE in FD, $\alpha_{ND}/\alpha_{FD}{\sim}1.9$ (calc.) and $\alpha_{ND}/\alpha_{FD}{\sim}7.6$ (obs.).

However, there still has a large discrepancy between the observed and calculated CLTEs in both FD and ND, $\alpha_{FD}{}^{calc}/\alpha_{FD}{}^{obs}{\sim}1.7$ and $\alpha_{ND}{}^{calc}/\alpha_{ND}{}^{obs}{\sim}0.41$. It indicates that some other factors would be operative for the CLTE anisotropy with this case.

Table V Calculated CLTE with the effect of arrays of elastomers and PP crystalline orientation taken into consideration

Sample designation	α_{FD}		α_{TD}		α_{ND}	
	Calc	Obs	Calc	Obs	Calc	Obs
PP-2/EOR	10	6.0	11	7.8	19	46
PP-4/EOR	10	10	15	13	16	25
PP-5/EOR	17	14	16	16	16	23

3-7. Retraction effect:

For the PP-2/EOR (lamella-like sheet), the massive CLTE discrepancy in FD or ND between its observed and calculated value would result from the fact that one of the assumptions for the present model might be inappropriate. In this section, the effect of retraction in elastomer domains, which was not considered for the CLTE calculation, is discussed.

As derived in APPENDIX B, the deformation by retraction force along each ND and FD is estimated by equations (15) and (16).

$$\frac{\Delta L_{ND}}{L_{ND}} \approx \frac{n^*}{L_{ND}} \cdot \frac{8\gamma}{E} \cdot \frac{t}{x} \qquad (15)$$

$$\frac{\Delta L_{FD}}{L_{FD}} \approx -\frac{1}{L_{FD}} \cdot \frac{4\gamma}{E} \qquad (16)$$

where n^*/L_{ND} and γ denoted the number of slab per unit length and interfacial tension between iPP and EOR. t and x are given in Figure 7.

From the TEM observation in Figure 2(a), n^*/L_{ND} and t/x are estimated to be $\sim 6 \times 10^6$ and $\sim 10^{-2}$, respectively. In addition, we obtain $E^{EOR} \sim 5 \times 10^4$ Pa and $\gamma \sim 1.2 \times 10^{-3}$ J/m^2 (measured). Inserting these numbers into equation (16) and (15), we obtain

$\Delta L_{ND}/L_{ND} \sim 12 \times 10^{-3}$ and $\Delta L_{FD}/L_{FD} \sim 6.4 \times 10^{-6}$. This contribution to the α_{ND} and α_{FD} was thus given by $\Delta L_{ND}/(\Delta TL_{ND})$ and $\Delta L_{FD}/(\Delta TL_{FD})$. Inserting $\Delta T = 77^{\circ}C$, we obtain $\Delta L_{ND}/(\Delta TL_{ND})$ and $\Delta L_{FD}/(\Delta TL_{FD})$ to be ~ 15 (10^{-5} $/^{\circ}C$) and -0.0083 (10^{-5} $/^{\circ}C$), respectively, the latter value being low enough to ignored. It indicates that the retraction of the interfacial tension has little or no contribution to the CLTE in FD.

On the other hand, as for the contribution of the retraction to the CLTE in ND, combining the contribution from retraction with that from the anisotropy by the PP crystal orientation yields $\alpha_{ND} \sim 34$ (10^{-5} $/^{\circ}C$) and hence, $\alpha_{ND}^{calc}/\alpha_{ND}^{obs} \sim 0.74$, being a bit closer to the observation. Hence, the deformation arising from the retraction in ND would be effective to α_{ND} [20]. The discrepancy between the calculated CLTE (~ 10 (10^{-5} $/^{\circ}C$)) and the observed one (~ 6.0 (10^{-5} $/^{\circ}C$)) in terms of the FD remains questionable, which will be discussed in the next Chapter.

For more precise estimation, however, detailed knowledge on the morphology, elastic constant at an elevated temperature as well as the more refined formulation of the equation (16) would be necessary.
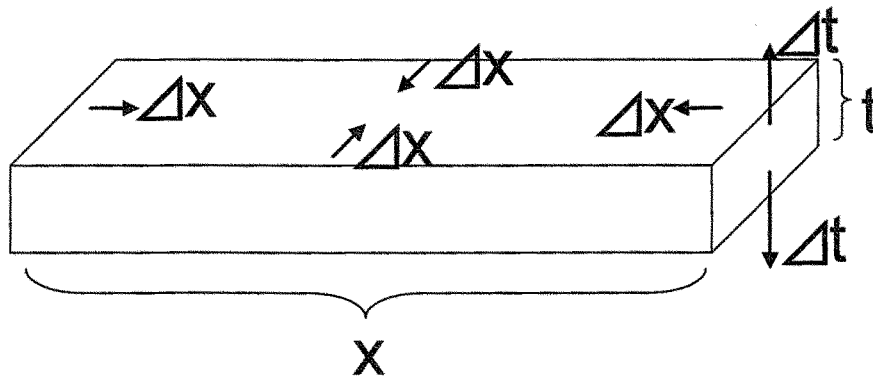
Figure 7: Deformation mode by retraction. .

4. Conclusions

The coefficient of linear thermal expansion, (CLTE), of a polymer blend consisting of polypropylene (PP) and poly(ethylene-*co*-octene) (EOR) with a different viscosity ratio, $\eta_0^*(EOR)/\eta_0^*(iPP)$, was investigated by TMA. As decreasing $\eta_0^*(EOR)/\eta_0^*(iPP)$, the CLTE depended strongly on the directions, namely, FD, TD and ND. TEM observations revealed that the arrays of the EOR domains varied with the viscosity ratio, $\eta_0^*(EOR)/\eta_0^*(iPP)$; "slab" at 0.036, "lamella-like sheet" at 0.082, "mixture of lamella and cylinder" at 0.92, "cylinder" at 3.0 and "ellipsoid or spherical" at 13. The WAXD analysis on the orientation function revealed that iPP crystal growth was strongly dependent upon this array of the elastomer domains; the c-axis were grown parallel to FD, and the b-axis parallel to ND for the lamella-like sheet array.

Taking account the EOR morphology and iPP crystal orientation, we estimated the CLTE in FD, TD and ND based on the composite model depending on the elastomer array. It was found that the incorporation of the anisotropy in iPP resulted in a better prediction in the CLTE with the cylindrical and the spherical arrays. However, as for the lamella-sheet array, substantial difference in the CLTEs of both FD and ND between the model and observation still remained. The effect of retraction deformation was then estimated. It was found that the retraction effect from the interfacial tension of the deformed elastomer would be important to explain the larger number of α_{ND}.

5. References

[1] Nomura T., Nishio T., Taniguchi H., Hirai I. and Hisamura N.; *Kobunshi Ronbunshu*, 1994, **51**, 505

[2] Wu G., Nishida K., Takagi K. Sano H. and Yui H.; *Polymer*, 2004, **45**, 3085

[3] Alexander L.E.; *"X-ray Diffraction Methods in Polymer Science"*, Wiley-Interscience, New York, 1969

[4] Wilchinsky Z.W.; *J. Appl. Polym. Sci.*, 1963, **7**, 923

[5] Mondoza R., Regnier G., Seiler W., Lebrun J.L.; *Polymer*, 2003, **44**, 3363

[6] Nomura T.; *Ph. D. Thesis* Nagoya University 1994

[7] Gu F., Hikosaka M., Toda A., Gosh S.K., Yamazaki S., Arakaki A., Yamada K.; *Polymer*, 2002, **43**, 1473

[8] Porter R.S., Weeks N.E., Capiati N.J., Krzewki R.J.; *J. Thermal. Anal.*, 1975, **8**, 547

[9] Zollar P. and Walsh D.J.; *"Standard Pressure-Volume-Temperature Data for Polymers"*, Technomic Publishing Co., Inc. 1995

[10] Choy C.L., Chen F.C. and Ong E.L.; *Polymer*, 1979, **20**, 1191

[11] Raghara R.S.; *Polym. Comp.*, 1988, **9**, 1

[12] Kerner E.H.; *Proc. Phys. Soc.*, 1956, **B69**, 808

[13] Holliday L. and Robinson J.; *J. Mate.r Sci.*, 1973, **8**, 301

[14] Turner P.S.; *J. Res. Nat. Bur. Stand.*, 1946, **37**, 239

[15] Shapery R.A.; *J. Composite Mater.*, 1968, **2**, 380

[16] Wang T.T. and Kwei T.K.; *J. Polym. Sci., Part A-2*, 1969, **7**, 889

[17] Cribb J.L.; *Nature*, 1968, **220**, 576

[18] Burkley C.P. and McCrum N.G..; *J. Mater. Sci.*, 1973, **8**, 1123

[19] Tashiro K., Kobayashi M. and Tadokoro H.; *Polym. Preprints Japan*, 1986, **35**, 3266.

[20] The numerical factor, which would depend on the shape of the domain, is on the order of 1, indicating that the contribution from the retraction would be on the order of ~10 (10^{-5} /°C). Hence, the contribution from the retraction will still be important.

[21] Gramespacher H. and Messner J.; *J. Rheol.*, 1997, **1**, 27.

6. Acknowledgement

APPENDIX A

From equations (7), (8) and (11), the variation of CLTE can be obtained through the Taylor expansion in terms of $\Delta\xi$ to the first order, and given by equation (A-1), where X=1 and 2, and J=FD and TD.

$$\Delta \ln(\alpha l^{PP-X/EOR}) = \frac{\Delta \alpha l^{PP-X/EOR}_J}{\alpha l^{PP-X/EOR}_J} = \frac{\phi^{EOR}(\alpha l^{EOR} - \alpha l^{PP-X}_J)}{\alpha l^{PP-X}_J \phi^{PP-X}} \Delta \xi \qquad (A-1)$$

Note that in this calculation, we use $\xi \sim 10^{-2}$ from experimental (small).

Substituting $\phi^{EOR}=0.3$, $\phi^{PP-X}=0.7$, $(\alpha^{EOR} - \alpha^{PP-X})/\alpha^{PP-X} \sim 1.3$ and $\Delta\xi$ ($\equiv \Delta[E^{EOR}/E^{PP-X}]$) < $20\times10^6 \times (1/2\times10^9 - 1/40\times10^9) < 10^{-2}$ [20] at room temperature, we obtain (A-2).

$$\frac{\Delta \alpha l^{PP-X/EOR}_J}{\alpha l^{PP-X/EOR}_J} < 5\times10^{-3} \qquad (A-2)$$

At an elevated temperature, $\Delta[E^{EOR}/E^{PP-X}] < 10^6 \times (1/200\times10^6 - 1/40\times10^9) < 10^{-2}$. indicating that ξ would be also negligible.

The effect of anisotropy in elastic constant would thus be negligible. Note that in the case of PP-3/EOR system, the PP orientation was found to be almost isotropic. E^{PP-3} can thus be isotropic one.

APPENDIX B

According to Gramespacher et al. [21], the driving force of the retraction is attributed to the interfacial energy reduction. The free energy variation, ΔG, based on the surface area change, ΔA, is thus given by equation (B-1), where γ denotes interfacial tension between iPP and EOR.

$$\Delta G = \gamma \Delta A \qquad (B-1)$$

Referring Fig. 7, ΔA is given by equation (B-2), where $t/x \ll 1$ is used.

$$\Delta A = 4(x-t)\Delta x \approx 4x\Delta x \qquad (B-2)$$

From the volumetric consideration, we obtain equation (B-3).

$$\frac{\Delta t}{\Delta x} = -2\frac{t}{x} \qquad (B-3)$$

The equation (B-3) corresponds to the Poisson's ratio, $\nu \equiv -\dfrac{\Delta x/x}{\Delta t/t}$, to be 0.5 (no volume change). The retraction force, f_{ret}, and the displacement, Δx, are then given by equations (B-4) and (B-5).

$$f_{ret} = -\frac{\Delta G}{\Delta x} \approx -4x\gamma \qquad (B-4)$$

$$\Delta x \approx -\frac{4\gamma}{E} \qquad (B-5)$$

Inserting (B-3) into (B-5), we obtain equation (B-6)

$$\Delta t \approx \frac{8\gamma}{E} \cdot \frac{t}{x} \qquad (B-6)$$

Assuming that there are n* plates in the unit thickness in ND, we obtain the total deformation along ND, ΔL_{ND}, to be given by equation (B-7).

$$\Delta L_{ND} = \Delta t n^* \approx \frac{8\gamma}{E} \cdot \frac{t}{x} n^* \qquad (B-7)$$

Hence, the contribution of the retraction to α_{ND}, $\dfrac{\Delta L_{ND}}{L_{ND}}$, is given by (B-8), corresponding to equation (16) in the text.

$$\frac{\Delta L_{ND}}{L_{ND}} \approx \frac{n^*}{L_{ND}} \cdot \frac{8\gamma}{E} \cdot \frac{t}{x} \qquad\qquad \text{(B-8)}$$

Chapter 5:

Difference in CLTE Anisotropy by Chemical Composition in TPE of Injection-molded iPP/TPE Blends

1. Introduction

In Chap. 4, the author reported that in the injection-molded iPP/EOR blends, the CLTE anisotropy was greatly dependent on the arrays of the EOR domains. The variation of the elastomers array was easily attained by controlling the viscosity ratio of EOR/iPP being less than unity. Among the various elastomers arrays, the lamella-sheet EOR array showed massive CLTE anisotropy, i.e., suppression of the thermal expansion both along the FD and TD being extremely low but preferable expansion of that along the ND leading to very high CLTE.

Such CLTE anisotropy for the lamella-sheet array was, to some extent, accounted for by the mechanical constraint and the retraction of the EOR sheet having high CLTE arranging in parallel with the iPP matrix with higher Young's modulus, by the iPP crystal orientation and by the retraction from the interfacial tension of the deformed EOR in a molten state (ND).

However, there remains question about massive discrepancy of the CLTE in the FD between the observed and the calculated CLTE employing the composite model introducing the retraction from the molten EOR as well as the effect of both the EOR array and the iPP crystal orientation cited above.

In this chapter, we investigated the CLTE anisotropy using the injection-molded blends composed of iPP and various thermoplastic elastomers (TPEs). In this study, the array of the TPE domain was fixed as the lamella-like sheet and, under this TPE array, we changed the chemical composition and the co-unit content in the TPE combined with the iPP thus the compatibility with the iPP. By this investigation, we could get an information about the correlation of the CLTE anisotropy with the compatibility of the TPE with the iPP matrix.

From this study, we found the importance of location of the iPP amorphous region in the blend on the CLTE along FD. In addition, we tired to estimate the CLTE in FD employing the simple composite model by Takayanagi et al. [1] under three components, TPE, iPP crystal phase and iPP amorphous phase not two components, iPP and TPE in the previous chapters.

2. Experimental

2-1. Raw materials and sample preparation:

IPP having 165 °C of melting temperature, 98.5 % of mmmm pentad sequences by ^{13}C-NMR and 2.8 dg/min of melt low rate (MFR) at 230 °C under 21.6 N of load was kindly donated from SunAllomer. The author chose four types of the ethylenic TPEs combining with the iPP, poly(ethylene-*co*-propylene) rubber (EPR) purchased from Dow Chemical, poly(ethylene-*co*-butene) rubber (EBR) from JSR, poly(ethylene-*co*-octene) rubber (EOR) from Dow Chemical and polyethylenes (PE) from Japan Polyethylene. Their general characteristics were presented in Table I. The MFR of the TPE was higher than that of the matrix iPP in order to adjust the morphology of the elastomer to be lamella-like sheet arrays (discussed later). The

abbreviation listed in the table was based on the co-unit type and its content; for instance, poly(ethylene-co-octene) rubber containing 9.0 wt% of 1-octene as a co-unit was abbreviated as EOR9.

The iPP/TPE binary blend with 70/30 (v/v) blend composition was prepared by melt-blended with a co-rotating twin screw extruder with 52 of L/D (TEX30α; JSW) under 180 °C of cylinder setting temperatures. The information of each blend is presented in Table II. In the Table II, Xc, the crystallinity of the iPP crystal in the blend, was obtained by dividing the endothermic enthalpy (ΔH) by the one corresponding to the perfect crystalline iPP, 209 (J/g). The ΔH and T_m were measured using a differential scanning calorimetry (DSC) at a scanning rate of 10 °C/min. The resulting blend was injection-molded to obtain a slab-shaped specimen, 125 (length) by 20 (width) by 3.0 (thickness) mm^3 using an injection machine (α100C; FUNAC) under 200 °C of cylinder setting temperatures, 40 °C of a tool temperature and 40 mm/s of an injection rate. The definition of the directions and the cross-sections were illustrated in Figure 1 in Chap. 2. The specimens obtained were annealed at 100 °C for 24 hours prior to use to remove their thermal history and residual stress.

Table I Characteristics of raw materials

Polymer type	Abbreviation	Co-unit content (nominal) wt%	MFR at 230°C dg/min.	Tm °C	Flexure modulus (nominal) MPa
Isotactic PP	iPP	-	2.4	166	1,650
Polyethylene (PE)	HD [a)]	-	8.1	135	1,300
	LD [b)]	-	10	113	140
Poly(ethylene-co-octene) rubber (EOR)	EOR9	9.0	6.3	103	110
	EOR24	24	8.9	60	12
	EOR30	30	2.5	33	3.5
Poly(ethylene-co-butene) rubber (EBR)	EBR5	5.0	16	120	160
	EBR17	17	5.9	85	20
	EBR20	20	6.0	68	14
	EBR32	32	6.8	35	10
Poly(ethylene-co-propylene) rubber (EPR)	EPR30	30	1.0	43	No data (<3.0)
	EPR57	57	0.86	No melting peak	No data (<3.0)

a) High density polyethylene, b) Low density polyethylene

Table II Characteristics of iPP-TPE blends

Abbreviation	TPE type	Tm °C	MFR ratio; TPE/iPP	Flexural modulus ratio; TPE/iPP	Xc %
iPP	iPP	166	-	-	48
iPP-HD	PE	164	2.9	0.78	42
iPP-LD		166	5.7	0.085	43
iPP-EOR9	EOR	166	2.3	0.062	43
iPP-EOR24		166	3.2	0.036	48
iPP-EOR30		167	1.0	0.020	50
iPP-EBR5	EBR	166	5.7	0.073	43
iPP-EBR17		166	2.1	0.052	46
iPP-EBR20		166	2.1	0.041	45
iPP-EBR32		165	2.4	0.021	47
iPP-EPR30	EPR	166	0.36	< 0.0020	44
iPP-EPR57		166	0.31	< 0.0020	47

2-2. CLTE evaluation:

The CLTE evaluation in this study was carried out according as the similar procedures described in Chap. 4 except for the measured temperature range (0 to 100 °C in this study).

The average CLTE (α^{obs}) on a given temperature range was given by equation (1).

$$\alpha^{obs} = \frac{1}{L}\frac{L_2 - L_1}{T_2 - T_1} \qquad (1)$$

where L, L_1 and L_2 are the reference length measured at 23 °C, the length at T_1 (0 °C in this work) and the length at T_2 (100 °C in this work), respectively.

2-3. Morphology observation:

The morphologies of the edge- and end-view were observed using a transmission electron microscopy (TEM) (JEM1200EX; JEOL) operated at 120 kV of an accelerating voltage. An ultra-thin section (thickness; 70-80 nm) microtomed at -100 °C was taken from the core layer of the slab after being stained with RuO_4 vapor at 40 °C for 5 hours.

2-4. iPP crystal axis orientation:

The crystalline orientation of the iPP in the blend was investigated using a wide angle X-ray diffractometer with a pole figure attachment (WAXD) according as the same procedures described in Chap. 4.

2-5. iPP amorphous orientation by optical microscopy:

The orientation function (f^{FD}_{am}) of the iPP amorphous region in the FD was determined from the birefringence (Δn)(measured), degree of crystallinity (X_c), and c-axis orientation function (f^{FD}_c) in the FD obtained by the X-ray pole figure using

$$f^{FD}_{am} = \frac{\Delta n - \Delta n^0_c X_c f^{FD}_c}{\Delta n^0_{am}(1 - X_c)} \qquad (2)$$

where Δn^0_c and Δn^0_{am} were the intrinsic crystal birefringence and the intrinsic amorphous birefringence, 0.0331 and 0.0468, respectively [2-3].

The Δn was obtained by a polarized optical microscope (POM) (BLX-40, Olympus Optical) with a Berek compensator. The sample was sliced to 50 μm thickness from the edge view with a razor blade at room temperature.

2-6. Dynamic mechanical thermal analysis (DMTA):

The measurements on the linear dynamic mechanical properties were made using a dynamic mechanical thermal analyzer (DMTA)(RSA-III; TA Instruments) on a tensile mode. The rectangular specimens with 30 (length) by 3.0 (width) by 0.4 (thickness) mm^3 were cut out from the slab and mounted in a specimen holder in such a way that the "length" direction, thus the oscillatory strain direction, coincided with the FD. Storage modulus (E'), loss modulus (E"), and loss tangent (tanδ) were monitored ranging from -80 to 140 °C at a constant frequency of 1.0 Hz and a heating rate of 4.0 °C/min.

3. Results

3-1. Morphology observation by TEM:

Figures 1-4 show the TEM micrographs in the edge-view parallel to FD from the iPP-PE, -EOR, -EBR and –EPR blend, respectively. In these figures, the dark regions represent the TPE-rich phases and the bright ones are the iPP-rich phases. In the iPP-PE (Fig. 1), -EOR (Fig. 2) and EBR (Fig. 3), the TPE-rich phases are highly deformed to the FD thus resulting in long thin fibrils, and form co-continuous structures with the iPP matrix. In the iPP-EPR blend (Fig. 4), coarse, short fibrils as well as the long fibrils are sporadically observed.

For Newtonian fluids, drop-to-fibril transition under shear was intensively investigated by many people [4-6]. They reported that the major factor for fibril formation was the viscosity ratio of droplet to matrix in the case that the viscosity ratio was close to or less than unity. This result would be also applicable for injection-molded iPP/TPE binary blend systems; in fact, long thin fibril formation was reported when the viscosity ratio τ of the dispersed TPE phase to the iPP matrix was equal to or less than unity under shear flow [7].

Hence, for the present PE, EO and EB blends, the major factor for the thin fibril formation will be ascribed to the viscosity ratio when considering their MFR ratios of the TPE phase to the iPP phase are more than unity, i.e., $\tau \leq 1.0$. In the case of the iPP-EPR blends whose MFR ratios are less than unity, i.e., $\tau \geq 1.0$, an incomplete droplet-to-fibril transition would occur, thus resulting in the coarse and/or short fibrils of the TPE domains.

TEM photographs of the iPP-PE, -EOR, EBR and EPR from the end view parallel to TD are shown in Figures 5-8, respectively. The long thin fibril formation is also

found in TD as well as FD although some short fibrils and/or droplets resulting from break-up of the fibrils are sporadically observed. The fibril break-up would be due to the principal normal stress difference imposed onto TD which is, in general, stronger than the shear stress for the driving force inducing the fibril formation along FD [8-9].

Based on the edge- and end view observation, the arrays of the rubber domains are assumed to be in the lamella-like sheet shape stacked normal to ND for the iPP-PE, -EOR and –EBR blends and in the ellipsoidal slab shape for the iPP-EPR blends which are schematically illustrated in Figure 9.
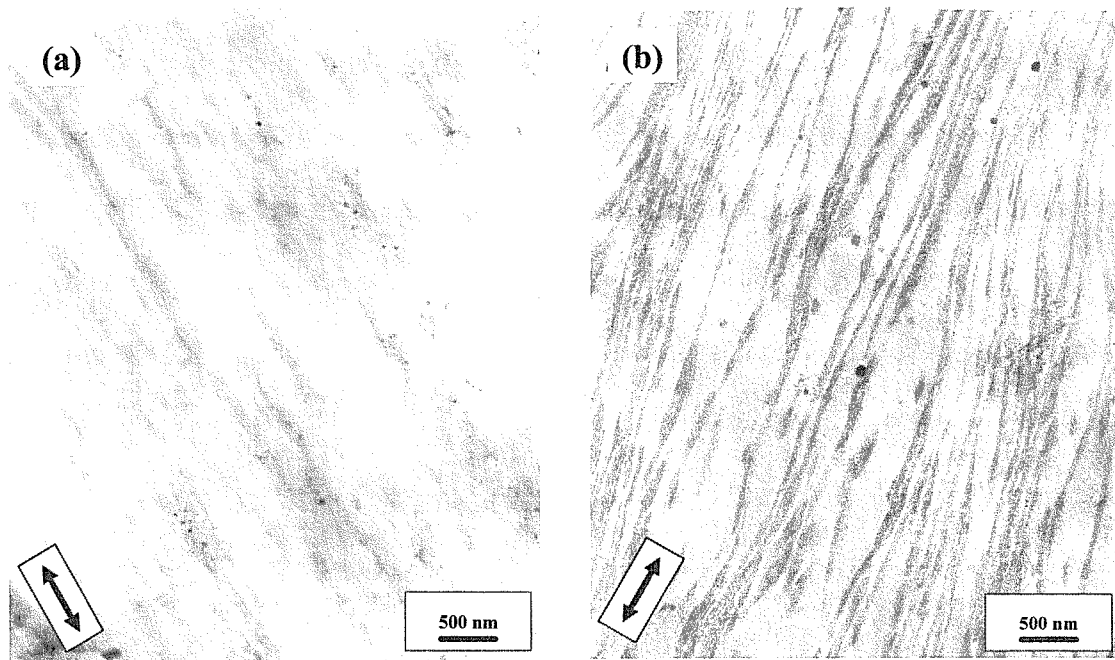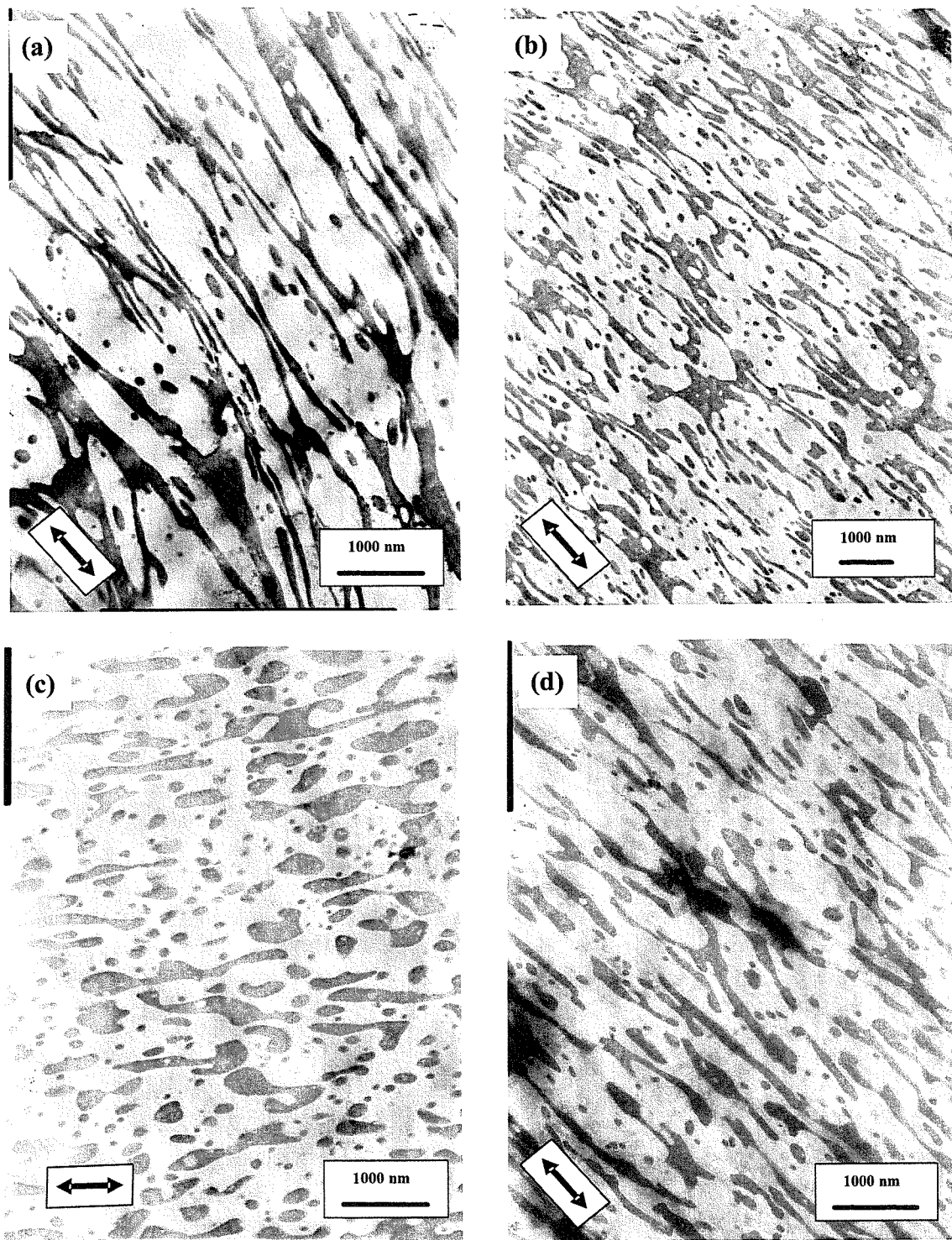
Figure 1: TEM micrographs of iPP/TPE blends in the edge view; (a) iPP/HDPE and (b) iPP/LDPE blend, respectively. The arrow indicates FD.
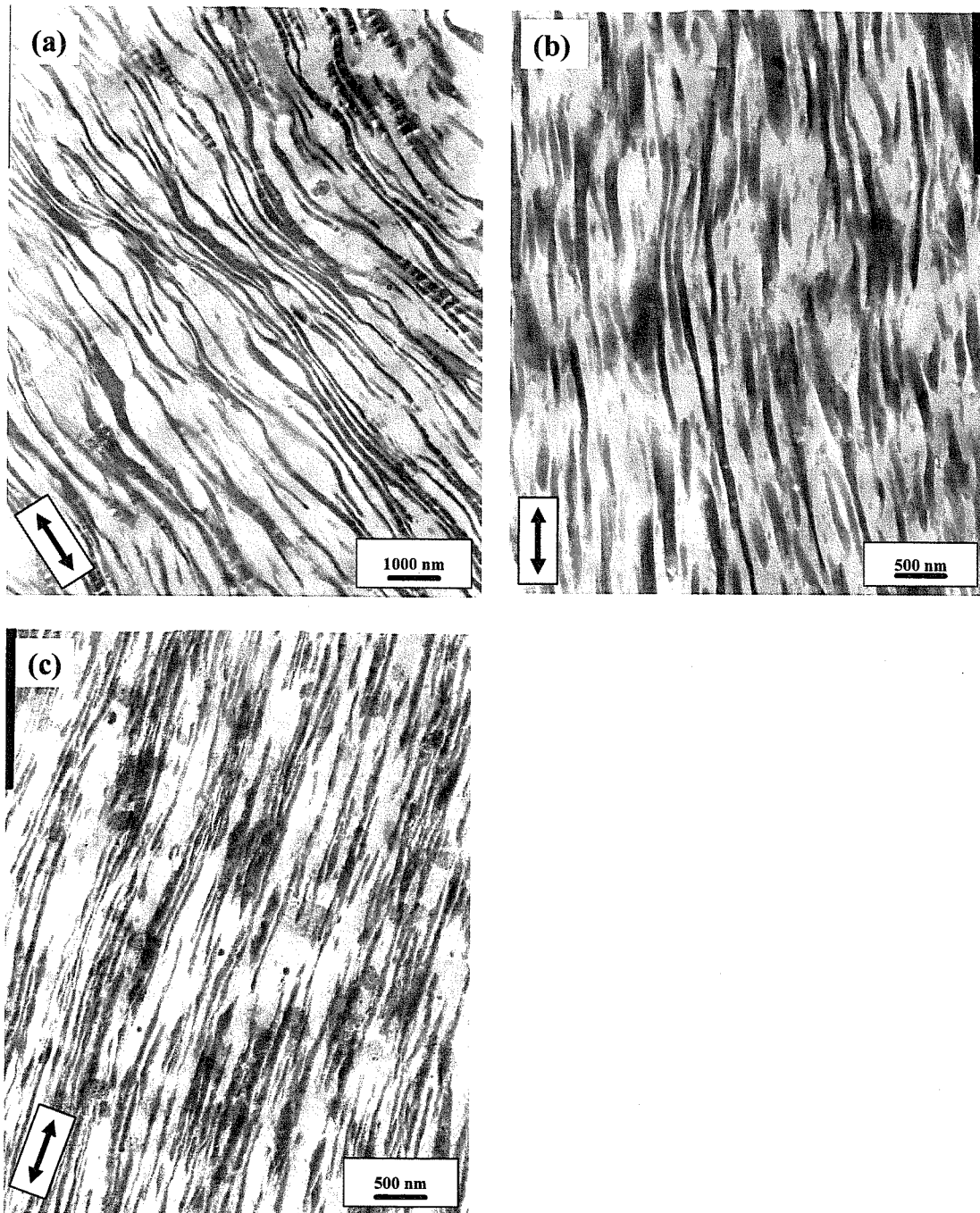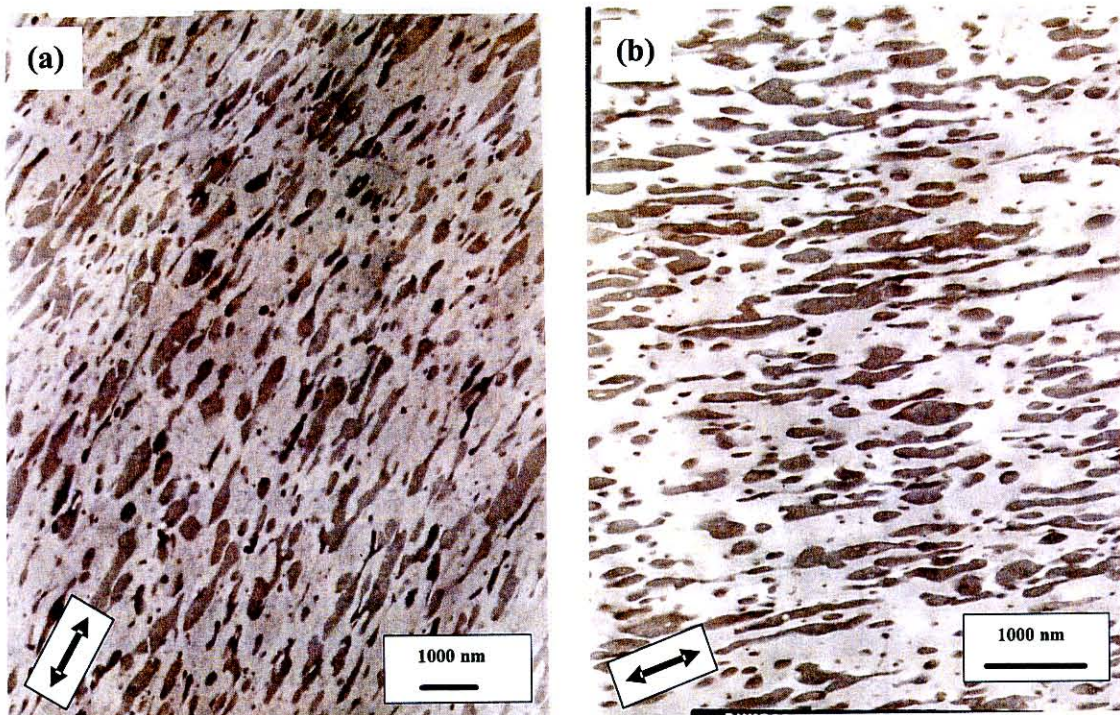
Figure 2: TEM micrographs of iPP/TPE blends in the edge view;
(a) iPP/EOR9, (b) iPP/EOR24 and (c) iPP/EOR30 blend,
respectively. The arrow indicates FD.
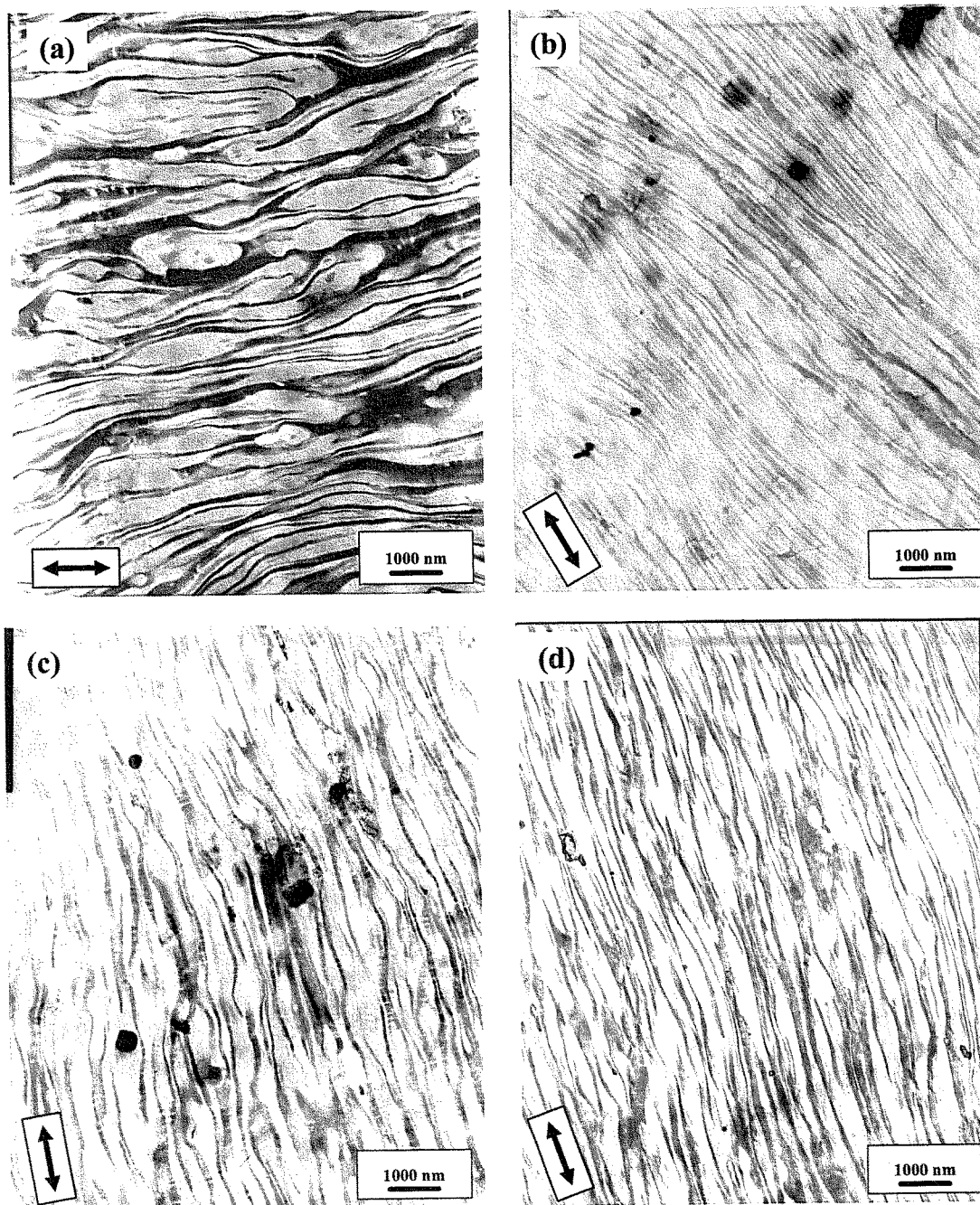
Figure 3: TEM micrographs of iPP/TPE blends in the edge view; (a) iPP/EBR5, (b) iPP/EBR17, (c) iPP/EBR20 and (d) iPP/EBR32 blend, respectively. The arrow indicates FD.
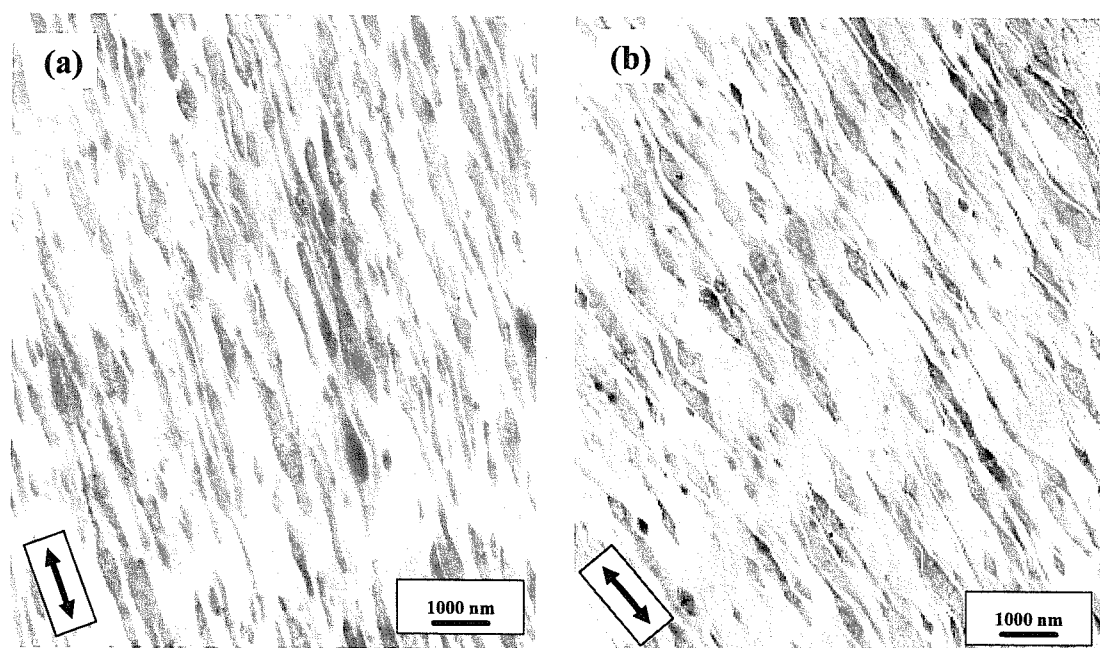
Figure 4: TEM micrographs of iPP/TPE blends in the edge view; (a) iPP/EPR30 and (b) iPP/EPR57blend, respectively. The arrow indicates FD.
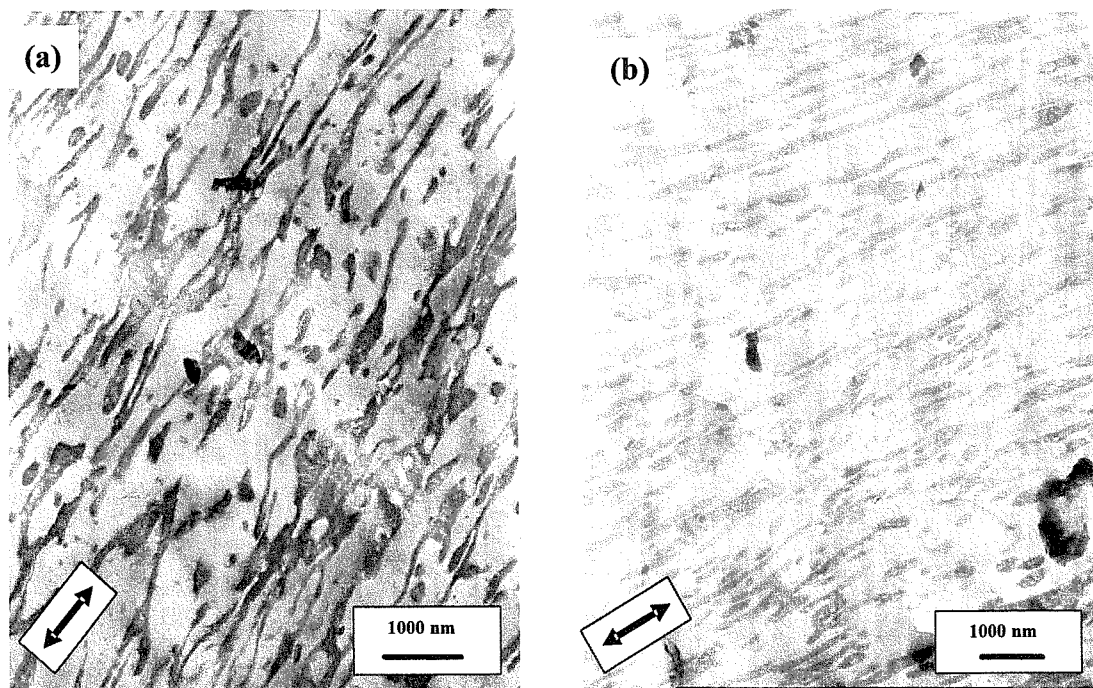
Figure 5: TEM micrographs of iPP/TPE blends in the end view; (a) iPP/HDPE and (b) iPP/LDPE blend, respectively. The arrow indicates TD.
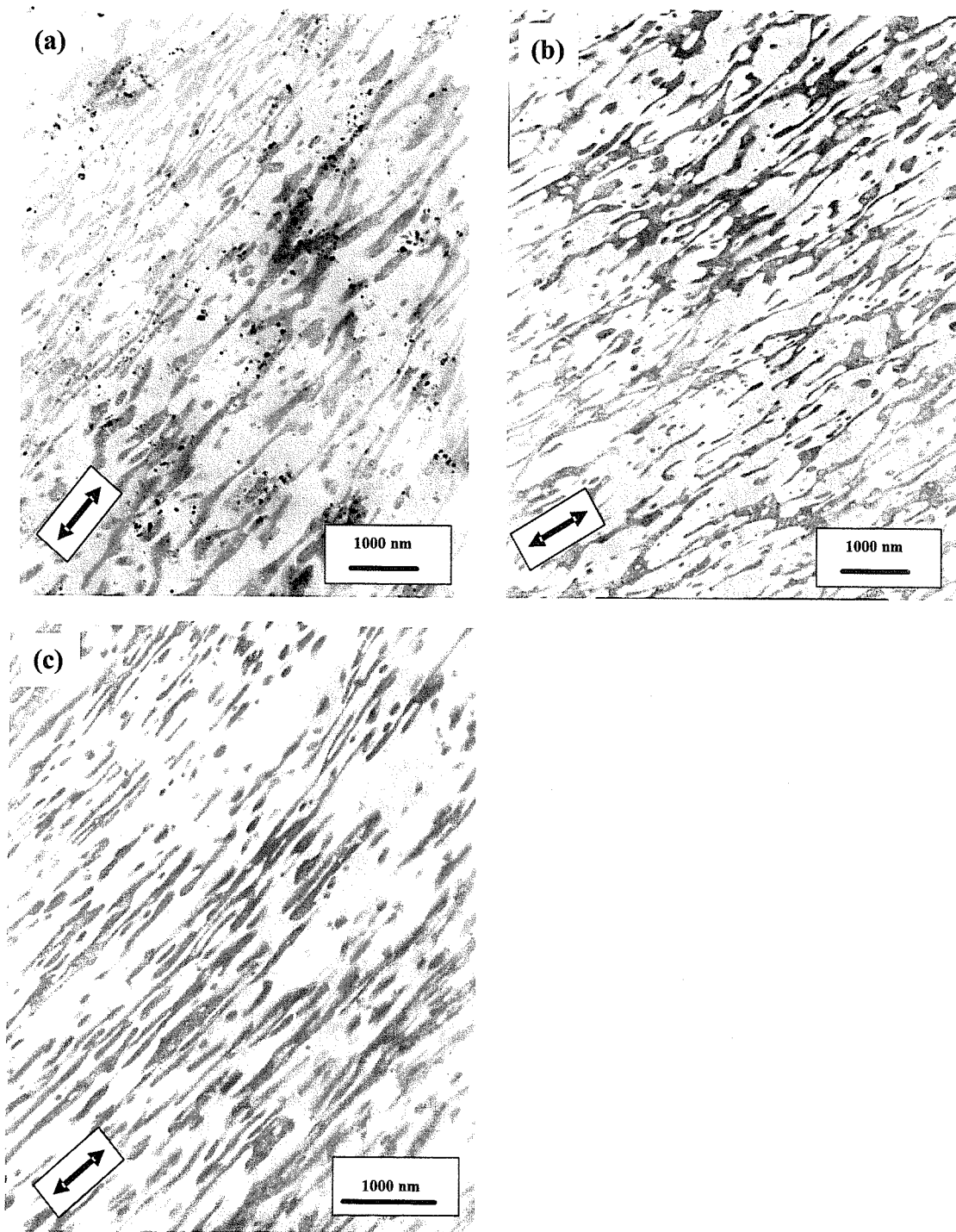
Figure 6: TEM micrographs of iPP/TPE blends in the end view; (a) iPP/EOR9, (b) iPP/EOR24 and (c) iPP/EOR30, respectively. The arrow indicates TD.

Figure 7: TEM micrographs of iPP/TPE blends in the end view; (a) iPP/EBR5, (b) iPP/EBR17, (c) iPP/EBR20 and (d) iPP/EBR32, respectively. The arrow indicates TD.

Figure 8: TEM micrographs of iPP/TPE blends in the end view; (a) iPP/EPR30 and (b) iPP/EPR57, respectively. The arrow indicates TD.
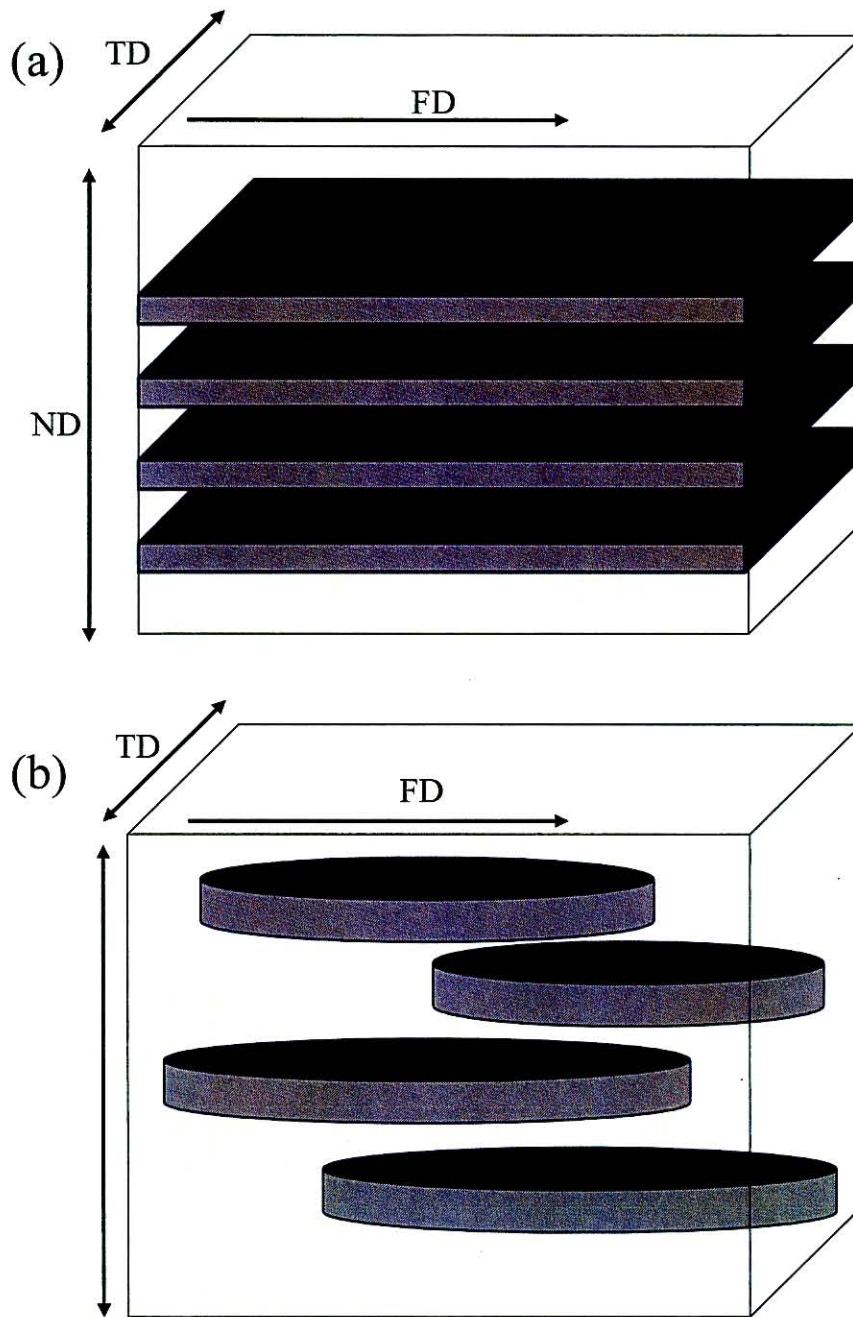
Figure 9: Schematic representation of arrangement of TPE inclusions in the blend; (a) iPP-PE, -EOR and EBR blends with the MFR ratio of TPE to iPP >1.0, i.e., the melt viscosity ratio of TPE to iPP < 1.0 and (b) iPP/EPR blends with the MFR ratio of TPE to iPP < 1.0, respectively.

3-2. Correlation of the CLTE with the co-unit type and its content in the TPE:

The average CLTEs (α^{obs}) for iPP/TPE binary blends along FD, TD and ND are plotted as a function of the co-unit content in the TPE, and they are shown in Figure 10(a)-(c), respectively.

In Fig. 10(a) (FD), all the CLTEs in the blends exhibit smaller values than that in the neat iPP and linearly decrease with the increase in the co-unit content in all cases. The similar trend is observed in the CLTE in TD (Fig. 10(b)). Note that the CLTE value in the iPP-EOR30 or iPP-EBR32 is ~ 6.0 (10^{-5} /°C) which is comparable to that in iPP-based composite with 25-30 wt% talc. These results are practically useful from the view point of the weight reduction of the molded articles so that we can achieve the CLTE decrease without higher density fillers.

Many researchers pointed out that, in the iPP/ethylenic TPE blends, the co-unit content in the TPE had great influence on mechanical or thermal properties, which was attributed to the variation of the TPE domain size and its distribution accompanied by the change in the affinity (compatibility) between the TPE and the iPP [10-17]. Yamaguchi et al. investigated the compatibility of EPR, EBR, and EHR (poly(ethylene-co-hexene)) having various co-unit content with iPP, and concluded that the co-unit ("α-olefin") rich TPE (>50 mol%) was miscible with iPP amorphous chains [15-17].

Hence, the CLTE trends as revealed in Fig. 10 would be also closely connected with the compatibility of the TPE with the amorphous chains of the base iPP.

It is found that the CLTEs in the PE, EOR and EBR blend series are on the same straight line irrespective of the difference in the co-unit types, whereas the CLTE values in the EPR blends are on the another line which shows gentler gradient toward the

variation of the co-unit content. As seen in the TEM photographs, the former blend series and the latter ones have different TPE morphologies, i.e., the lamella-like sheet and the ellipsoidal slab, respectively. Therefore, the difference in the CLTE by the variation of the co-unit content found between the EP blends and the other blends reflect on the difference of the arrays of the TPE. The lamella-sheet array is considered to be more effective for suppressing the thermal expansion in FD and TD compared to the ellipsoidal slabs array.

On the other hand, the CLTE values in ND (Fig. 10(c)) in the blends except for the iPP-HD show more than twice greater than that in the iPP. When considering a large experimental errors observed in the CLTEs along ND, these values may be regarded as being nearly constant (30-40 (10^{-5} /°C)) in spite of the difference in the TPE types and their co-unit content.
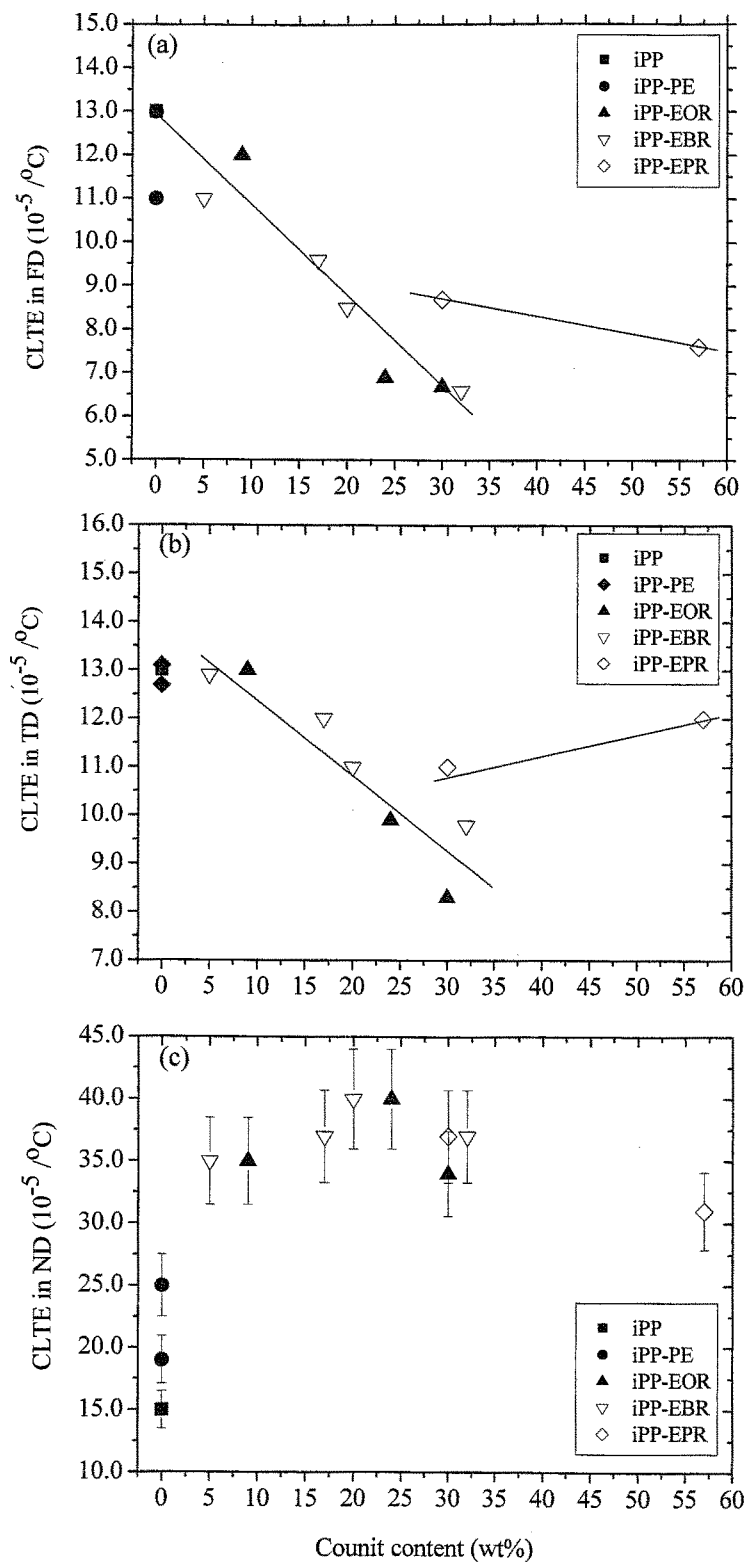
Figure 10: CLTE as a function of co-unit content in (a) FD, (b) TD and (c) ND, respectively.

3-3. Correlation of the CLTE with the Young modulus ratio:

Figure 11 shows the CLTE values as a function of Young's modulus ratio of TPE to iPP. As for FD (Fig. 11(a)) as well as TD (Fig. 11(b)), the CLTEs linearly increase with the Young's modulus ratio, i.e., the blends with softer TPEs give lower CLTEs. Note that the TPEs with the smaller Young's modulus have higher co-unit content, which may be partly due to decrease in rigid crystalline polyethylene sequences in the TPE chain by random incorporation of the co-unit. On the other hand, the CLTEs in ND remain constant ~ 30-40 (10^{-5} /$^{\circ}$C) irrespective of change in the Young's modulus ratio as shown in Fig. 11(c).

When considering the slab or lamella-sheet arrays of the TPE domains in the iPP matrix as shown in Fig. 9 in which the elastomers align parallel to both in FD and TD and in series in ND, thus the thermal stress, σ (=$\alpha l \Delta TE$) developed in FD and TD is thus the summation of a thermal stress for each component. As for ND, a thermal strain, ε (=$\alpha l \Delta T$) in ND is the summation of a thermal strain for each component [18]. The CLTE models composed of PP and TPE for each direction are derived as equations (3)-(5).

$$\alpha_{FD}(calc) = \frac{\alpha^{PP}_{FD}\phi^{PP} + \alpha^{E}\xi\phi^{E}}{\phi^{PP} + \xi\phi^{E}} \qquad (3)$$

$$\alpha_{TD}(calc) = \frac{\alpha^{PP}_{TD}\phi^{PP} + \alpha^{E}\xi\phi^{E}}{\phi^{PP} + \xi\phi^{E}} \qquad (4)$$

$$\alpha_{ND}(calc) = \alpha^{PP}_{ND}\phi^{PP} + \alpha^{E}\phi^{E} \qquad (5)$$

where $\xi = E^{E}/E^{PP}$. In these eqs., E and ϕ denote Young's modulus and volume fraction, and superscript PP and E represent iPP and TPE, respectively.

From eq. (5), the CLTE along ND is found to be independent of the Young's modulus of each component, which is consistent with the CLTE result in ND (Fig.

11(c)) showing no correlation with Young's modulus ratio.

On the other hand, eqs. (3) and (4) reveal that the CLTEs along both FD and TD are found to be proportional to ξ (Young's modulus ratio). It is agreeable to the CLTE trends observed in FD and TD (Figs. 11(a) and (b)). However, the minimum CLTEs for FD and TD achievable by these models when $\xi \rightarrow 0$ are equal to those corresponding to the neat iPP, α^{PP}_{FD} or α^{PP}_{TD}. In the experiments, all the blends exhibit lower CLTEs in FD and TD than the neat iPP, indicating that such simple composite models introducing the array effect composed of two components, iPP and TPE are insufficient for the real CLTE behaviors. It was also pointed out in Chap. 4.

3-4. iPP crystal orientation:

The iPP crystal orientation was an important factor for inducing the CLTE anisotropy in the lamella-like sheet arrangement as reported in Chap. 4. The author investigated the iPP orientation function of each blend along the each direction by WAXD pole figure. The results are summarized in Table III.

In all blends except for the b-axis in ND for the iPP-HD blend, each c-, a- and b-axis in the iPP crystalline phase are highly oriented along FD, TD and ND as revealed that the f_c, f_a and f_b show the largest value in FD, TD and ND, respectively. It indicates that the arrays of the TPE domains with lamella-sheets or ellipsoidal slabs induce the iPP crystal orientation.
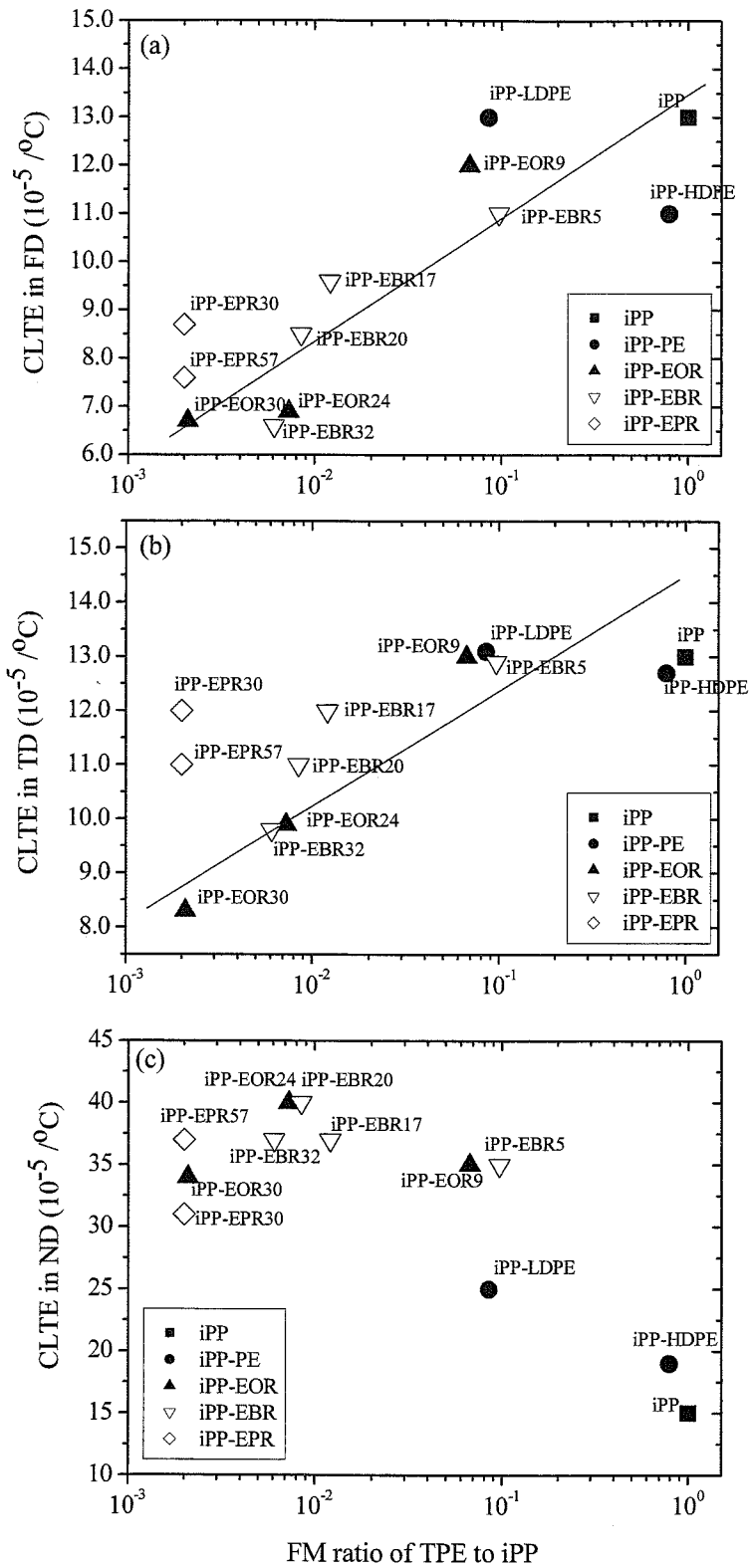
Figure 11: CLTE as a function of Young modulus ratio of TPE to iPP; (a) FD, (b) TD and (c) ND, respectively.

Table III Orientation function for each derection

	Herman's Orientation function f	Direction		
		FD	TD	ND
iPP	fa	-0.091	0.21	-0.17
	fb	-0.34	0.22	0.073
	fc	0.43	-0.43	0.095
iPP-HDPE	fa	-0.34	0.14	0.12
	fb	-0.027	0.094	-0.10
	fc	0.37	-0.23	-0.020
iPP-LDPE	fa	0.020	0.14	-0.22
	fb	-0.31	0.027	0.26
	fc	0.29	-0.17	-0.03
iPP-EOR9	fa	0.055	0.16	-0.25
	fb	-0.34	-0.072	0.38
	fc	0.29	-0.089	-0.13
iPP-EOR24	fa	0.020	0.19	-0.25
	fb	-0.30	-0.020	0.26
	fc	0.28	-0.17	-0.032
iPP-EOR30	fa	0.015	0.18	-0.25
	fb	-0.28	-0.02	0.21
	fc	0.26	-0.16	0.035
iPP-EBR5	fa	0.025	0.20	-0.25
	fb	-0.30	0.00	0.28
	fc	0.29	-0.20	-0.02
iPP-EBR17	fa	0.024	0.18	-0.23
	fb	-0.28	0.011	0.25
	fc	0.26	-0.19	-0.016
iPP-EBR20	fa	0.0030	0.18	-0.23
	fb	-0.32	0.034	0.22
	fc	0.31	-0.21	0.0052
iPP-EBR32	fa	-0.013	0.20	-0.24
	fb	-0.26	0.0010	0.23
	fc	0.25	-0.20	0.013
iPP-EPR30	fa	-0.061	0.24	-0.23
	fb	-0.31	0.076	0.15
	fc	0.37	-0.32	0.074
iPP-EPR57	fa	-0.0020	0.16	-0.21
	fb	-0.33	0.089	0.19
	fc	0.33	-0.25	0.022

4. Discussion

A conventional explanation [19-22] for creating the CLTE anisotropy by the deformed rubber domains was that the retraction by both the interfacial tension from the molten state TPE domains and the recovery strain from the rubber elasticity at higher temperature suppressed the thermal expansion of the matrix iPP in FD and TD but induces the thermal expansion preferentially toward ND instead. In other words, the larger the aspect ratio of the lamella sheet in the TPE domains was, the stronger the retraction and recovery strain were.

In addition, we pointed out in Chap. 4 that the orientation in the iPP crystalline region was a dominant factor to create the CLTE anisotropy because of the difference of the CLTE of each crystal axis; the CLTE along the a-axis $(\alpha l_a)\sim 8.8$, that along the b-axis $(\alpha l_b)\sim 19$ and that along the c-axis $(\alpha l_c)\sim -1.2$ $(10^{-5}$ $/^{\circ}C)$ [23]. The injection-molded iPP/EOR blend having the larger CLTE anisotropy (very low CLTE in FD whereas very high CLTE in ND) showed that the b-axis was exclusively oriented to ND and c-axis to FD.

In the following section, we will investigate the influence of these two factors on the CLTE anisotropy, in particular, the high CLTE in ND and very low CLTE in FD.

4-1. High CLTE in ND:

The correlation of CLTE in ND with the aspect ratio in the TPE inclusions and b-axis orientation function in ND is shown in Figure 12(a) and (b), respectively. The aspect ratio in the TPE was determined based on the TEM figures observed from the edge view.

It is found that the CLTEs in ND are roughly proportional both to the aspect ratio of the TPE domains and the b-axis orientation function, thus suggesting that the high CLTE in ND could be accounted for by the conventional explanations, the retraction and recovery strain from the TPE phase and the b-axis orientation in the iPP crystalline phase.

Considering the schematic models shown in Fig. 9 where the TPE phases arranged as lamella-sheets or ellipsoidal slabs are connected in series with the iPP phase and stacked normal to ND, the CLTE in ND would be greatly affected by a small variation of the thermal strain of both the iPP- and TPE phase because the total thermal strain in ND will be summation of the thermal strain from each phase. The TPE in ND will be less constrained by the rigid iPP matrix than that in FD and TD hence the TPE will expand preferentially to ND
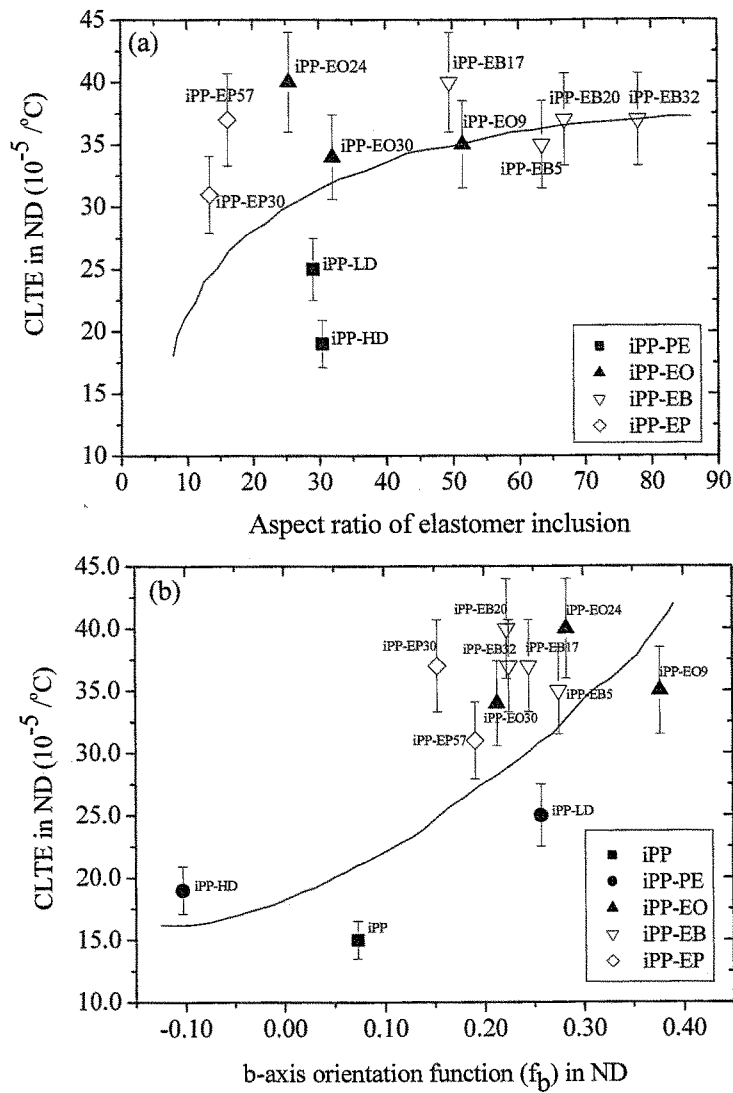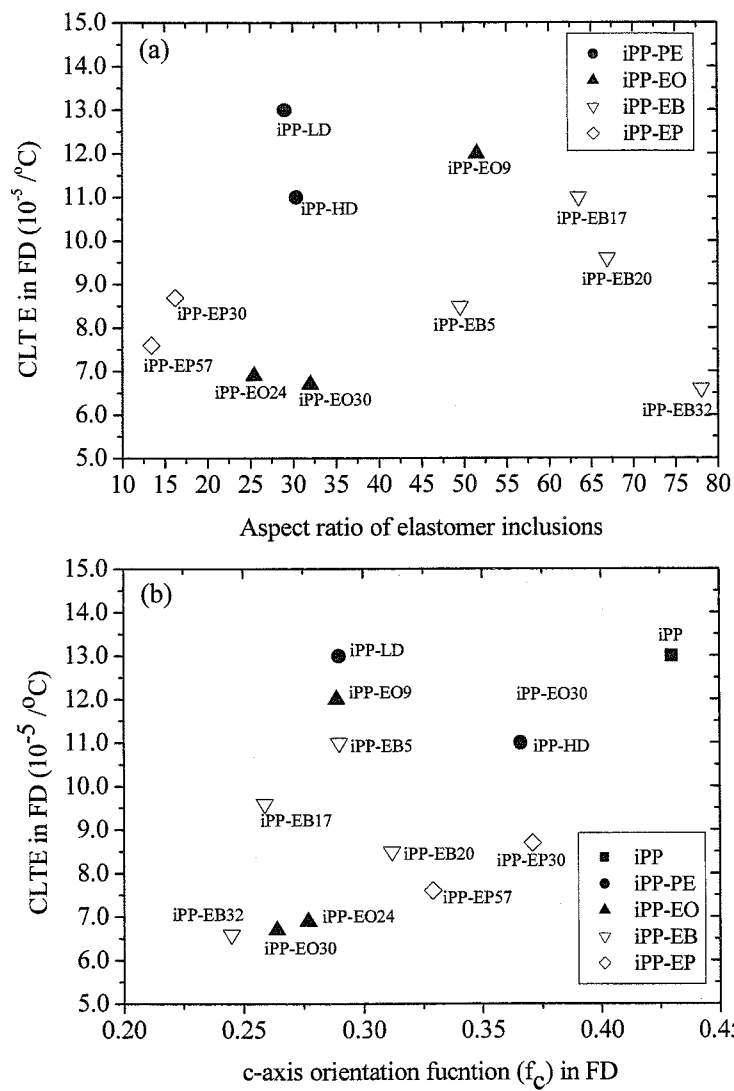
Figure 12: CLTE as a function of (a) aspect ratio of the TPE inclusions and (b) b-axis orientation function (f_b) in the ND, respectively.

4-2. Low CLTE in FD:

Similarly, the above discussion will be attempted on the CLTE in FD. The plots of the CLTE in FD against the c-axis orientation function in FD and the aspect ratio in the TPE are shown in Figures 13(a) and (b), respectively.

No correlation of the CLTE in FD with both the c-axis orientation function and the aspect ratio of the TPE are found. Only the retraction (recovery strain) from the TPE domains and the crystal orientation from the iPP is insufficient to explain the subtle differences in the CLTE in FD among the blends having similar TPE arrays like the lamella-sheets or ellipsoidal slabs.

The TPE inclusions arranged in parallel with the iPP in FD would be not so greatly influenced on the thermal strain in FD as on that in ND. Moreover, the retraction and recovery strain from the TPE along FD with temperature increase would be strongly restricted because the softer TPE phases are surrounded and strongly constrained by the rigid iPP matrix having more than 10 times higher Young modulus than that of the TPE (see Table 2).

Figure 13: CLTE as a function of (a) aspect ratio of the TPE inclusions and (b) c-axis orientation function (f_b) in the FD, respectively.

4-3. Role of the iPP amorphous region on suppression of the CLTE:

In Chaps. 2 and 4, the iPP amorphous regions were treated as being isotropic without taking both the allocation and orientation of them into consideration. The CLTE of the iPP amorphous region was reported to be 20-30 (10^{-5} /°C) [24] which is comparable to that of the TPE [24] and thus high enough to have a great influence on the CLTE of the entire blend system, depending on the allocation and orientation in the iPP amorphous chains. In addition, we also pointed out in Chap.4 that in lamella-like array, large discrepancy between the observed and calculated CLTE in FD still remained questionable, the cause of which would be due to the model itself composed of two components (PP and elastomer) system without consideration of the PP amorphous region, thus influence of solubility of the TPE into the iPP amorphous chains. In this study, the importance of the compatibility of the TPE is clarified according to the good correlation of the CLTEs in FD (or TD) with co-unit content (Fig. 10(a) (or (b)).

In the following discussion, we will investigate the correlation of the orientation and allocation of the PP amorphous region with the CLTEs, and the mechanism of suppressing the CLTE by use of the models introducing the influence of this region.

The CLTE in FD is plotted as a function of the orientation function of the PP amorphous region in FD (f^{FD}_{am}), which is shown in Figure 13.

The CLTE in FD is proportional to the f^{FD}_{am}, suggesting that the blends with the smaller f^{FD}_{am} give the lower CLTE. In addition, the smaller f^{FD}_{am}, almost isotropic (~0), is observed in the high co-unit TPE blends. The interlamella PP amorphous chains in the iPP matrix are somewhat oriented upon injection-molding [25]. Thus, the isotropic PP amorphous would be the one accommodated inside the TPE phase rather than in the iPP matrix. The orientation of the PP amorphous chains in the TPE phase accompanying

with the orientation of the TPE phase by the injection-molding could be neglected because the specimens were annealed above the melting point of the TPE before use.

There were a number of studies on the compatibility for the blends comprising iPP and ethylenic TPE [26-30], in which iPP and TPE were miscible (single phase) at an elevated temperature in high shear fields such as injection-molding, subsequently leading to phase-separation via spinodal decomposition (SD) in a quiescent state during the cooling process. The SD growth rate was greatly dependent on co-unit content in the TPE; slow for the blend with the high co-unit TPE while fast for that with the low co-unit one [26,30].

In this context, we investigated the SD and its demixing growth rate at various annealing temperatures for the iPP-EOR9 (low co-unit) and iPP-EOR30 (high co-unit), the details of which are shown in APPENDIX. Major conclusions are 1) both blends showing the modulated interconnected structures that are characteristic of the SD during phase separation, 2) both blends exhibiting LCST phase behavior, and 3) the demixing rate of the iPP-EOR9 (low co-unit) being much faster than that of the iPP-EOR30 (high co-unit).

Therefore, in the case of the blends with the high co-unit TPE, considerable amount of the iPP amorphous chains would be remained inside the TPE phase as a result of the slower SD growth arrested by the faster crystallization of the iPP matrix upon cooling process. On the other hand, as for the blends with the lower co-unit TPE, the iPP amorphous chains would be expelled from the TPE phase resulting from the faster SD growth before the crystallization will take place.

It is confirmed from the comparison of the TEM photographs at high magnification between the blends with higher co-unit and lower co-unit TPE. As typical

examples of them, the iPP-EOR30 (high co-unit TPE) and iPP-EOR9 (low co-unit one) are shown in Figure 15(a) and (b), respectively. They can provide the information about the interface between the iPP- and the elastomeric phase.
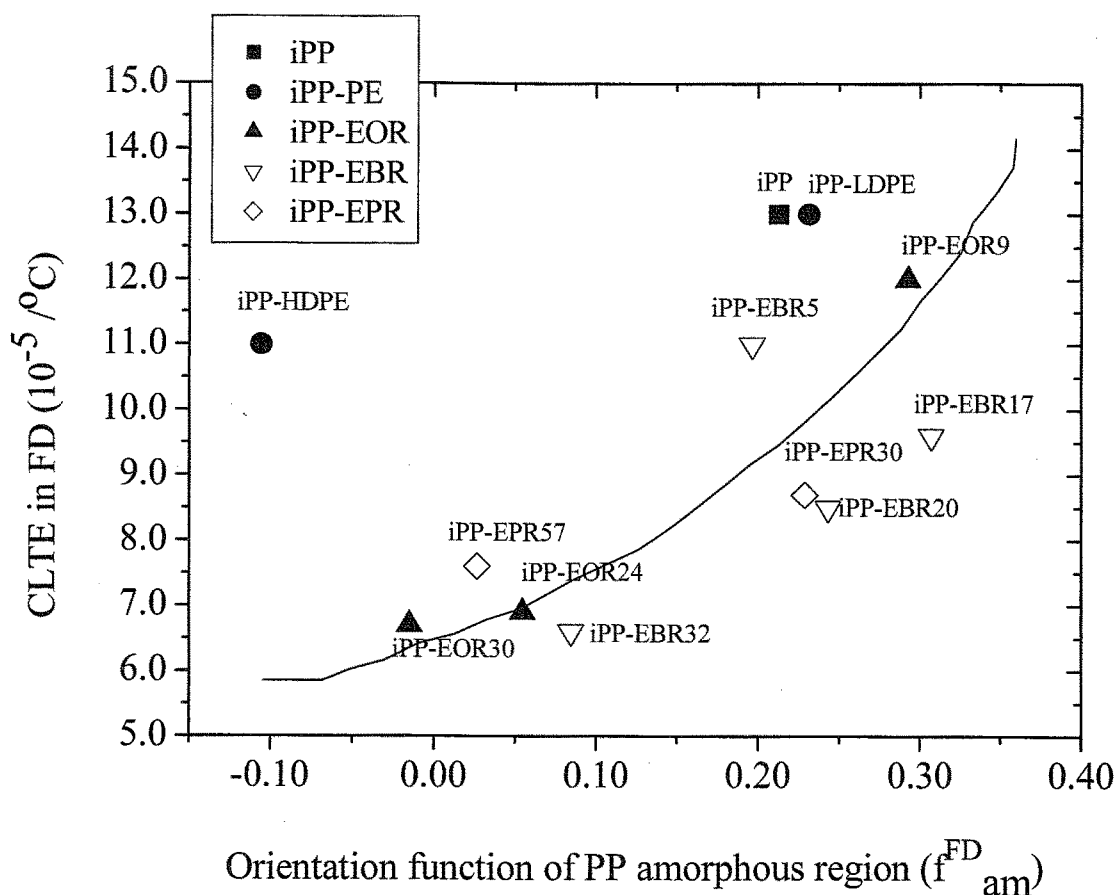
Figure 14: Correlation of CLTE along the FD with the orientation function of the iPP amorphous region

In the case of the iPP-EOR30 (Fig 15(a)), the iPP crystal lamellae deeply penetrate into the deformed elastomer, which is regarded as the epitaxial growth of the iPP crystals based on the elastomeric phase. Such structure would form as a result that the crystallization of the iPP residing inside the elastomeric phase would proceed faster than the phase-separation via the SD.

On the contrary, no indication of the epitaxial growth of the iPP crystals from the elastomer phase is found in the blend of the iPP-EOR9 (Fig. 15(b)). In this case, the phase-separation via the SD would take place much faster than the iPP crystallization.
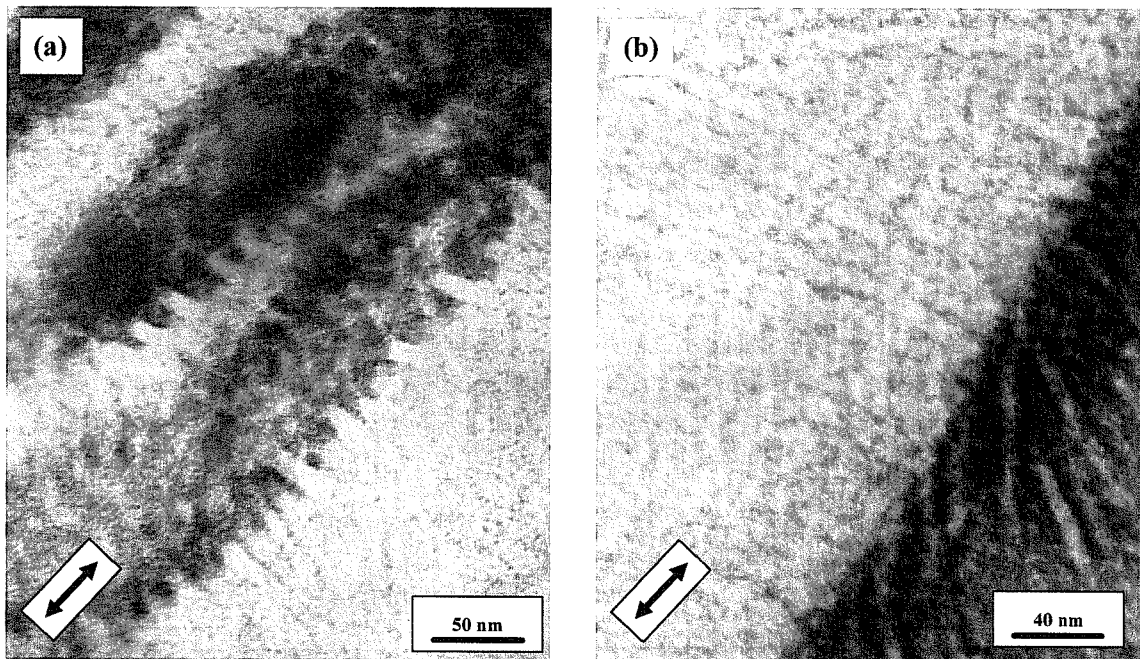

Figure 15: TEM photographs at high magnification in the
edge view; (a) iPP-EOR30 and (b) iPP-EOR9,
respectively. The arrow shown is the FD.

Moreover, the mobility of the iPP amorphous chains would change depending on where they would be inside the elastomeric phase or in the iPP matrix phase. It was investigated by the intensity of loss modulus (E") around the Tg for the iPP in the blend by DMTA; the high E" means high mobility of the iPP amorphous chains or vice versa.

Figure 16 shows the E" intensities around the Tg of the iPP for the iPP-EOR

blend series *vs* temperature. As increasing in the co-unit content of the EOR in the blend, the corresponding E" decreases, thus being indicative of decrease in the mobility of the iPP amorphous chains in the blend with higher octene content.

Figure 17 shows the peak intensity of E" around 0 °C for the all blends as a function of the co-unit contents. The peak intensities also decrease as increasing in the co-unit content. The mobility of the iPP amorphous chains confined in the higher co-unit TPE phase would be restricted by considering its arrays in parallel with the rigid iPP phase having 50-100 times higher Young modulus.
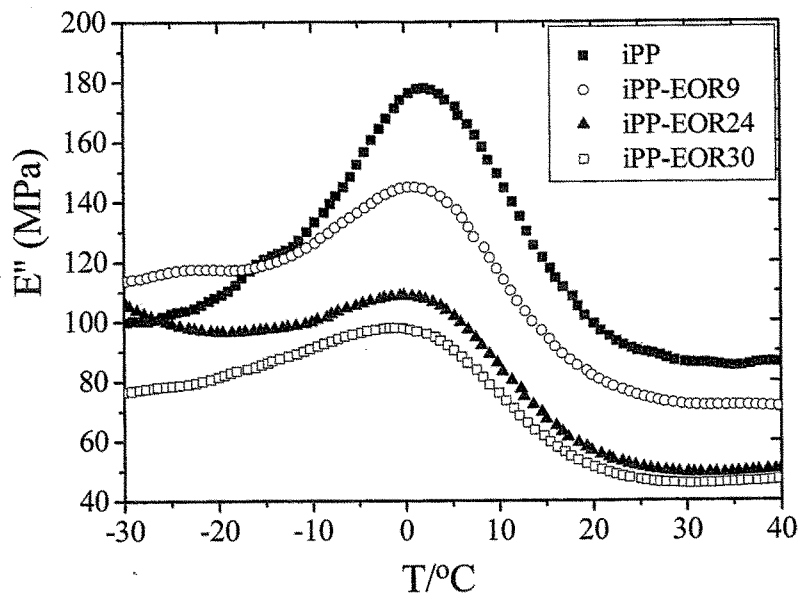
**Figure 16:** Loss modulus (E") of iPP-EOR blend series around 0 °C corresponding to Tg of iPP amorphous chains.
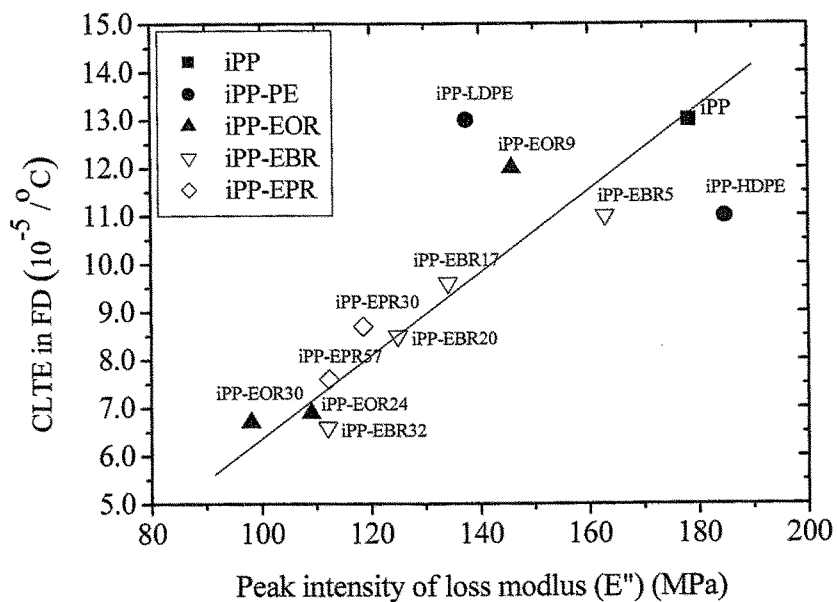
Figure 17: Correlation of CLTE along the FD with the peak intensity of loss modulus (E") around 0 °C.

From these consequences, we can assume the plausible mechanism for suppressing the CLTE along FD. The schematic models around the iPP and TPE neighborhood for the higher- and lower co-unit TPE blends are shown in Figure 18(a) and (b), respectively, where the allocation of each PP crystalline- (C), PP amorphous- (A) and TPE region (E) is demonstrated.

In the case of the high co-unit TPE blend, considerable amount of the PP amorphous chains would be included and confined in the softer TPE thus leading to being isotropic, and thermal expansion of the TPE as well as the included PP amorphous chains would be restricted by the rigid PP phase. Hence, the CLTEs in FD for this blend series are suppressed to be extremely low.

On the other hand, most of the PP amorphous chains in the low co-unit TPE blend would exist in the interlamella between the iPP crystalline phases, which may still have high CLTE due to little or no mechanical constraint.
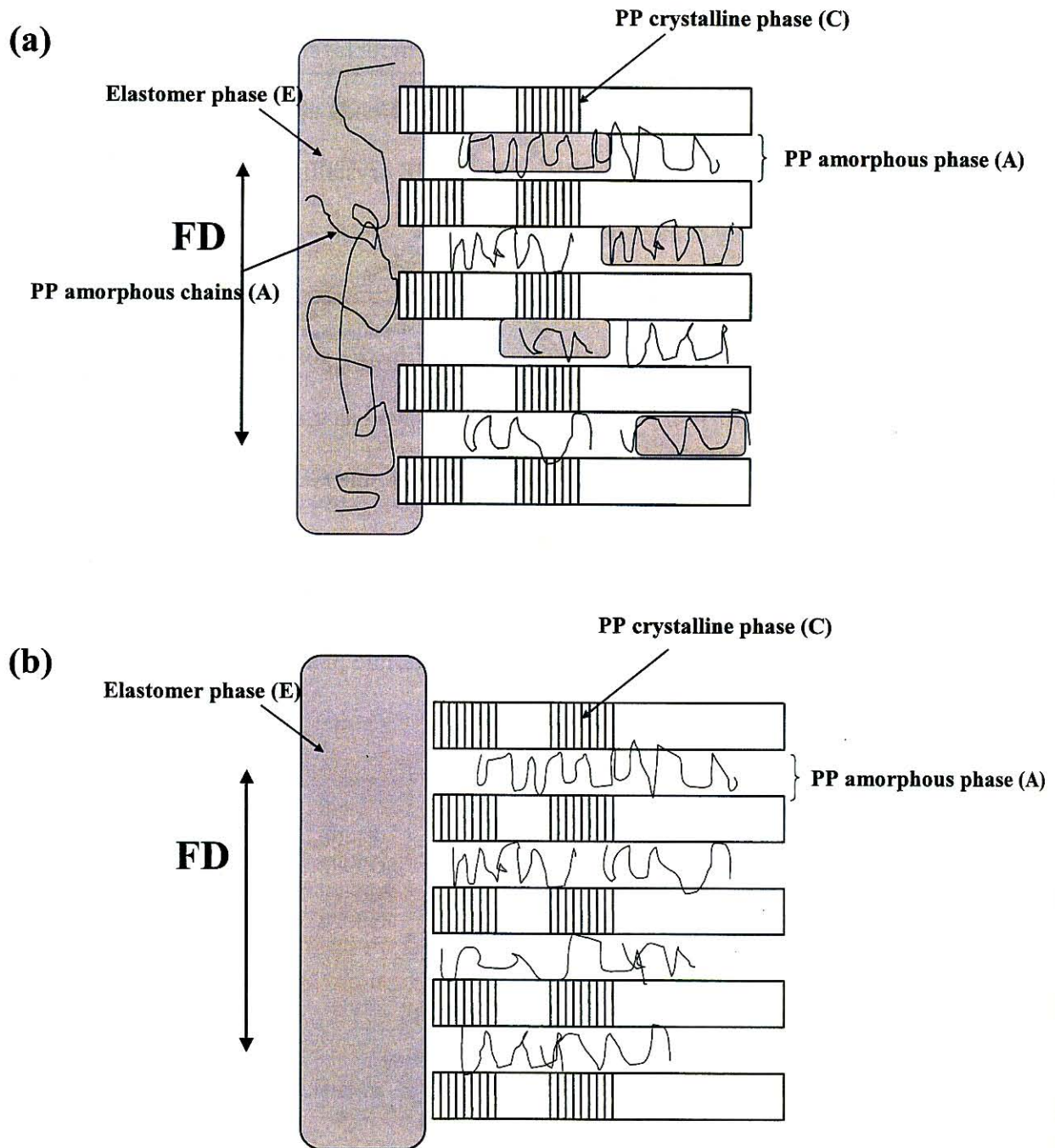
Figure 18: Schematic diagrams depending on the difference of the array of each A, C and E phase in the blend with (a) high co-unit TPE and (b) low co-unit TPE, respectively.
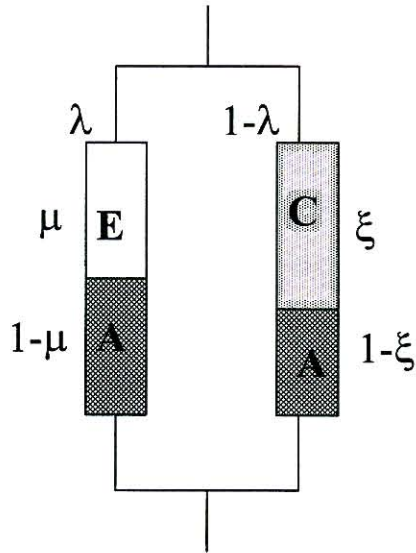
Figure 19: Mechanical model for interpreting the
CLTE behaviors of the iPP blend. Element A,
E and C correspond with the amorphous, the
crystalline and the elastomer region,
respectively. The value $\lambda\mu$ is equal to the
volume fraction of the elastomer region.

4-4. CLTE modeling:

Based on the arrays of the amorphous- (A) and crystalline phase(C) in the iPP,

and the elastomeric phase (E) as shown in Fig. 18, the mechanical model suitable for

interpreting the CLTE behaviors is shown in Figures 19. [1].

Parameter λ expressing the degree of parallelism and parameter μ and ξ for the

degree of series connection are defined as Fig. 19 and set $\lambda\mu=\varphi=0.3$ (volume fraction of

the TPE) and thus $(1-\lambda)\xi=(1-\varphi)X_c$. The λ, ξ and μ are satisfied with $0<\lambda<1.0$, $0<\xi\leq1.0$

and thus $0.3<\mu\leq1.0$. The allocation of the iPP amorphous region by the differences of

the co-unit of TPE is distinguished depending on μ and ξ; when $\mu=1.0$, all the amorphous region would belong to the iPP continuous phase, which would be the extreme case of the blend having the low co-unit TPE, and when $\xi=1.0$, all the amorphous region would be included in the TPE region in this case, which thus would be the one of that having the high co-unit TPE.

The calculated total CLTE (α^{calc}_{FD}) in the blend is given by equation (6)

$$\alpha^{calc}_{FD} = \frac{\lambda\{\mu\alpha_{FD,e} + (1-\mu)\alpha_{am}\}E^* + (1-\lambda)\{\xi\alpha_{FD,c} + (1-\xi)\alpha_{am}\}E^{**}}{\lambda E^* + (1-\lambda)E^{**}} \tag{6}$$

Here E* and E** are given by

$$E^* = \left(\frac{1-\mu}{E_{am}} + \frac{\mu}{E_e}\right)^{-1} \tag{7}$$

$$E^{**} = \left(\frac{1-\xi}{E_{am}} + \frac{\xi}{E_{FD,c}}\right)^{-1} \tag{8}$$

In these equations, α and E denote the CLTE and the Young's modulus, respectively. The subscript am, c, e and FD denote the iPP amorphous- (A), the iPP crystalline- (C), the TPE elastomer-region (E) and the direction FD, respectively. In these equations, the Young's modulus and the CLTE of each region per volume can be obtained by multiplying the volume fraction of each region, φ (the region E), $X_c(1-\varphi)$ (the region C) and $(1-X_c)(1-\varphi)$ (the region A) by the corresponding Young's modulus and CLTE.

Considering the anisotropy of the Young modulus and the CLTE of the orientation of each crystal axis in the iPP crystalline part, the $\alpha_{FD,c}$ and $E_{FD,c}$ are deduced as

$$\alpha_{FD,c} = f^{FD}{}_a \alpha_{c,a-axis} + f^{FD}{}_b \alpha_{c,b-axis} + f^{FD}{}_c \alpha_{c,c-axis} \qquad (9)$$

$$E_{FD,c} = f^{FD}{}_a E_{c,a-axis} + f^{FD}{}_b E_{c,b-axis} + f^{FD}{}_c E_{c,c-axis} \qquad (10)$$

In these equations, $f^{FD}{}_{a\ (or\ b,\ c)}$, $\alpha_{c,a-axis\ (or\ b-,\ c-axis)}$ and $E_{c,a-axis\ (or\ b-,\ c-axis)}$ denote the iPP crystal orientation function of each crystal axis along the FD, the CLTE of the each crystal axis ranging from 23 to 100 °C and the Young's modulus of each crystal axis, respectively. In addition, the elastic constant and the CLTE of the other A and E parts are assumed to be isotropic for simplification.

The CLTE and the Young's modulus of each crystal axis in eqs. (6) - (7) are regarded as fixed parameters; the following values are employed; $\alpha_{c,a-axis} \sim 8.2$, $\alpha_{c,b-axis} \sim 18.0$, $\alpha_{c,a-axis} \sim -0.41$ (10^{-5} /°C) and $E_{c,a-axis} \sim 2.9$ GPa, $E_{c,b-axis} \sim 3.2$ GPa [31], $E_{c,c-axis} \sim 40.1$ GPa [32]. The E_{am} and the α_{am} are 20 MPa [33] and 33 (10^{-5} /°C), respectively. The latter value, 33 (10^{-5} /°C) of the α_{am} can be obtained from inserting the Xc, $\alpha^{obs}{}_{FD}$, $f^{FD}{}_{a-,\ b-,\ and\ c-axis}$ of the iPP listed on Fig. 10 and Table I – III into equation (11).

$$\alpha_{am} = \frac{\alpha^{obs} - X_c(f^{FD}{}_a \alpha_{c,a-axis} + f^{FD}{}_b \alpha_{c,b-axis} + f^{FD}{}_c \alpha_{c,c-axis})}{1 - X_c} \qquad (11)$$

Using eq. (6), we can estimate the CLTE values for typical two blends; the iPP-EOR30 (high co-unit TPE) and the iPP-EOR9 (low co-unit TPE). The E_e, X_c, $f^{FD}{}_{a-,\ b-,\ c-axis}$ and $f^{FD}{}_{am}$ can be obtained from Table I, II, III and Fig. 14. The α_e values for each TPE are 23 (10^{-5} /°C) for EOR30 as one third of the measured volumetric thermal expansion determined with pressure-volume-temperature (PVT) analysis [24] and 37

(10^{-5} /°C) for EOR9 (measured).

For simplification, we assume $\xi=1.0$ for the CLTE calculation of the iPP-EOR30 blend and $\mu=1.0$ for that of the iPP-EOR9 blend, respectively. Inserting the necessary values into Eqs. (3)-(5) yields -1.6 (10^{-5} /°C) for the iPP-EOR30 and 8.9 (10^{-5} /°C) for the iPP-EOR9, respectively.

The latter value is in good agreement with the observed one, 12.0 (10^{-5} /°C), indicating that the model under the assumption $\mu=1.0$, i.e., no amorphous chains in the elastomeric phase, would be reasonably applied to the blend with low co-unit TPE. In contrast, the former value, -1.8 is underestimated against the observed one, 6.7 (10^{-5} /°C) when $\xi=1.0$. It is found to be $\xi\neq1.0$, i.e., some portion of the iPP amorphous region would be involved in the iPP crystalline region in the case of the iPP-EOR30. Obtaining the value of ξ by an experiment could improve the calculation accuracy.

4. Conclusions

In the iPP blend consisting of various types of ethylenic elastomers with different comonomer contents, the author clarified the following points;

1) By TEM observation, the shapes of the TPE in most of the blends were in the lamella-like sheet morphology stacked to ND.

2) The CLTE values in FD and TD were reversely proportional to the amount of the co-unit content in the TPE irrespective of its chemical composition. The CLTEs in ND except for the iPP-HD showed high and similar values (30-40 (10^{-5} /°C)) irrespective both of the chemical composition and the co-unit content of the TPE.

3) The high CLTEs in ND were closely related both with the aspect ratio of the TPE sheets and the b-axis orientation function of the iPP crystal along the ND. It was

found that the high CLTE in ND could be explained both by the retraction from the TPE and the thermal expansion of the iPP crystal axis.

4) The dependence in the CLTE in FD on the co-unit content showed strong correlation with the iPP amorphous orientation and the loss modulus peak intensity around Tg corresponding to the iPP amorphous chains. It indicated that the allocation of the iPP amorphous region played an important role on the CLTE along FD.

5. References

[1] Takayanagi M., Imada K. and Kajiyama T.; *J. Polym. Sci.; Part C*, 1966, **15**, 263

[2] Kunugi T., Ito T., Hashimoto M. and Ooishi M.; *J. Appl. Polym. Sci.*, 1983, **28**, 179

[3] Suzuki A., Sugimura T. and Kunugi T.; *J. Appl. Polym. Sci.*, 2001, **81**, 600

[4] Taylor G.I., *Proc. R. Soc. London,* 1934, **A134**, 501

[5] Cox R.G., *J. Fluid Mech.,* 1969, **37**, 601

[6] Tomotika S., Cox R. and Mason S.G., *J. Colloid Sci.,* 1972, **38**, 395

[7] Kim B.K. and Do H.I.; *J. Appl. Polym. Sci.*, 1996, **60**, 2207

[8] Vadas E.B., Goldsmith H.L. and Mason S.G.; *Trans. Soc. Rheol.*, 1976, **20**, 373

[9] Han C.D. and Kim Y.W.; *Trans. Soc. Rheol.*, 1975, **19**, 245

[10] Nomura T., Nishio T., Nakagawa M., Sumitomo T., Suzuki S.; *Kobunshi Ronbunshu,* 1994, **51**, 577

[11] Dao K.C.; *Polymer,* 1984, **25**, 1527

[12] Nomura T., Nishio T., Iwatami K., Yokomizo K., Kitano K. and Toki S.; *J. Appl. Polym. Sci.,* 1995, **55**, 1307

[13] Ling Z., Rui H., Liangbin L. and Gang W.; *J. Appl. Polym. Sci.,* 2002, **83**, 1870

[14] Xu J.T., Zhang Y.J., Guan F.X. and Fan Z.Q.; *J. Appl. Polym. Sci.,* 2005, **97**, 240

[15] Yamaguchi M., Miyata H. and Nitta K-h.; *J. Appl. Polym. Sci.,* 1996, **62**, 87

[16] Nitta K-h., Okamoto K. and Yamaguchi M.; *Polymer,* 1998, **39**, 53

[17] Yamaguchi M., Suzuki K-i. and Miyata H.; *J. Polym. Sci. Part B; Polym. Phys.,* 1999, **37**, 701

[18] Burkley C.P. and McCrum N.G.; *J. Mater. Sci.,* 1973, **8**, 1123

[19] Yamamori Y., Iwamoto K. and Miwa Y.; *JSAE Rev.,* 1991, **12**, 61

[20] Wu G., Nishida K., Takagi K., Sano H. and Yui H.; *Polymer*, 2004, **45**, 3085

[21] Nomura T., Nishio T., Taniguchi H., Hirai I. and Hisamura N.; *KobunshiRonbunshu*, 1994, **51**, 505

[22] Koizumi J., Okumoto T., Mizutani H. and Shichida Y.; *Seikei-Kakou*, 1994, 6, 697

[23] Gu F., Hikosaka M., Toda A., Gosh S.K., Yamazaki S., Arakaki M. and Yamada K.; *Polymer*, 2002, **43**, 1473

[24] Zoller P. and Walsh D.J.; *"Standard Pressure-Volume-Temperature Data for Polymers"*, Technomic Publishing Co. Inc., 1995

[15] Choi D. and White J.L.; *Polym. Eng. Sci.*, 2002, **42**, 1642

[26] Sano H., Matsuda M., Sato H. and Nomura T.; *Kobunshi Ronbunshu*, 1999, **56**, 563

[27] Inaba N., Sato K., Suzuki S. and Hashimoto T.; *Macromolecules*, 1986, **19**, 1690

[28] Inaba N., Yamada T., Suzuki S. and Hashimoto T.; *Macromolecules*, 1988, **21**, 407

[29] Lim S.W., Lee K.H. and Lee C.H.; *Polymer*, 1999, **40**, 2873

[30] Lee J.K., Lee J.H., Lee K.H. and Jin B.S.; *J.Appl. Polym. Sci.*, 2001, **81**, 695

[31] Sakurada I., Ito T. and Nakamae K.; *J.Polym. Sci.: Part C*, 1966, **15**, 75

[32] Tashiro K., Kobayashi M. and Tadokoro H.; *Polym. Prepr. Jpn.*, 1986, **35**, 3266

[33] Inoue T., Mizukami Y., Okamoto H., Matsui H., Watanabe H., Kanaya T. and Osaki K.; *Macromolecules*, 1996, **29**, 6240

APPENDIX

The liquid-liquid (L-L) phase separation of the injection-molded iPP-EOR9 and iPP-EOR30 blend was investigated using phase-contrast optical microscope (PCM) at various demixing temperatures (T_d), 180, 200, 220 and 250 $^{\circ}$C.

The specimen with ~50 μm in thickness was cut out from edge view of the mother slab, then being interposed between two glass plates. The specimen was heated to the desired demixing temperature above the melting temperature of the iPP (165 $^{\circ}$C) for 5, 10, 30, 60, 180, 600, 1800, 3600 sec and was then quenched at -78 $^{\circ}$C. The quenched specimen was observed by PCM at room temperature.

Figures 20 and 21 display the time evolution of morphology under PCM at 180, 200, 220 and 250 $^{\circ}$C of T_d for the iPP-EOR30 and iPP-EOR9, respectively. As can be clearly seen, the modulated interconnected structures characteristic of L-L spinodal decomposition develop and coarsen with time for both blends. In addition, the time resolved phase-separated domain size increases with the T_d, indicating that both blends have a LCST phase behavior.

T_d=180 ºC T_d=200 ºC

30s   30s

180s   180s

600s   600s

20 µm
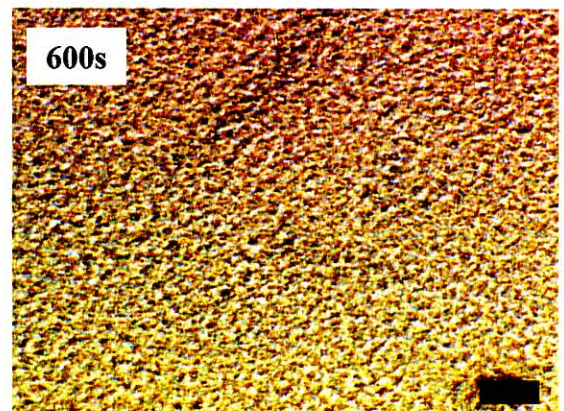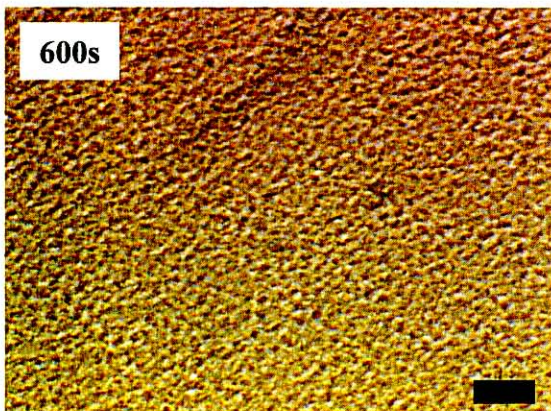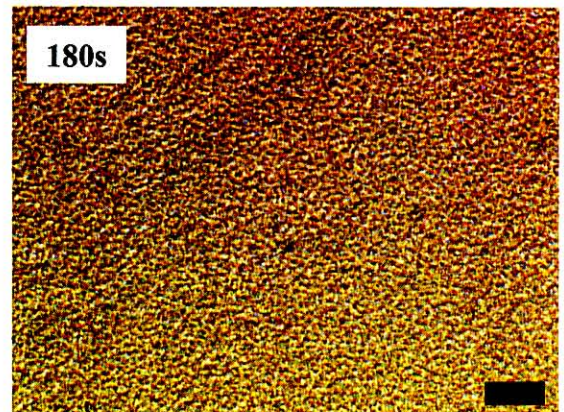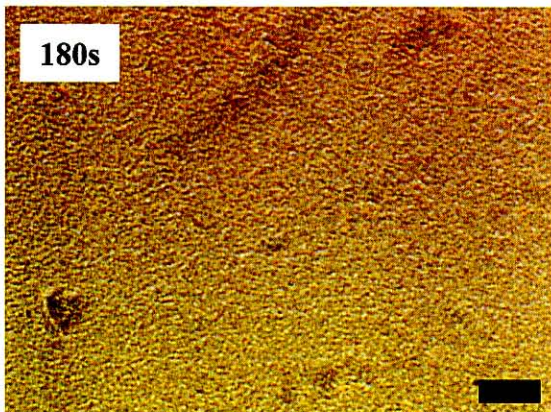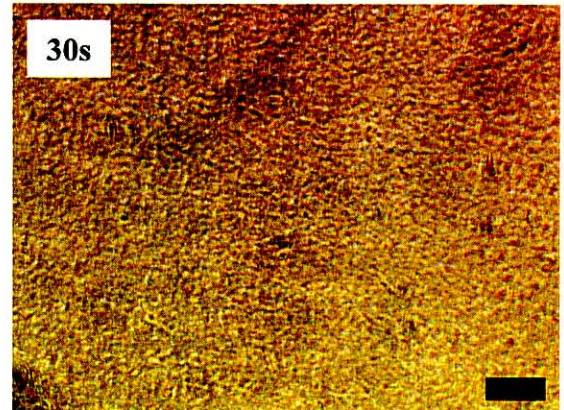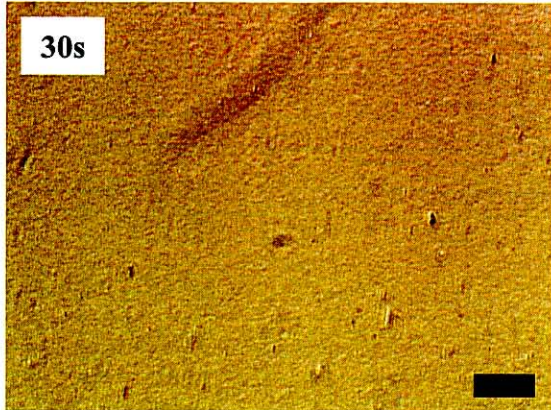
Figure 20: Time evolution of phase-contrast images for the iPP-EOR30 demixed at T_d=180, 200, 220 and 250 ºC, respectively. The scale bar represents 20 µm.

$T_d = 220\ ^oC$ $T_d = 250\ ^oC$

Figure 20 (Contnued) :   20 μm

T_d=180 °C   T_d=200 °C

Figure 21: Time evolution of phase-contrast images for the iPP-EOR9 demixed at T_d=180, 200, 220 and 250 °C, respectively. The scale bar represents 20 μm.

20 μm

T_d=220 ^{o}C $\quad\quad\quad$ T_d=250 ^{o}C

30s 30s

180s 180s

600s 600s
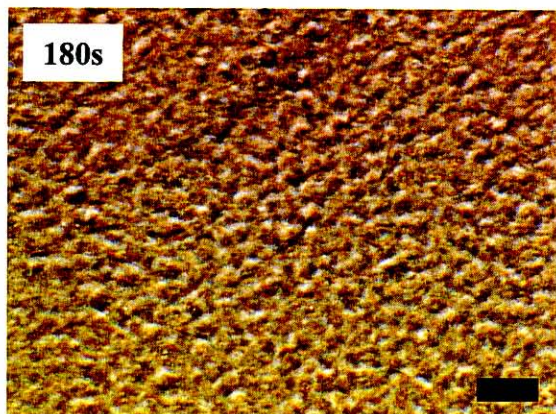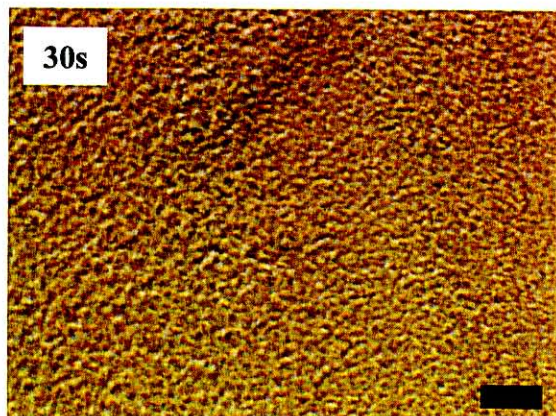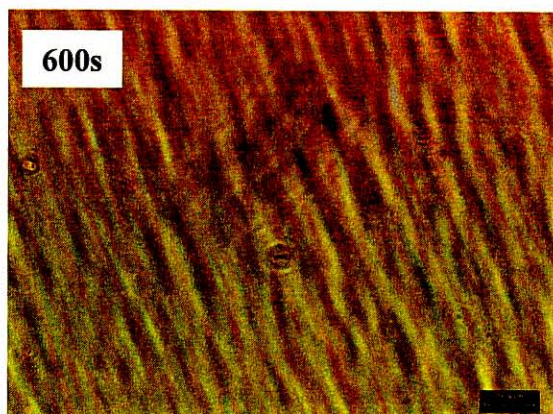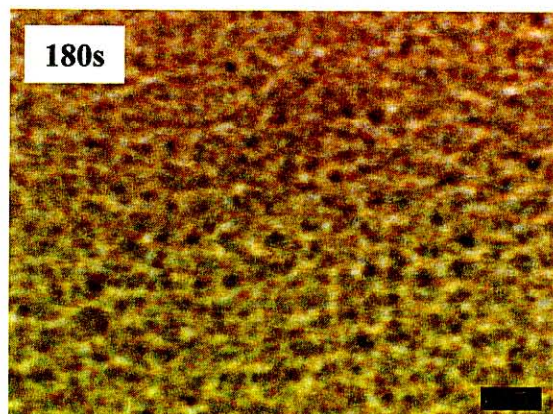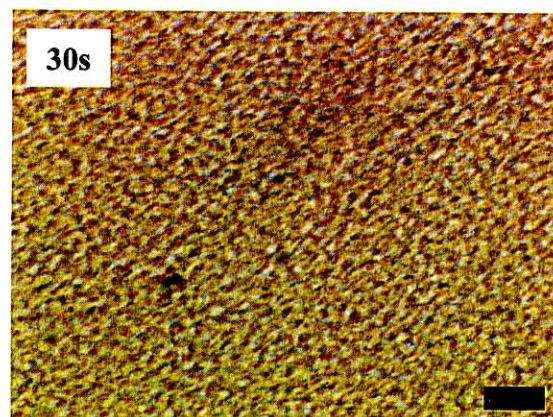
Figure 21(Continued) : $\quad\quad\quad\quad\quad\quad\quad$ 20 µm

128

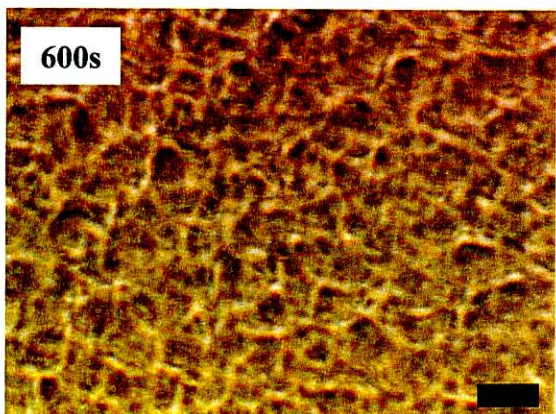Figure 22 shows the time evolution of the interconnected/periodic distance (λ) at various demixing temperatures. Here, we employed the length of the elastomeric phase interposed between the PP phases as the value of λ.

At any demixing temperatures, the λ of the iPP-EOR30 is smaller than that of the iPP-EOR9, suggesting the slower growth of SD.
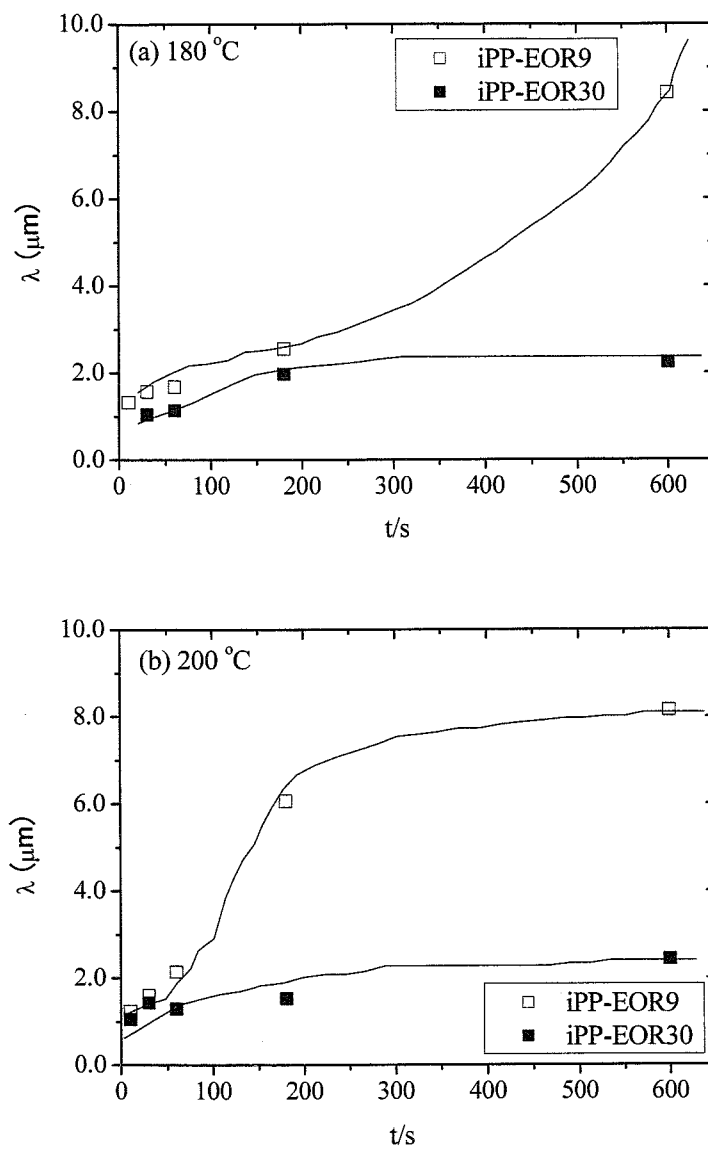
Figure 22: Change in the periodic distance with time at various demixing temparatures; (a) 180 °C, (b) 200 °C, (c) 220 °C and (d) 250 °C.
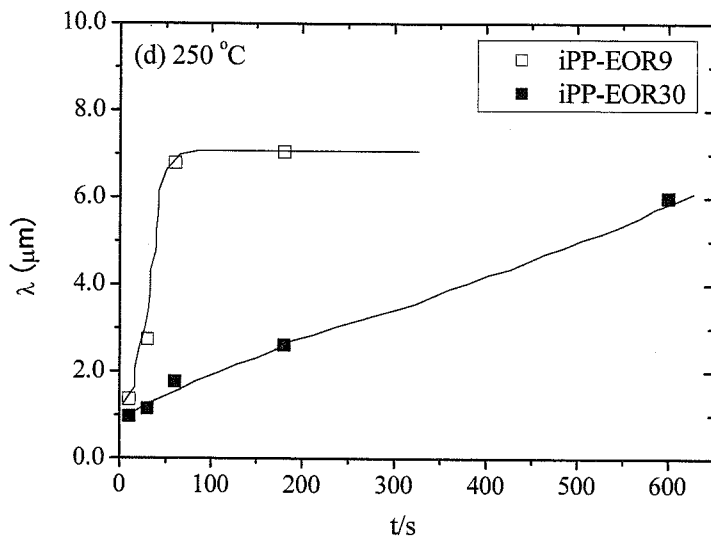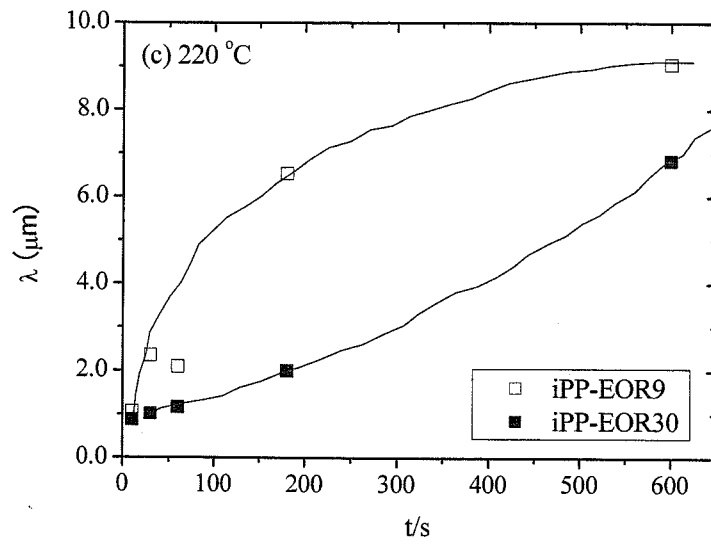
Figure 22 (Continued):

Chapter 6:

Real-time Morphological Observation of Injection-molded iPP/EOR Blend at Elevated Temperatures using Atomic Force Microscopy (AFM)

1. Introduction

In Chap. 2, the author reported the differences of the CLTE behaviors between the injection-molded iPP/EOR blend and the compression-molded one. In the case of the injection-molded blend, the CLTE in the FD increased with increasing temperature in a quite unusual manner; an inflection point emerged around 50 °C and above this temperature the CLTE began to drop drastically. On the other hand, the CLTE in the SD of the compression-molded monotonically increased with temperature increase.

TEM observation reveled that the two blends had different EOR morphologies, the lamella-sheet array for the injection blend and the spherical array for the compression one. Such morphological difference would induce the difference in the CLTE behaviors between the two blends. Hence, elaborate morphological observation would be a key for elucidating the mechanism of the CLTE difference.

Using TEM, remarkable insights about phase separated structures and lamella structures of semi-crystalline polymer/rubber blends have been obtained [1-2]. However, this technique can not be used to investigate real time morphological changes with temperature variation.

132

Atomic force microscopy (AFM) has become a powerful tool of investigation of polymer surfaces. One of the main advantages of using the AFM is that we can obtain the images with a molecular scale resolution at various temperatures [3-7].

In this study, we investigated the morphological changes of the two iPP/EOR binary blends with each having different shapes of the EOR domains at elevated temperatures using atomic force microscopy (AFM) equipped with a heater accessory. It was found that the iPP amorphous region in the interlamella developed differently depending on the EOR shapes.

2. Experimental

2-1. Raw material Characteristics:

Isotactic polypropylene (iPP) used in this study, which was kindly supplied by SunAllomer, had 5,600 Pa·s of a zero shear viscosity (η_m^*) at 210 °C, 98.5 % of isotactic index on the basis of pentad sequences [mmmm] determined by ^{13}C-NMR and 165 °C of melting temperature with differential scanning calorimeter (DSC) at a scanning rate of 10 °C/min. Poly(ethylene-co-octene) (EOR), which was purchased from Dow Chemical, had 24 wt% of octene content, 455 Pa·s of zero shear viscosity (η_i^*) at 210 °C, 55 °C of melting temperature by DSC. The zero shear viscosity of each material was obtained by the same procedure described in Chap. 4.

2-2. Sample preparation:

The blend sample consisting of 70/30 vol/vol of iPP/EOR having 0.085 of a viscosity ratio η_i^*/η_m^*, was prepared according as the similar procedures described in Chap. 2. The resulting blend was fabricated to obtain the two slab-shaped specimens by

different two molding methods; injection- and compression-molding. The injection-molded specimen was also obtained by the same procedures as described in Chap. 2.

On the other hand, the compression-molded slab was prepared by plasticizing at 230 °C for 5minutes followed by hot-pressing under 10 MPa and then by cooling at 30 °C at 5 MPa. The definition of the directions and cross sections of the resulting slab obtained by the injection or the compression was illustrated in Figures 1(a) and (b), respectively. We abbreviated each specimen as Blend-I for the injection-molded specimen and Blend-P for the compression-molded one. The each slab was annealed at 100 °C for over 24 hours to remove a thermal strain and residual stress and to enhance secondary crystallization. Thus, the influences of shrinkage by the crystallization and excess expansion due to relieving stress on CLTE values and AFM images can be neglected.

The thermal properties of each specimen were carried out with a differential scanning calorimetry (DSC) (DSC-7; Perkin Elmer) ranging from 23 to 230 °C at a scanning rate of 10 °C/min. In the Blend-P, only one peak at 165°C corresponding to the T_m of iPP was observed. In the Blend-I, there had a small but distinct peak at 37 °C in addition to the peak at 165°C. The peak at higher temperature (165 °C) observed in both types of specimens was identical with the T_m of the raw material iPP, indicating that the EOR is immiscible in the crystalline region of the iPP. The peak at 37 °C in the Blend-I would correspond to the T_m of the EOR, being much lower than that of the raw material EOR (55 °C).
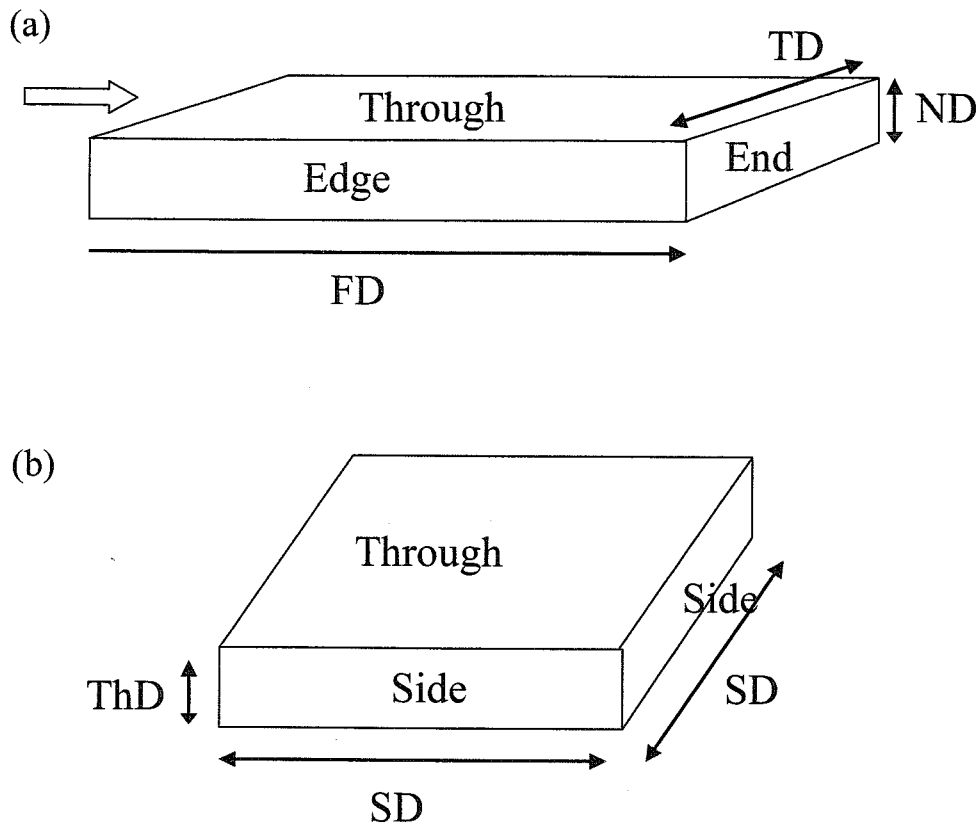
Figure 1 : Nomenclature of direction and cross section.
(a) injection-molded specimen; For directions, FD (parallel to flow direction) , TD (transverse to flow direction) and ND (normal to flow direction). For cross sections, Edge- (parallel to FD), End- (parallel to TD) and Through view (parallel to ND).

(b) compression-molded specimen. For directions, SD (parallel to width or length direction) and ThD (parallel to thickness direction). For cross sections, Side view (parallel to SD) and Through view (parallel to ThD)

2-3. Real time observation of morphological change with temperature variation by AFM:

Morphological changes at elevated temperatures at room temperature (~23°C), 40, 60, 80, 100 and the returned room temperature rapidly cooled from100°C, were observed under atmospheric condition using an atomic force microscope (AFM) (Nanoscope IV MultiMode AFM; Veeco) with a high-temperature heater accessory. The measurement was started after keeping the test temperature for 20min, the time of which was long enough to make the sample and the cantilever reach to the test temperature [9]. The AFM images were taken in tapping mode using a silicone cantilever with a spring constant of 2.8 N/m and resonance frequency of 75 kHz. Both height and phase images were taken simultaneously. All data were collected with 512×512 pixels per image. Typical scan rates, set point amplitude ratio and scan size during recording were 1.0 Hz, 0.7-0.8 and 500×500 nm, respectively. The flat surfaces, which were taken from a core layer in the edge view parallel to the FD for Blend-I and in the side-view for the Blend-P, were obtained by cryo-microtomed at −100°C with a diamond knife. Note that the observation by AFM was carried out in a core layer not a skin layer.

2-4. Determination of crystallinity of the iPP in the blend at different initial temperatures:

The difference in the weight fraction of the crystallinity (X_c) of the iPP in each blend at each temperature stage, r.t., 40, 60, 80 and 100 °C, for the above AFM measurement was determined from the division of the heat of fusion per gram (ΔH) of the iPP in the blend by that of perfect crystalline iPP, 209 (J/g) [10]. The ΔH was

obtained using DSC measurement by comparing the area of endothermic peak at around 165 °C of the blend sample and the standard. The procedures were as follows; the sample sealed in an aluminum pan was heated from r.t. up to each target temperature at a heating rate of 10 °C/min and held at this temperature for 20 min., then reheated up to 230 °C at a heating rate of 10 °C/min.

2-5. Long period change in iPP lamellae with temperature change:

The variation of long period between PP lamellae with temperature variation was measured with a small angled X-ray scattering (SAXS) (NanoStar; Bruker) equipped with a high temperature accessory, which was operated at 45 kV and 22 mA. The X-ray was irradiated normal to the edge view in the Blend-I and the side view in the Blend -P. Typical collection time was 120 min. Test sample was taken from a core layer in the edge view with a 1mm thickness and then mounted on a specimen holder and then heated at testing temperature. The testing temperatures were chosen as r.t. (~25 °C), 40, 60, 80, 100 °C and the r.t. cooled from 100 °C. The measurement was started after maintaining the testing temperature for more than 30 min which would be long enough for the specimen to reach the testing temperature. Data was collected through a two dimensional (2D) position sensitive proportional counter (2D-PSPC).

2-5. Determination of apparent activation energy by dynamic mechanical thermo-analysis (DMTA):

The apparent activation energies of the amorphous- and the crystalline region of the iPP in each blend were obtained based on the linear dynamic mechanical analysis which was made using a dynamic mechanical thermo-analyzer (DMTA) (RSAIII; TA

Instruments) on a tensile mode. The rectangular specimen with 30 (length) by 3.0 (width) by 0.4 (thickness) mm^3 was cut out from the slab and mounted in a sample holder in such a way that the "length" direction, thus the oscillatory strain direction, coincided with the FD or the SD. The loss moduli (E") were monitored ranging from -80 and 140 °C at various frequencies (f) of 0.5, 1.0, 2.0, 5.0, 10 and 50 Hz, and at a heating rate of 4.0 °C/min. The dispersion peaks associated with the iPP molecular motion were observed at around 0 and 80 °C. The peak at around 0 °C was the primary dispersion (α_a) ascribed to the micro-Brownian motion of amorphous chains and the higher peak (80 °C) belonged to the crystalline dispersion (α_c) caused by internal friction within the crystalline region [11-12]. The apparent activation energy (ΔH^*) of the iPP amorphous or crystalline region was given by inserting a gradient from the plot of log f as a function of reciprocal temperature (1/T) of the corresponding E" peak to α_a or α_c at a given frequency f into equation (1) [13].

$$\Delta H^* = -2.303 R \frac{d \log f}{d(\frac{1}{T})} \qquad (1)$$

Here, R denotes gas constant, 8.31 J/Kmol.

2-6. Linear thermal expansion coefficient (CLTE):

The CLTE evaluation was carried out according as the procedure in Chap. 2. The measured direction was the FD for the Blend-I and SD for the Blend-P.

3. Results:

3-1. Difference in the morphological behaviors at higher temperatures between the injection and compression-molded specimen by AFM :

Figure 2 shows AFM phase image of the edge view of the Blend-I at various temperatures. In general, the phase contrast is obtained due to the phase lag and frequency shift of the cantilever oscillation relative to drive signal of the cantilever. In these figures except for Fig. 2(g) where inverse trend of the phase contrast is obtained, dark regions represent soft or adhesive regions as a result of the phase lag and hence bright regions indicate hard or low adhesive regions. In the present system, both the elastomeric and the iPP amorphous phase correspond to the high-adhesive region and the iPP crystalline phase to the hard or low-adhesive one.

At room temperature with low magnification (Fig. 2(a)), it can be found that the dark regions corresponding to EOR-rich phases are clearly observed resulting from a phase separation and they are highly deformed along the FD, forming co-continuous structures with the iPP matrix. In immiscible or partially miscible binary blends with less than 1.0 of a viscosity ratio, minor component having lower viscosity was highly deformed along FD and formed co-continuous structures due to shear force followed by elongational force upon injection-molding [14-16]. The present system is typical case in this pattern. In bright regions, i.e., iPP-rich phases, stripe patterns corresponding to the iPP lamellae are clearly observed. The lamellae are aligned perpendicular to the deformed EOR phases.

At higher magnification (Fig. 2(b)), dark stripes corresponding to the iPP amorphous regions can be clearly observed between the interlamellae in the iPP matirx.

When increasing temperature up to 40°C (Fig. 2(c)), there is no change in the EOR rich regions. However, a drastic change in the iPP matrix occurs above this temperature; the iPP lamella regions seem to spread, being wider in their thickness, whereas the amorphous regions seem to reduce, being narrower. This trend seems to be further facilitated as successively increasing in temperatures up to 60 and 100 °C (Fig. 2(d)-(f)); the amorphous regions can't be observed at 100 °C (Fig. 2(f)).

When returning to room temperature from 100°C (Fig. 2(g)), the phase contrast is inverted, i.e., each EO- and iPP-rich phase appears as the bright and the dark region with a web-like structure consisting of some streaks in the iPP-rich phase.

The above phase inversion might be caused by a phase lag as a result that the tip contacts with large bumps of the EOR subjected to successive melt and solidification or might result from the change of the tip-sample interaction due to deposition of the molten EOR onto the tip.
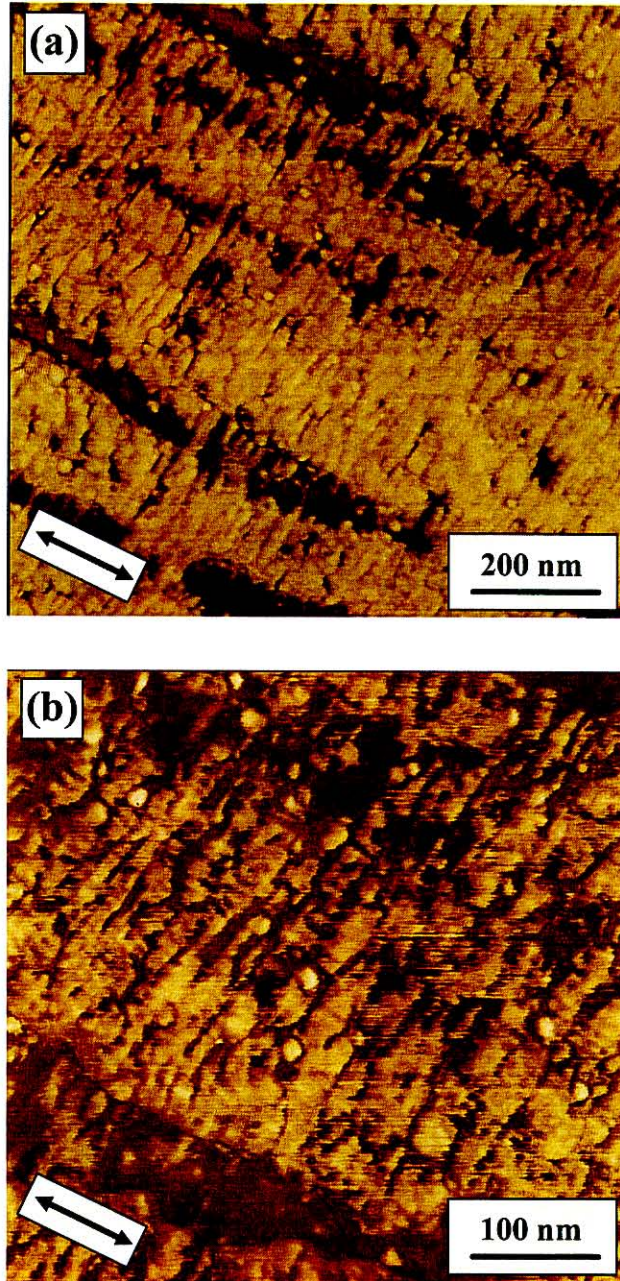
Figure 2: AFM phase images of Blend-I at low magnification (a) and at high magnification (b). The arrow indicates FD.
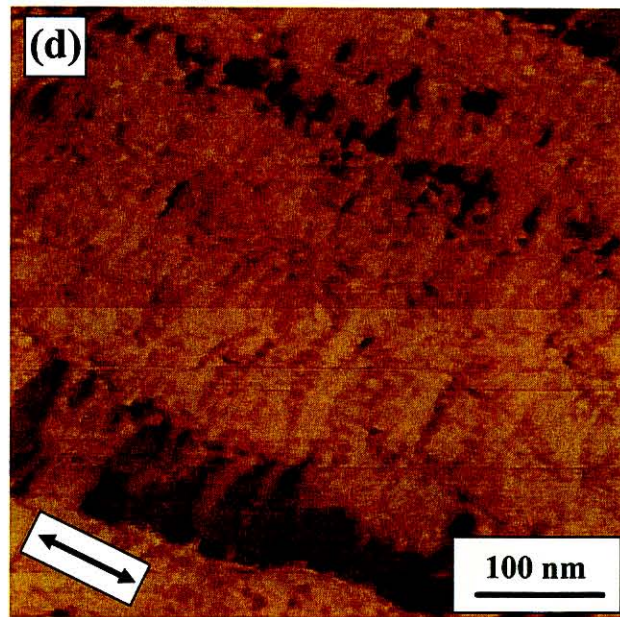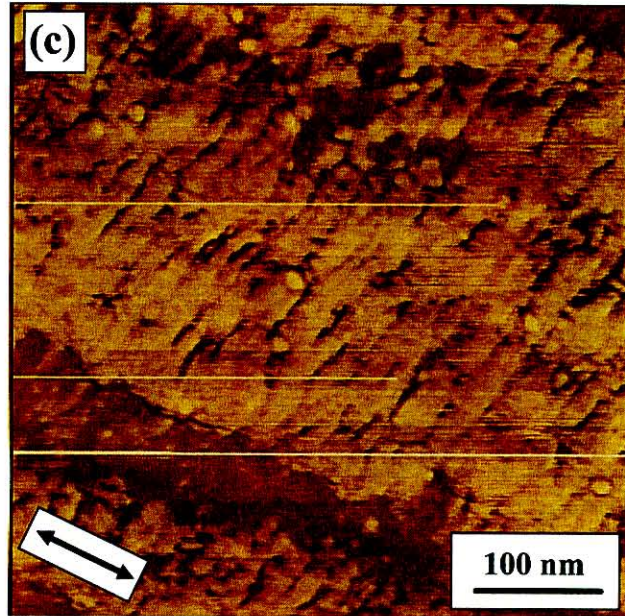
Figure 2(Continued): AFM phase images of Blend-I at 40 °C (c) and at 60 °C (d). The arrow indicates FD.
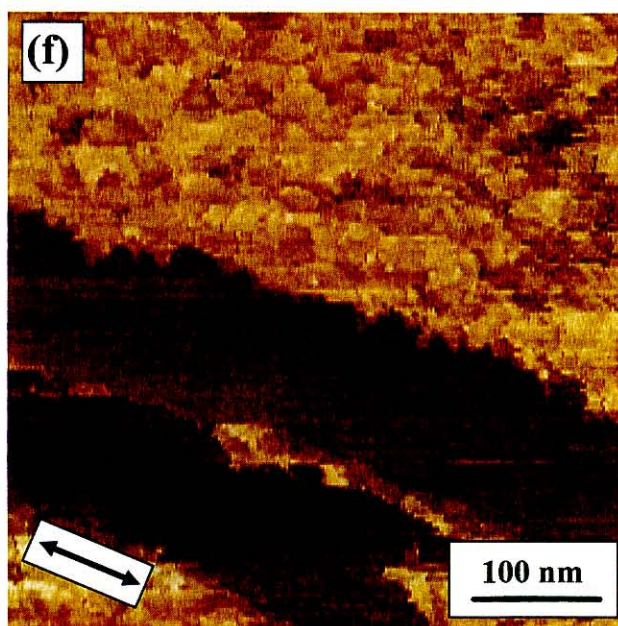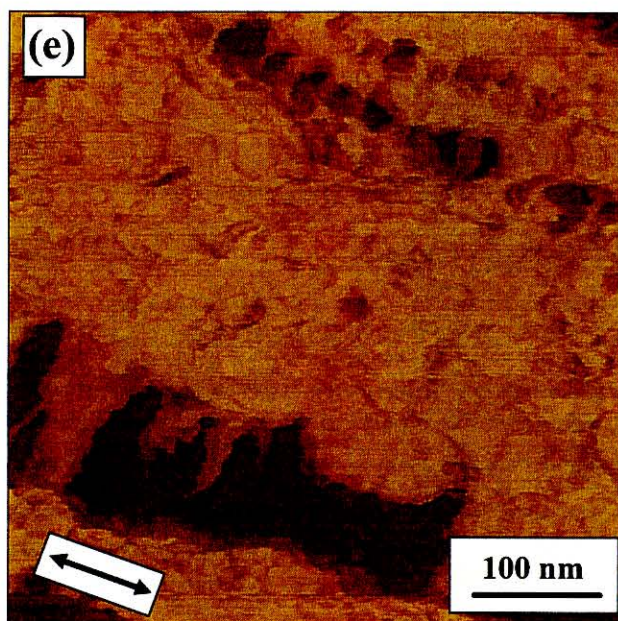
Figure 2(Continued): AFM phase images of Blend-I at 80 °C (e) and at 100 °C (f). The arrow indicates FD.

143
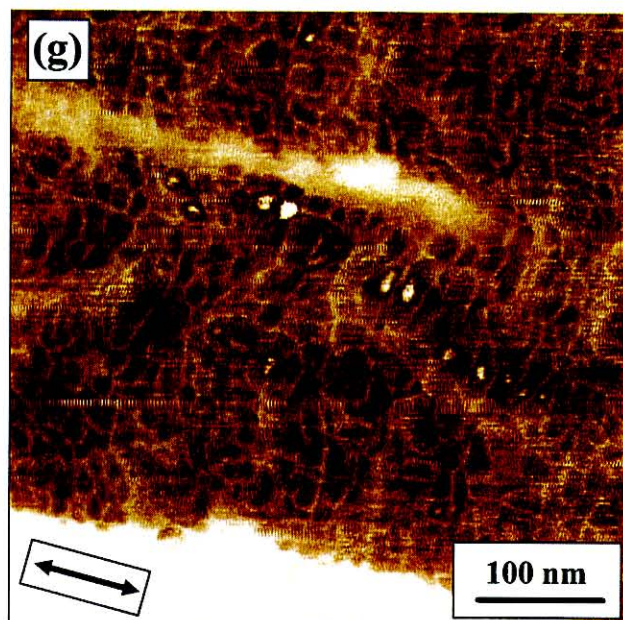
Figure 2(Continued): AFM phase images of Blend-I
at room temperature rapidly cooled from 100 ºC.
The arrow indicates the FD.

In contrast to the injection, quite different results are obtained in the
compression-molded blend, the Blend-P as shown in Figure 3.

At room temperature, the EOR phases (dark regions) are observed to be spherical
in shape at low magnification image (Fig. 3(a)). The stripe pattern originating form the
iPP lamellae are observed in analogy with the Blend-I but it is randomly oriented at
high magnification image (Fig. 3(b)).

On gradually increasing temperatures up to 60 °C (Figs. 3(c) and (d)), little or no
changes in the iPP-rich region are found. On further increase in temperature at 80 and

144

100 °C (Fig. 3(e)-(f)), we can observe the increase in the dark regions in the iPP phase, i.e., the iPP amorphous regions. This is reasonable result, considering that the thermal expansion in the amorphous region is much larger than that in the PP crystalline region [17].
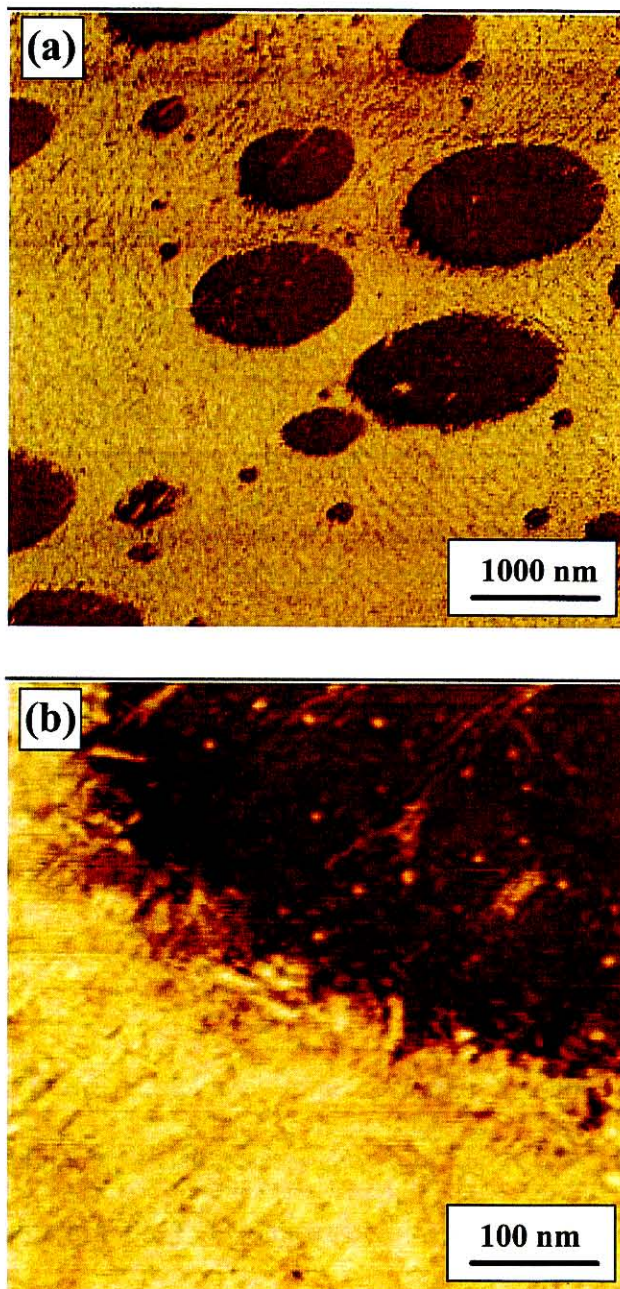
Figure 3: AFM phase images of Blend-P at room temperature at low magnification (a) and at high magnification (b).
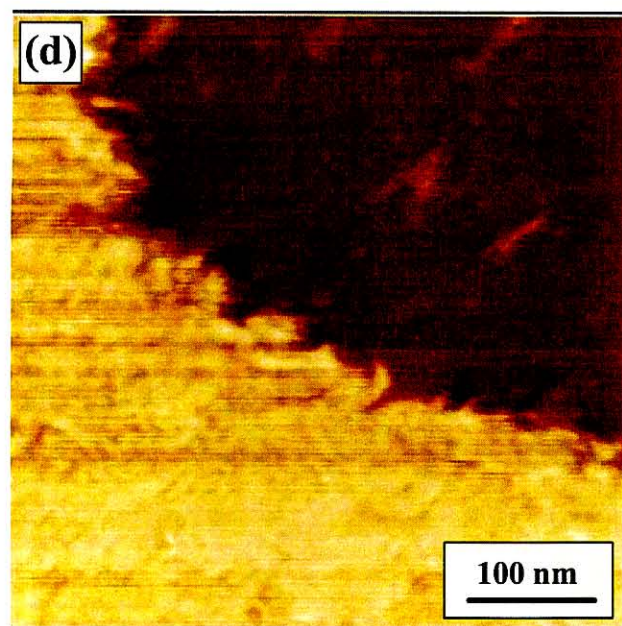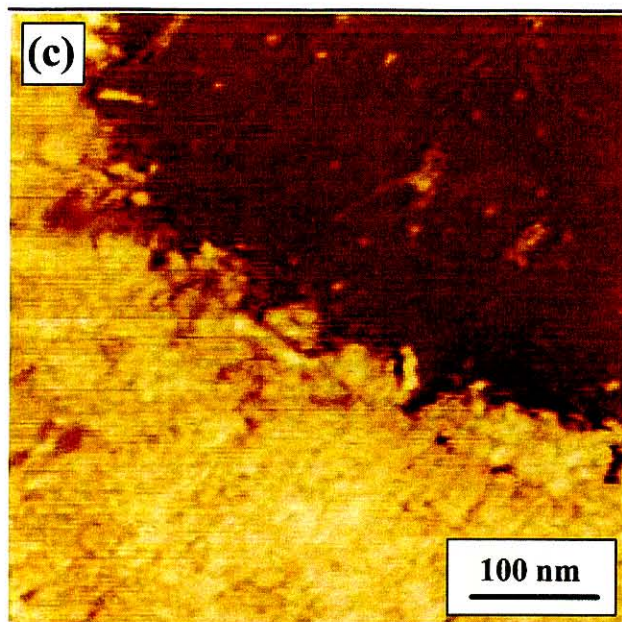
Figure 3(Continued): AFM phase images of
Blend-P at 40 °C (c) and at 60 °C (d).
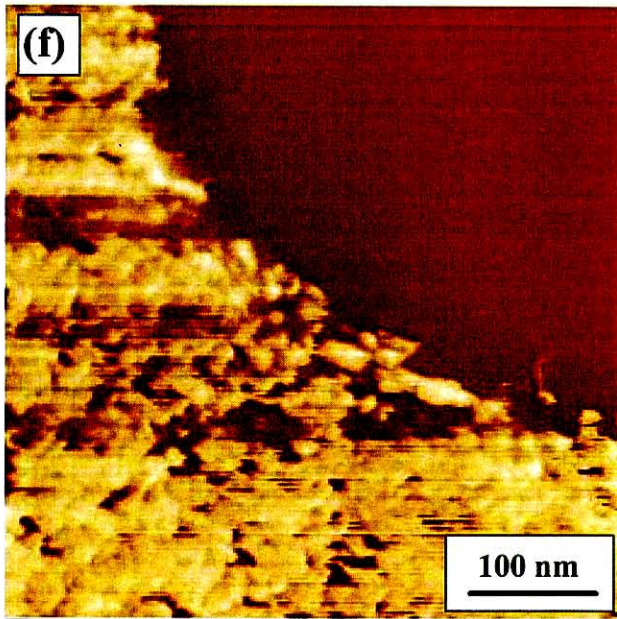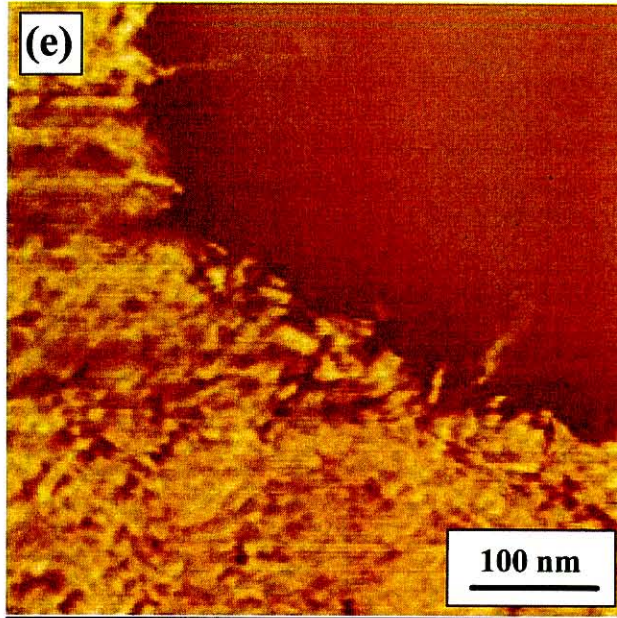
Figure 3(Continued): AFM phase images of
Blend-P at 80 °C (e) and at 100 °C (f).
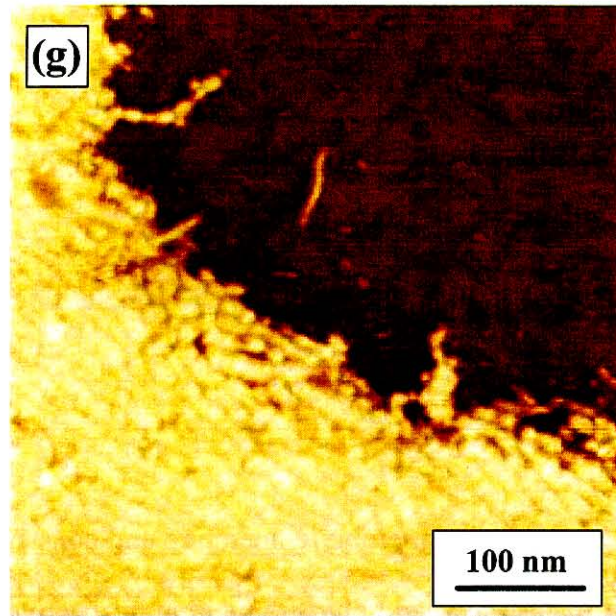
Figure 3(Continued): AFM phase images of
Blend-P at room temperature rapidly cooled
from 100 °C.

4. Discussion

In this part, we will discuss influencing factors giving rise to the unusual morphological changes observed in the iPP matrix for the Blend-I. Firstly, we will investigate the change in the lamella thickness of the iPP crystalline region using DSC and SAXS.

4-1. Crystallinity change at every temperature stage:

Figures 4(a) and (b) show the crystallinity (X_c) and the T_m for each Blend-I and −P by the change in the initial holding temperature, respectively. The each holding

temperature corresponds to the one employed for the above AFM observation.

Fig. 4(a) reveals that no major change in the crystallinity between the two blends is observed throughout any initial holding temperatures. On the other hand, Fig. 4(b) reveals that the T_m values of the Blend-I decrease a bit with increasing the initial holding temperatures, whereas those of the Blend-P are found to be nearly constant under the variation of the initial holding temperatures.

The T_m of highly crystalline polymers and the lamella thickness (l_c) had a linear correlation given by equation (2) [18],

$$T_m = T_m^0 - \frac{C}{l_c} \qquad (2)$$

where T_m^0 and C are equilibrium melting temperature and constant related with surface free energy and heat of fusion when polymers melting, respectively. The T_m^0 and C for the iPP were estimated as 186.1 °C and 240 by Yamada et al. [19]. Hence, eq. (2) is rewritten as equation (3).

$$T_m = 186.1 - \frac{240}{l_c} \qquad (3)$$

Inserting the T_m values obtained into eq. (3) yields the lamella thickness. The correlation of the lamella thickness (l_c) at each temperature for each blend as a function of the initial holding temperature is shown in Figure 5. The l_c values for the Blend-I decrease with increasing the temperature as analogy with the T_m trend. Thus, we can conclude that spreading the crystalline area observed in the AFM images for the Blend-I at elevated temperatures would not result from the increase in the lamella thickness.
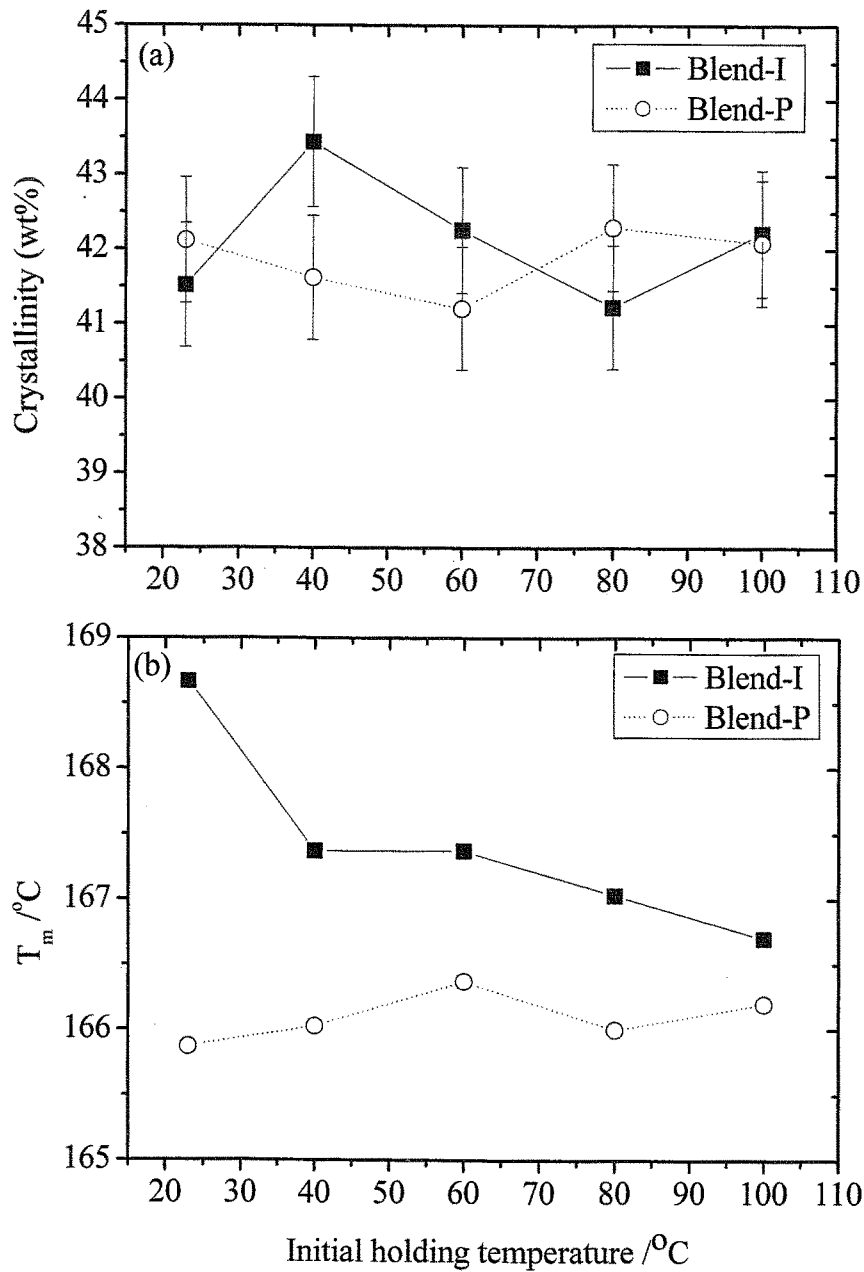
Figure 4: Change in the crystallinity (a) and the melting temperature (b) of the iPP in each blend by changing the initial holding temperature.
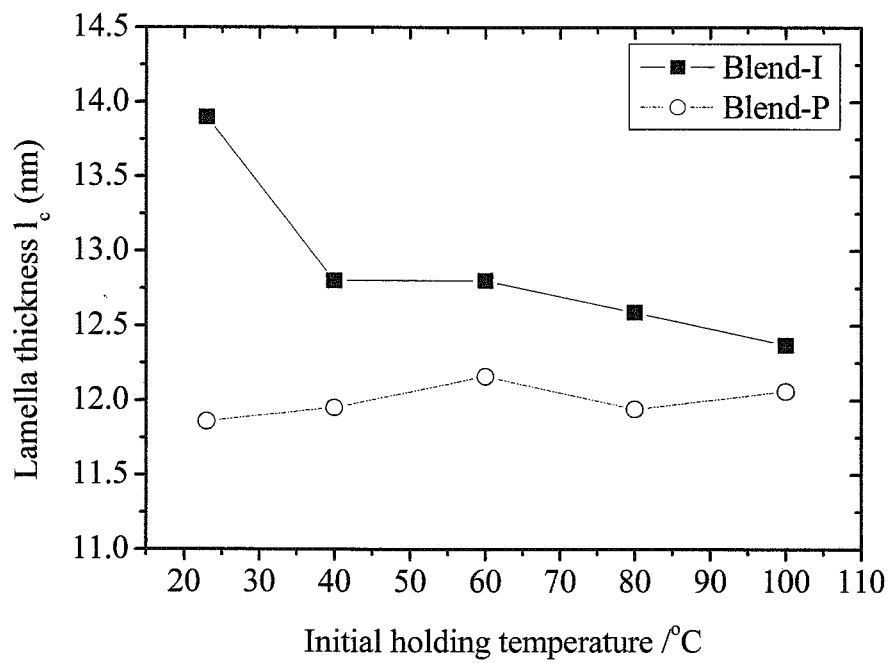
Figure 5: Change in the lamella thickness of each blend by changing the initial holding temperature.

4-2. Variation of PP long period with temperature change:

Figures 6(a) and (b) show the SAXS data of the Blend-I and -P with temperature change, respectively. These figures display $I(q)q^2$ versus q, where $I(q)$ is the intensity function and $q=(4\pi/\lambda)\sin\theta$, λ and θ being the wavelength of the X-ray and the scattering angle.

In both cases, the peak position shifts slightly to left, thus smaller q value with increasing temperature, indicating that the long period (L), i.e., the most probable next neighbor distance of the lamellae increases with temperature changes.

Using the long period (L) expressed as $L=2\pi q^{-1}$ and the lamella thickness (l_c) in the previous section, we can obtain the amorphous thickness (l_{am}) of each blend from $L-l_c$ thus $2\pi q^{-1}-l_c$ with temperature change. The results together with the l_c change are shown in Figure 7. In the case of Blend-I, the l_c decreases but the l_{am} increases with increasing temperature. This is reverse trend in the AFM observation, in which the amorphous area gradually shrinks but the crystalline area expands.

On the other hand, for the Blend-P, the l_c show almost constant and the l_{am} slightly increases with temperature change. This is in good agreement with the AFM images for Blend-P, in which the amorphous area seems to gradually spread when increasing temperature as presented in Fig. 3.
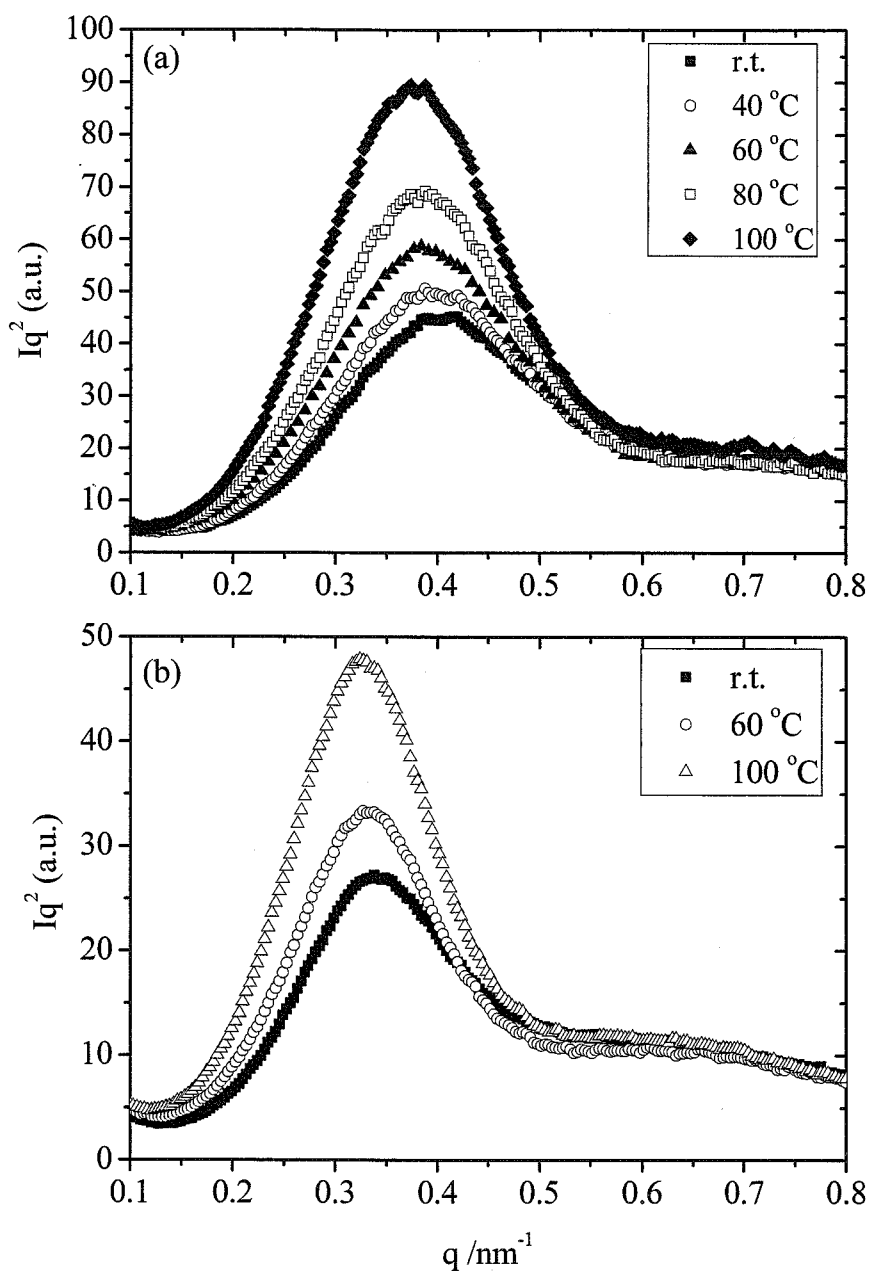
Figure 6: SAXS profiles of (a) Blend-I and (b) Blend-P.
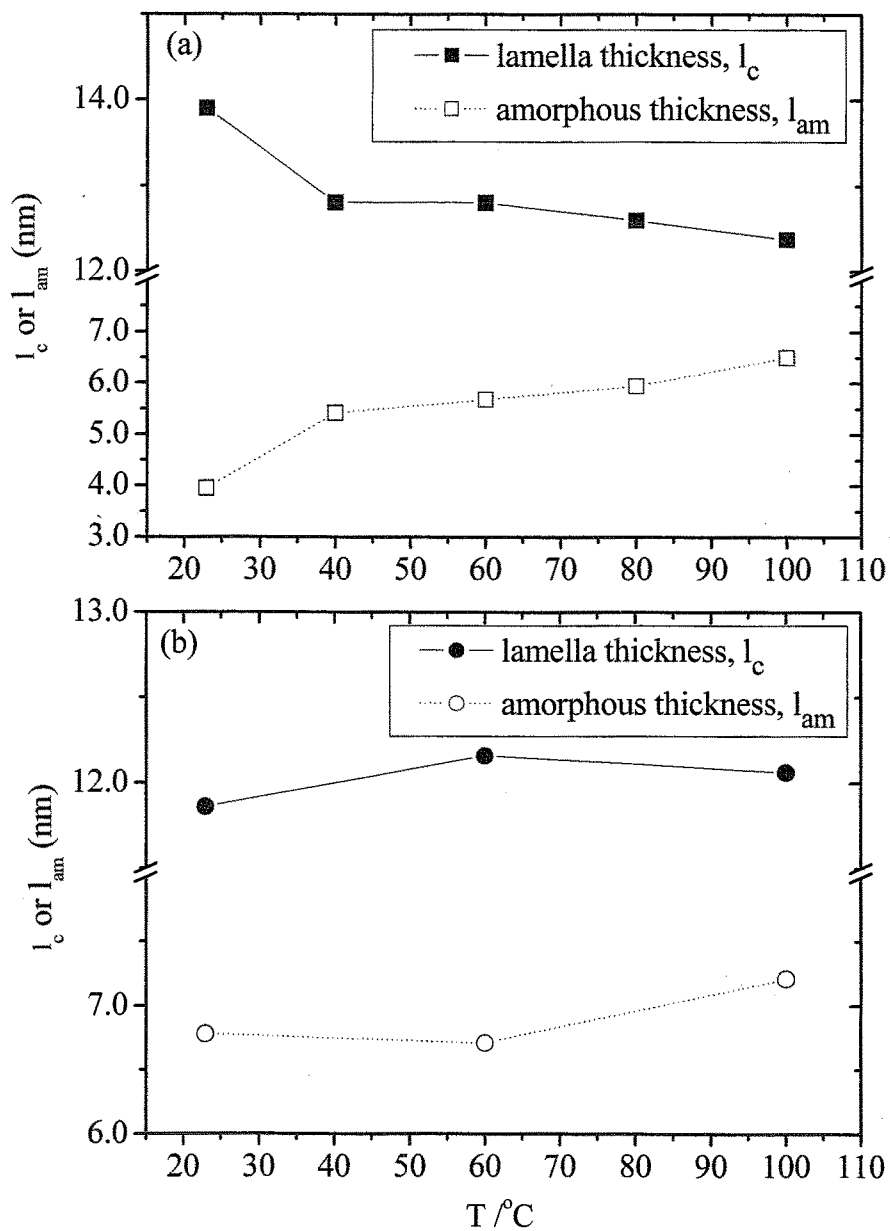
Figure 7: Temperature dependence of the lamella and amorphous thickness for (a) Blend-I and (b) Blend-P.

Tanabe *et al.* [20] reported using SAXS analysis of linear low density polyethylene (LLDPE) the simultaneous decrease in l_c and increase in l_{am} at higher temperatures below melting temperature. It was resulted from a surface melting of the lamellae. Albrecht and Storbl [21] also reported the similar phenomenon and reached the same conclusion.

In the present system, the crystal regions in the Blend-I fabricated by injection-molding would include lots of imperfect crystals thus thin lamellae which would be easily formed as a result of rapidly cooling under high pressure, compared with the Blend-P by compression-molding. Due to the presence of such imperfect crystal with low melting temperature residing inside the lamellae or near the interface between the crystal and the amorphous regions, the surface melting would occur in the Blend-I more easily than in the Blend-P.

In the following section, we discuss the mobility of the crystal regions based on the apparent activation energy, ΔH^* by DMTA.

4-3. Apparent activation energy of the PP amorphous and crystal regions:

The α_a peak belonging to the relaxation of the iPP amorphous chains in the blend was clearly observed at around 270-280 K, the peak of which was employed for the determination of ΔH^* of the iPP amorphous chains. The α_c relaxation corresponding to the iPP crystalline chains was, however, observed as an inflection point not a peak. Hence, we adopted the point of the intersection obtained by extrapolating the two tangent lines of the curve of DMTA as the α_c peak of the crystalline region. An example is shown in Figure 8.
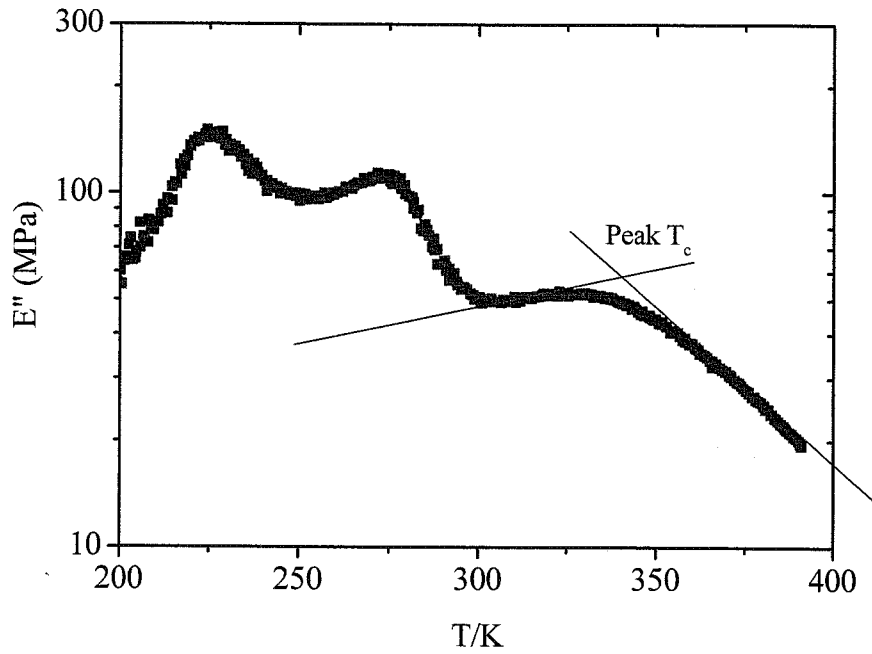
Figure 8: Determination of the dispersion peak of the
crystal region.

The reciprocal peak temperatures for both the crystalline and amorphous chains at

each frequency (f) are plotted against log f, which is shown in Figure 9(a) and (b).

157
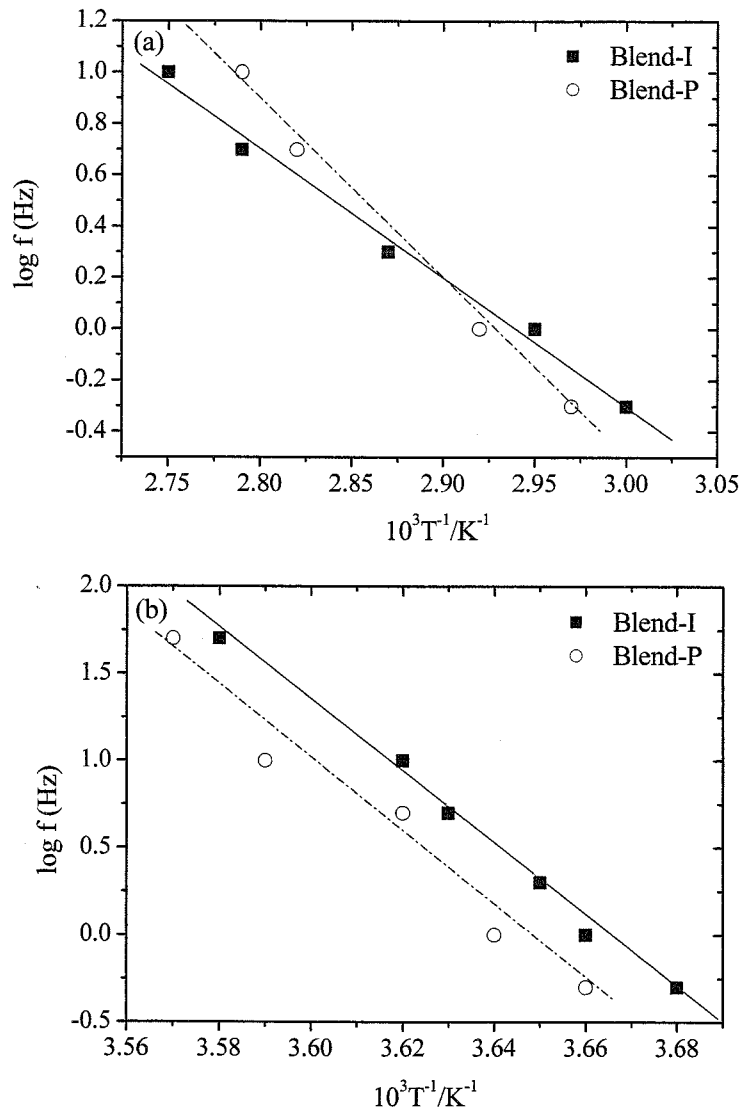
Figure 9: log f as a function of T-1 for Blend-I and Blend-P;
(b) α_c to the iPP crystal chains and (b) α_a relaxation
belonging to the iPP amorphous chains.

Inserting the slope of these lines into eq. (1) yields the apparent activation energy

(ΔH^*) of each blend. The value of the ΔH^* for the α_c is 95 kJ/mol for the Blend-I and

136 kJ/mol for the Blend-P, respectively, thus being indicative of higher mobility of the

crystal regions for the injection-molded blend (Blend-I) compared with that of the compression one (Blend-P). On the other hand, the value of the ΔH^* for the α_a exhibits 396 kJ/mol for the Blend-I and 411 kJ/mol for the Blend-P (no difference), indicating no differences in the mobility in the iPP amorphous chains between the two blends.

From the results obtained above, we will consider the AFM image difference between the two blends. In terms of the phase images on the tapping mode, the image contrast is discriminated as the difference in the adhesive force between tip and sample. In the case of the Blend-I, the surface melting in the crystal regions occurs more easily compared with the Blend-P, thus resulting in making the surface of crystal regions so adhesive as the amorphous regions and causing disappearance of the phase image contrast between the two regions at elevated temperatures. That would be one of the plausible reasons why the amorphous regions of the Blend-I seem to shrink and disappear at higher temperatures.

4-4. Correlation of thermal expansion behavior with morphological change:

In this section, we will discuss the correlation of the morphological change of the order of nanometer with a bulk thermal property, the CLTE behavior.

Figure 10 shows the CLTE-temperature profile for the Blend-I (α_{FD}) and Blend-P (α_{SD}).

As can be seen in Fig.10, the Blend-I has quite different CLTE behavior from that of the Blend-P in spite of each blend consisting of the same formulation. The α_{FD} shows a clear inflection point at around 40 °C, and above this temperature, the CLTE decrease. On the other hand, the α_{SD} shows a relatively monotonic increase via small inflection point at around 60-70 °C.

The inflection point observed at 40 °C corresponds to the temperature where the morphological change begins to emerge in the iPP matrix for the Blend-I. This CLTE behavior might have some correlation with the surface melting of the crystal region. It will be reported in the future.
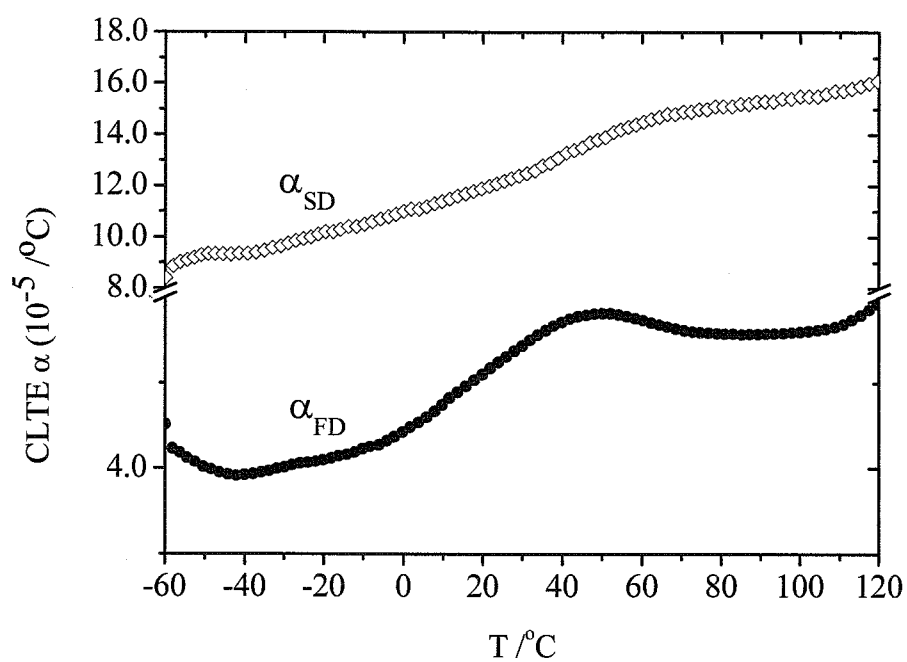
Figure 10: Differences in the CLTE behaviors between Blend-I and Blend-P.

5. Conclusions

The real-time morphology observation of iPP/EOR blend systems at elevated temperatures was conducted. We compared the phase images of the injection-molded specimen (Blend-I) with those of the compression-molded one (Blend-P) at various temperatures. In the case of the Blend-I, the morphology in the iPP matrix drastically changed at elevated temperatures; an increase in the crystalline area while decrease in the amorphous area. For the Blend-P, the amorphous area in the iPP matrix began to expand at higher temperatures. The morphological behavior in the Blend-I was quite abnormal when taking much higher thermal expansion in the iPP amorphous region into consideration. The SAXS and DMTA studies revealed that the surface melting of imperfect crystallites residing at the interface between the lamellae and the amorphous region or inside the lamellae would take place in the Blend-I more easily than in the Blend-P. Such surface melting in the crystalline region would cause fading the image contrast as a result of reducing the difference in the adhesive force between the crystalline and amorphous region.

6. References

[1] Trent J.S., Scheinbeim J.I. and Couchman P.R.; *Macromolecules*, 1983, **16**, 598

[2] Kakugo M. and Sadatoshi H.; *J. Polym. Sci. : Part C, Polym. Lett.*, 1986, **24**, 171

[3] Magonov S.N., Elings V. and Papkov V.S.; *Polymer*, 1997, **38**, 227

[4] Pearce R. and Vansco J.; *Polymer*, 1998, **39**, 1237

[5] Sikes H.D. and Schwartz D.K.; *Science*, 1997, **278**, 1604

[6] Magonov S.N. and Godovsky Y.K.; *Am.Lab.*, 1998, **30**, 15

[7] Godovsky Y.K. and Magonov S.N.; *Langmuir*, 2000, **16**, 3549

[8] Jiang Y., Jin X.G., Han C.C. and Li L.; *Langmuir*, 2003, **19**, 8010

[9] Ivanov D.A., Amalou Z. and Magonov S.N.; *Macromolecules*, 2001, **34**, 8944

[10] Alexander E.J., *"X-ray Diffraction Methods in Polymer Science"*,
Wiley-Interscience, New York, 1969

[11] Takayanagi M., Imada K. and Kajiyama T.; *J. Polym. Sci. : Part C*, 1960, **15**, 263

[12] Yamaguchi M., Miyata H. and Nitta K-h.; *J. Appl. Polym. Sci.*, 1996, **62**, 87

[13] Muller F.H. and Huff K.; *Kolloid Z.*, 1959, **166**, 44

[14] Min K. and White J.L.; *Polym. Eng. Sci.*, 1984, **24**, 1327

[15] Ling Z., Rui H., Linagbin L. and Gang W.; *J. Appl. Polym. Sci.*, 2003, **83**, 1870

[16] Kim B.K. and Do I.H.; *J. Appl. Polym. Sci.*, 1996, **60**, 2207

[17] Zoller P. and Walsh P.J.; *"Standard Pressure-volume-temperature data for Polymers"*, Technomic Publishing Co., Lancaster PA. USA, 1995

[18] Wunderlich B.; *"Macromolecular Physics"* Vol 3, Academic Press, New York, 1980

[19] Yamada K.; *Ph.D. Thesis Hiroshima Univ.*, 2001

[20] Tanabe K., Strobl G.R. and Fischer E.W.; *Polymer*, 1986, **27**, 1147

[21] Albrecht T. and Strobl G.; *Macromolecules*, 1995, **28**, 5827

7. Acknowledgement

Chapter 7

Nano-mechanical Properties of Finely Dispersed EOR Domain in iPP/EOR blend using AFM and their Correlation with CLTE Behavior

1. Introduction

In Chap. 2, the author investigated the difference in the CLTE behaviors between the injection- and compression-molded iPP/EOR blend, in which large CLTE anisotropy was found in the injection whereas the CLTE in the compression was almost isotropic. We pointed out that such difference, in particular, the anisotropic CLTE behavior in the injection specimen would be caused by synergy effects of the following factors; (1) iPP crystal orientation (Chaps. 2 and 4), (2) retraction from the EOR having lamella-like sheet array stacked normal to normal-to-flow direction (ND) (Chap. 4) and (3) allocation of iPP amorphous region (Chap. 5).

As indicated above, the CLTE anisotropy in the injection-molded specimen is deeply connected with both iPP and EOR parts not just with either one. We conducted the real-time morphological observation at higher temperatures using AFM in Chap. 6, thus providing direct information on the morphological change in each component with temperature variation. As a result, in the case of the injection-molded iPP/EOR blend, the surface melting from the iPP lamellae or the interface between the crystal and amorphous region would occur even below the T_m of the iPP. The surface melting might be also correlated with the anisotropic CLTE behavior because the surface melting

164

began to occur from 40 °C which was in good agreement with the apparent inflection point found in the CLTE-temperature curve. However, we couldn't acquire any information of morphological and/or mechanical changes in the EOR domains accompanying by temperature variation.

The AFM is a powerful tool not only for the morphological observation of polymer blends under various environments [1-4] but also for evaluation of physical property of the surfaces of the polymers [5-12]. Compared with other tools, AFM can probe local surface mechanical properties with high resolution, down to several tens of nanometers, and with fine control of applied force, down to several nanonewtons [13-15]. These two characteristics provide the AFM advantages for studying the mechanical properties of materials because most of these exhibit nanoscale heterogeneous modulus distribution.

In this Chapter, we focused on quantifying the elastic modulus of finely dispersed EOR domains in the iPP/EOR blend using the AFM; we investigated the difference in the elastic modulus by the difference in the shape or array of the EOR domains, and by the difference in the thermal history for the injection-molded iPP/EOR specimen. Lastly, we discussed the relationship of the elastic modulus of the EOR domains with the CLTE behaviors.

2. Theory

In general, the elasticity of the polymeric surfaces using AFM has been measured by the indentation method [16-18], in which force-distance curves are monitored when the tip is loaded into the sample surface. In this method, elastic properties can be obtained by fitting the recorded force curve under the loading process into the Hertz

165

model [7,10,12,19-21]. In addition, the Hertz model is based on the assumption of no adhesive interaction between the tip and sample [22]. Hence, this technique shows the limitations when applied to soft or adhesive materials such as polymeric surfaces including rubbers. Because of difficulty of accurate determination of the tip-sample contact point, a small uncertainty will cause a significant experimental error in calculating sample elasticity. Active indentation in soft and thin samples also will have interference from the substrate modulus, which complicates the study of sample properties [18]. In addition, a large indentation with a sharp tip in the sample may break its stress-strain linearity, or even make it fracture.

In the case of the present system including adhesive rubber domains, the Hertz model using the force-curve during the loading process would be no longer valid. We acquired the elastic modulus based on the unloading force curve not the loading one by being applied to the Johnson-Kendall-Roberts model (hereafter called the JKR model) [23] which considers the adhesion effect.

As two elastic spheres contact, the adhesion and the external load cause an elastic deformation and a contact area forms between the two elastic bodies. According to the JKR model, the contact area a is given by

$$a^3 = \frac{R}{K}\left[P + 3\pi Rw + \sqrt{6\pi RPw + (3\pi Rw)^2}\right] \qquad (1)$$

$$a_0^{\,3} = 6w\pi R^2 \Big/ K \qquad (2)$$

$$\delta = \frac{a^2}{R}\left[1 - \frac{2}{3}\left(\frac{a_0}{a}\right)^{3/2}\right] \qquad (3)$$

$$\frac{1}{K} = \frac{3}{4}\left[\frac{1-v_1^{\,2}}{E_1} + \frac{1-v_2^{\,2}}{E_2}\right] \qquad (4)$$

166

where P, w, a_0, δ and R are the external load, the work of adhesion, the contact radius under zero load and sample deformation and the radius of the tip, respectively. E and ν are Young's modulus and Poisson ratio. The subscript 1 and 2 means the sample and the tip, respectively. In the present system, $E_2 \gg E_1$ so that $1/K$ is reduced to

$$\frac{1}{K} = \frac{3}{4}\left(\frac{1-\nu_1^2}{E_1}\right) \qquad (5)$$

In reality, we can require the relation connecting the load P, the sample deformation δ and the elastic modulus E. For this purpose, we use "the two point methods" [8], which is the method that any two points from the unloading force curve. For simplifying the calculation, "zero point" and "maximum adhesion point" are chosen as the two points. Here, the zero point is defined as the point where the adhesive interaction and the stored elastic force are balanced, and thus a zero external force is taken on the tip. The maximum adhesion point represents the point where the tip has a maximum external force due to the adhesion between the tip and sample.

A typical force-curve is shown in Figure 1 where the zero and the maximum point are presented in the unloading force curve.
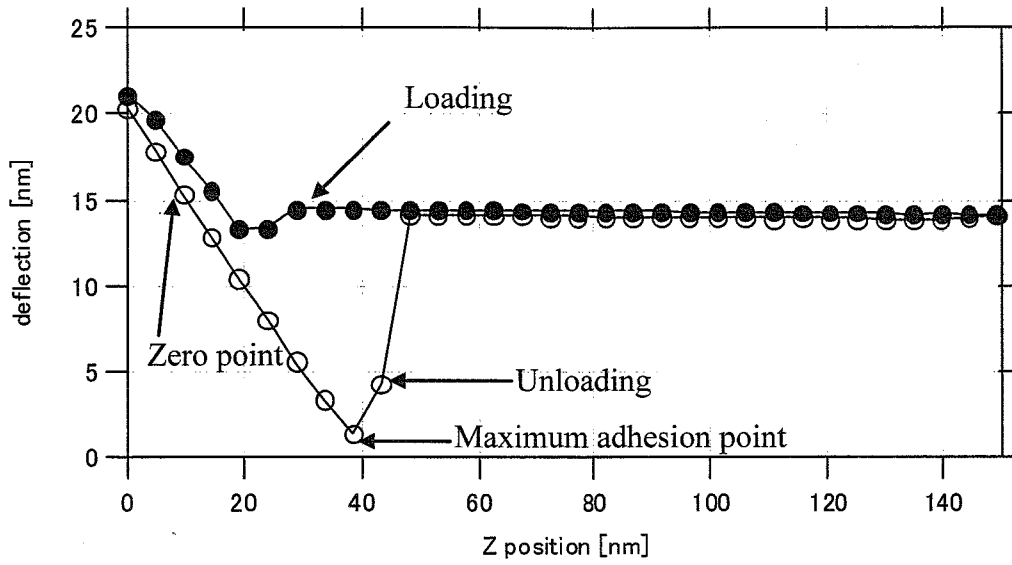
Figure 1: A typical AFM force curve for a soft or adhesive material. Closed circles mean the curve profile under loading process, and open ones are the one under unloading process. The zero point is where the tip has zero external force, and the maximum adhesion point is where the tip has a maximum external force.

When P_1 is defined as the load at the maximum adhesion point, the P_1 is negative load and given by

$$P_1 = -\frac{3}{2}\pi wR \qquad (6)$$

Hence, the contact area a_1 at the maximum adhesion point is given by

$$a_1 = \frac{a_0}{4^{1/3}} . \qquad (7)$$

Combining eq. (2) and (7) with eq. (3), we can obtain the sample deformation at the zero point (δ_0) and the maximum adhesion point (δ_1);

$$\delta_0 = \frac{1}{3}\left(\frac{16P_1^2}{K^2 R}\right)^{1/3} \qquad (8)$$

$$\delta_0 = -\frac{1}{3}\left(\frac{P_1^2}{K^2 R}\right)^{1/3} \qquad (9)$$

Combining eqs. (8), (9) and (5), we can obtain the relation connecting the elastic modulus E, the sample deformation δ and the maximum load P_1.

$$E = \frac{3(1-\nu^2)}{4}\left(\frac{1+16^{1/3}}{3}\right)^{2/3}\frac{P_1}{\sqrt{R(\delta_0 - \delta_1)^3}} \qquad (10)$$

We can obtain the elastic modulus E by inserting P_1, δ_0 and δ_1 (known from the unloading fore curve) into eq. (10). The value 0.5 as the Poisson's ratio ν was employed in this study.

3. Experimental

3-1. Raw materials and sample preparation:

Isotactic polypropylene (iPP) used in this study was supplied by SunAllomer Ltd., had 98.5 % of isotactic index [mmmm] determined by ^{13}C-NMR. Poly(ethylene-co-octene) rubber (EOR) was commercially available from Dow Chemical, had 24 wt% of octene content. The other structural information for each material was listed in Table I.

Table I Sample information of raw materials

Designation	Types of Polymer	zero-shear viscosity (Pa.s)	Flexure modulus (nominal) (MPa)	Tm (°C)	Crystallinity (%)
iPP	Isotactic PP	5,600	1,650	165.5	47.2
EOR	Poly(ethylene-co -octene)	455	20	50-60	n.d.[2]

1) measured at 230°C.
2) Negligibly small

The blend sample of iPP/EOR (70/30 (v/v)) having 0.085 of a viscosity ratio

η_i^* / η_m^* was prepared by being melt-blended with a co-rotating twin screw extruder

(TEX30α; JSW). The detailed procedures were described in Chap. 2. The specimen

fabrication with the resulting blend was carried out by two different methods, the

injection- and the compression-molding to control the morphology of the elastomer

inclusion. The detailed procedures were described in Chap. 2 for the injection-molding

and Chap. 6 for the compression-molding. The definition of the directions and cross

sections of the resulting specimens were illustrated in Figure 1.
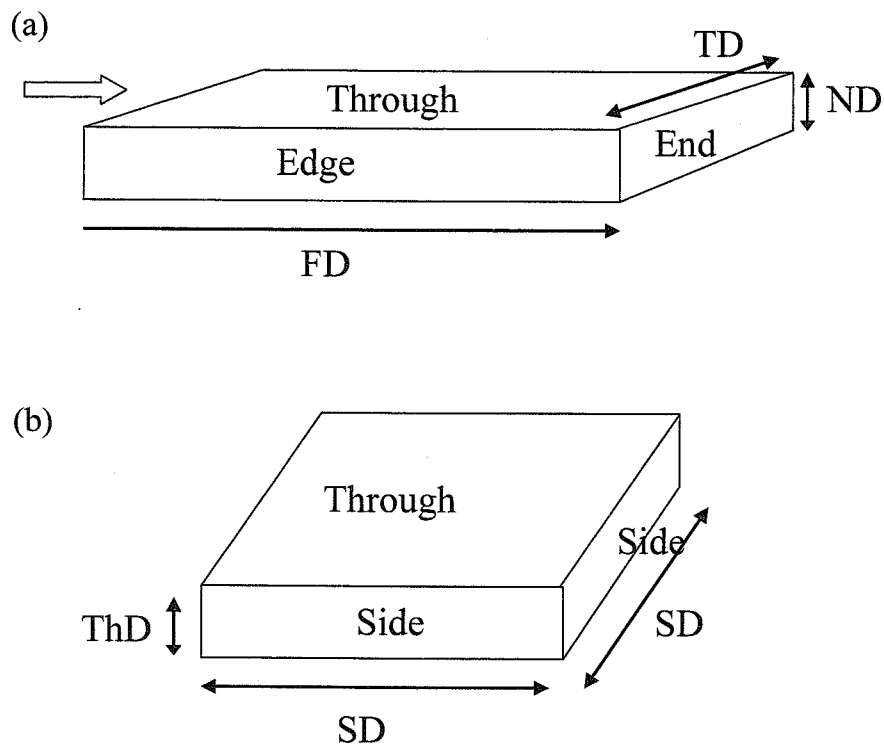
Figure 1 : Nomenclature of direction and cross section.
(a) injection-molded specimen; For directions, FD (parallel to flow direction) , TD (transverse to flow direction) and ND (normal to flow direction). For cross sections, Edge- (parallel to FD), End- (parallel to TD) and Through view (parallel to ND).

(b) compression-molded specimen. For directions, SD (parallel to width or length direction) and ThD (parallel to thickness direction). For cross sections, Side view (parallel to SD) and Through view (parallel to ThD)

3-2. AFM measurements:

The sample for the AFM measurement was punched out from the central part of the specimen fabricated above followed by annealed at a given temperature for 2 hours and then conditioned at 23 °C overnight. After that, the annealed sample was microtomed at cryo-temperature (-100 °C) to obtain the flat surface. The observed cross

section was the edge-view parallel to FD for the injection-molding and the side view for the compression-molding specimen.

For the AFM measurements, Nanoscope IV (Veeco) as apparatus and NP-2 (Veeco) as a cantilever were used. The cantilever used had 0.58 N/m (nominal) of the spring constant and 20 nm (nominal) of the tip radius. Force volume mode, which utilizes the collection of the force curves over selected surface areas, was employed for the mapping of the mechanical properties of the polymer blend surface. This mode enables the mapping of the mechanical properties with nanometer scale resolution while obtaining topographic images simultaneously. As a typical condition, we used 64×64 pixels per image and $1.0 \times 1.0 \ \mu m^2$ of a scan area. Fitting the force curves collected into eq. (10) using a soft ware package (IgorPro) gave the local elastic modulus.

3-3. Linear thermal expansion coefficient evaluation:

The CLTE evaluation was made according as the procedures in Chap. 2. The measured direction was FD for the injection sample and SD for the compression one.

4. Results and discussion

## 4-1. Difference in elastic modulus in the EOR domains by their shapes:

We evaluate the difference in the elastic modulus depending on the shapes in the EOR domains, fibrous- (injection) and spherical-shape (compression). The elastic modulus mapping images and their histograms of the modulus distribution for the injection- and compression-molded specimen are shown in Figures 2 and 3, respectively. Both specimens for this experiment were annealed at 100 °C for 24 hours before use in order to eliminate their thermal history, followed by being cryo-microtomed for obtaining a flat surface.

Relatively lower modulus regions, which are considered to correspond to the EOR domains, are observed as fibrous for the injection (Fig. 2(a)) and spherical (Fig. 3(a)) for the compression. It is confirmed by the TEM images of corresponding specimens from edge- and side-view as shown in Figures 4(a) and (b); the EOR domains as dark regions are found to be fibrous in the injection (Fig. 4(a)) along flow direction (FD) whereas to be spherical in the compression (Fig. 4(b)).

The higher modulus regions involving the areas exceeding the upper limit will correspond to the iPP matrix phase.
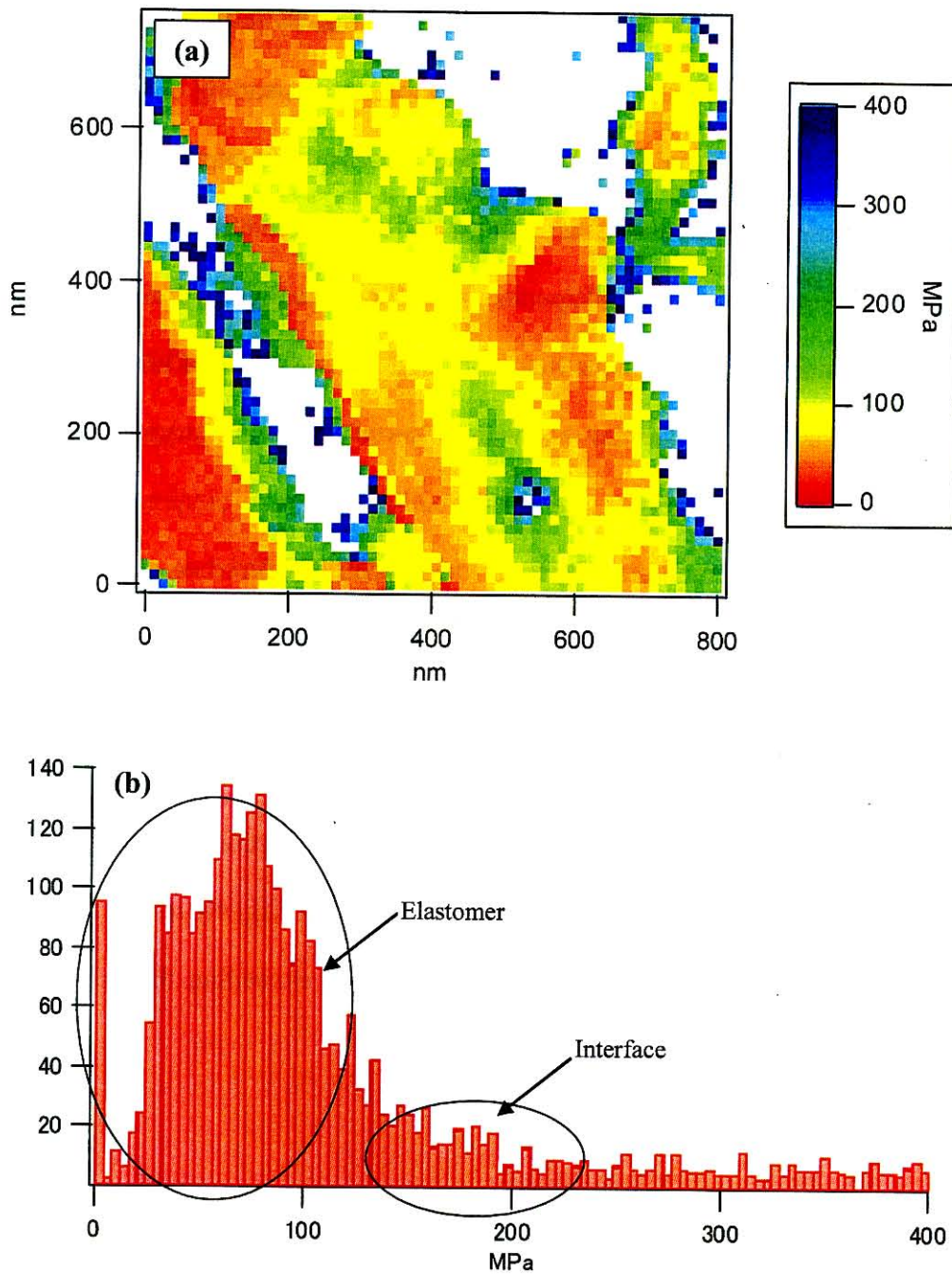
Figure 2: (a) Elastic modulus mapping image and (b) histogram of the elastic modulus for the injection-molded specimen after annealed at 100 ºC.
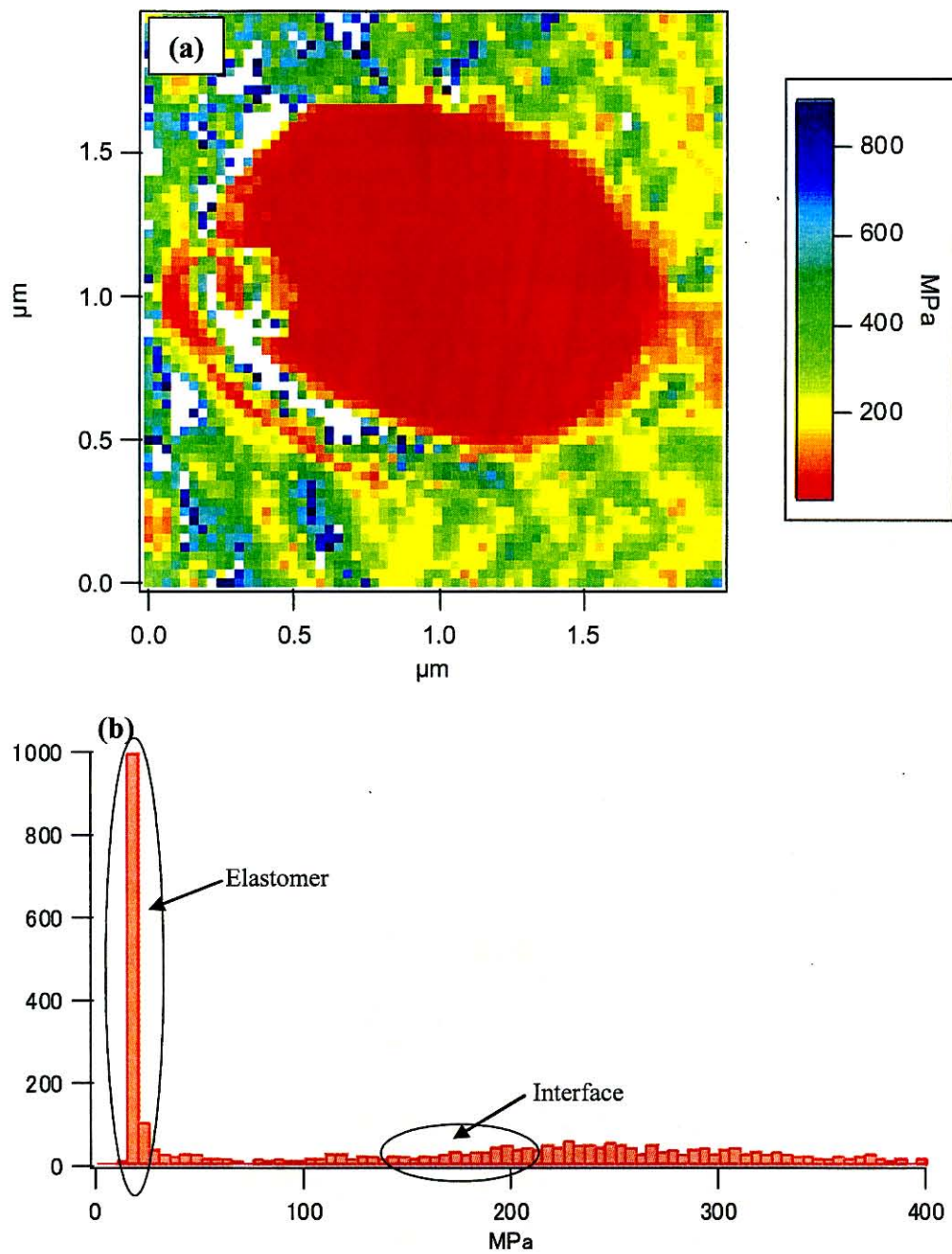
Figure 3: (a) Elastic modulus mapping image and (b) histogram of the elastic modulus for the compression-molded specimen after annealed at 100 °C.
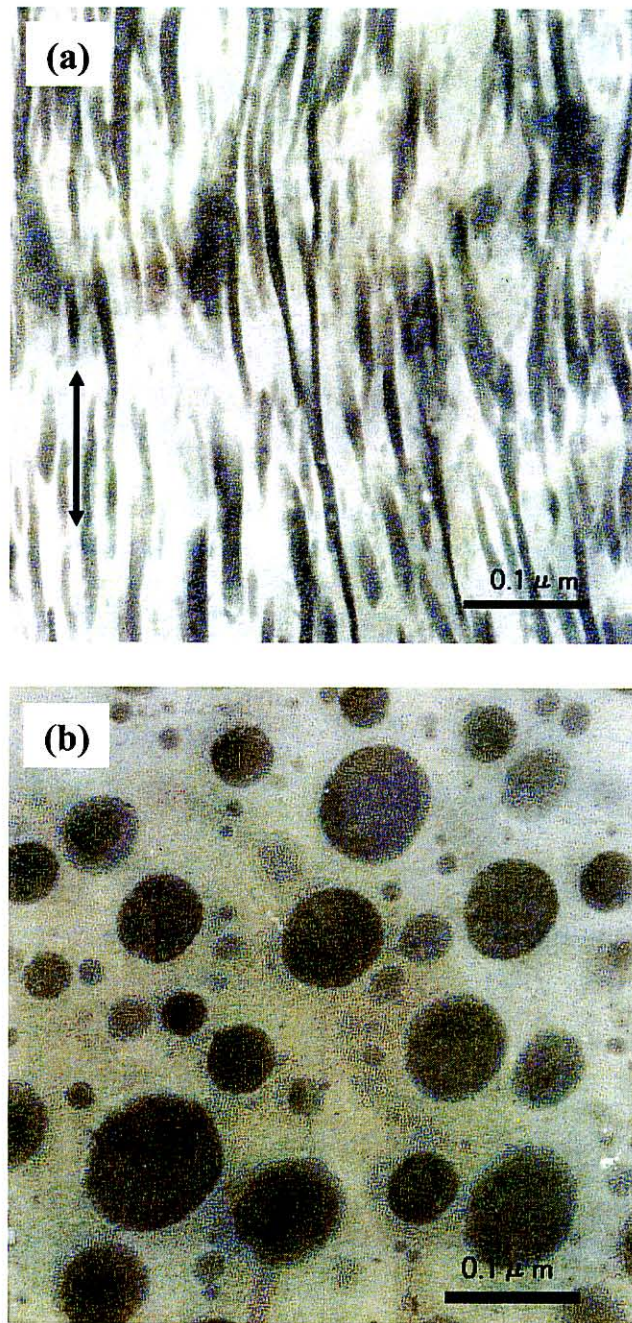
Figure 4: TEM micrographs (a) injection-molded specimen and (b) compression-molded specimen. Both are annealed at 100 °C before use.

In addition, at the interface between the EOR and iPP matrix, the elastic modulus in the injection blend exhibits broader distribution ranging from 150 to above 300 MPa, whereas the one in the compression blend is found to be homogeneously 150-200 MPa.

The difference in the elastic modulus inside the EOR domains will be discussed more clearly by using the corresponding histograms (Fig. 2(b) and 3(b)) rather than by the mapping images. In these histograms, the modulus below 300 MPa in Fig. 2(b) and 150 MPa in Fig. 3(b) will belong to that for the regions inside the EOR domains, taking the elastic modulus of the iPP matrix and the interface based on the above results into consideration. As for the fibrous EOR (injection), the elastic modulus widely distributes from 5 to 100 MPa and two peaks around 50 MPa and 70 MPa are clearly observed, thus being indicative of presence of more than two types of the EOR regions with different modulus. In contrast, for the spherical EOR (compression), almost all the elastic moduli in the EOR domain are found to be concentrated around 20 MPa without any distribution.

A tension f_x developing in a molecular chain is given by equation (11) according to the rubber-elastic theory on the assumption that a molecule would be one dimensional Gaussian chain [24]

$$fx = \frac{Rx}{NL^2} kT \qquad (11)$$

where Rx, N, L, k and T denote end-to-end distance, number of segment in a molecular, segment length, Boltzmann constant and temperature, respectively. By this, one can understand that a taut molecule having longer end-to-end distance is supposed to exhibit higher tension, compared with a random-coil molecule having shorter end-to-end distance. The highly elongated and taut molecules having higher tension (higher elastic modulus) would exist more in the injection blend than in the compression one.

These results indicate that the change in the fabrication method resulting in the variation of the shapes of the elastomer domains has a great influence on the physical property inside the rubber domain.

4-2. Change in elastic modulus in the EOR domains with annealing temperatures:

Figures 5-7 show the elastic modulus mapping images of the specimens with different thermal history with as-fabricated, annealed at 100 °C and annealed at 155 °C, respectively. (The Fig. 6, the same one as the Fig.2, is shown again.) The relatively lower modulus region represents the EOR-rich phase and the high modulus region mapped as pale blue ~ white in Figs. 5 and 6, and green ~ pale blue in Fig. 7 correspond to the iPP-rich phase.

In the as-fabricated specimen shown in Fig. 5, the elastic modulus belonging to the EOR-rich phase (Fig. 5(a)) widely distributes ranging from 20 to ~400 MPa. It is clearly confirmed by the histogram as shown in Fig. 5(b). The higher elastic modulus regions, i.e., higher stress regions, which are frequently found around the interface between the iPP and the EOR domain, show 20 times higher values than that of the nominal bulk modulus of the EOR (~20 MPa). In the highly deformed EOR resulting from the injection-molding under high shear followed by rapid cooling, a residual stress would remain inside the EOR phase because the stress relaxation inside the EOR would be arrested by faster solidification of the iPP matrix.

As annealed at 100 °C (Fig. 6), the elastic modulus in the EOR, as a whole, shifts to lower modulus region, thus leading to being narrower distribution accompanying with almost disappearance of the extremely high elastic modulus region (>200 MPa). It results from the stress relaxation of the EOR proceeding due to being annealed at 100

°C with higher temperature than the T_m of EOR (55 °C).

On further increase in the annealing temperature up to 155 °C (Fig. 7), which is above the onset melting temperature of the iPP (165 °C), the elastic modulus in the EOR region in red color turns out to be <20 MPa uniformly, which is lower than that of the EOR blend with annealed at 100 °C (Fig. 6), and closer to that of the EOR in the compression (Fig. 3). It means that all the residual stress inside the EOR would be removed as a result of the further procession of the stress relaxation.

The elastic modulus near the interface between the matrix and elastomer domain is about 40 MPa which is much lower than that in any other blends including the compression-molded blend.

Moreover, in the regions corresponding to the iPP matrix, the extremely high modulus region above the upper detectable limit almost disappears, thus resulting in relatively low value with <150 MPa. The reason for such a drastic decrease in the modulus in the iPP matrix is not clear at present. The blend consisting of iPP and ethylenic TPE exhibits the lower critical solution temperature (LCST) phase behavior in the melt [25-29]. Assuming that it would apply to the present iPP/EOR blend system, the liquid-liquid phase separation would proceed further by annealed near the T_m of the iPP, and the dissolved EOR would separate out from the iPP phase (iPP amorphous phase), thus leading to increase in the softer component (EOR) in the iPP matrix.

179
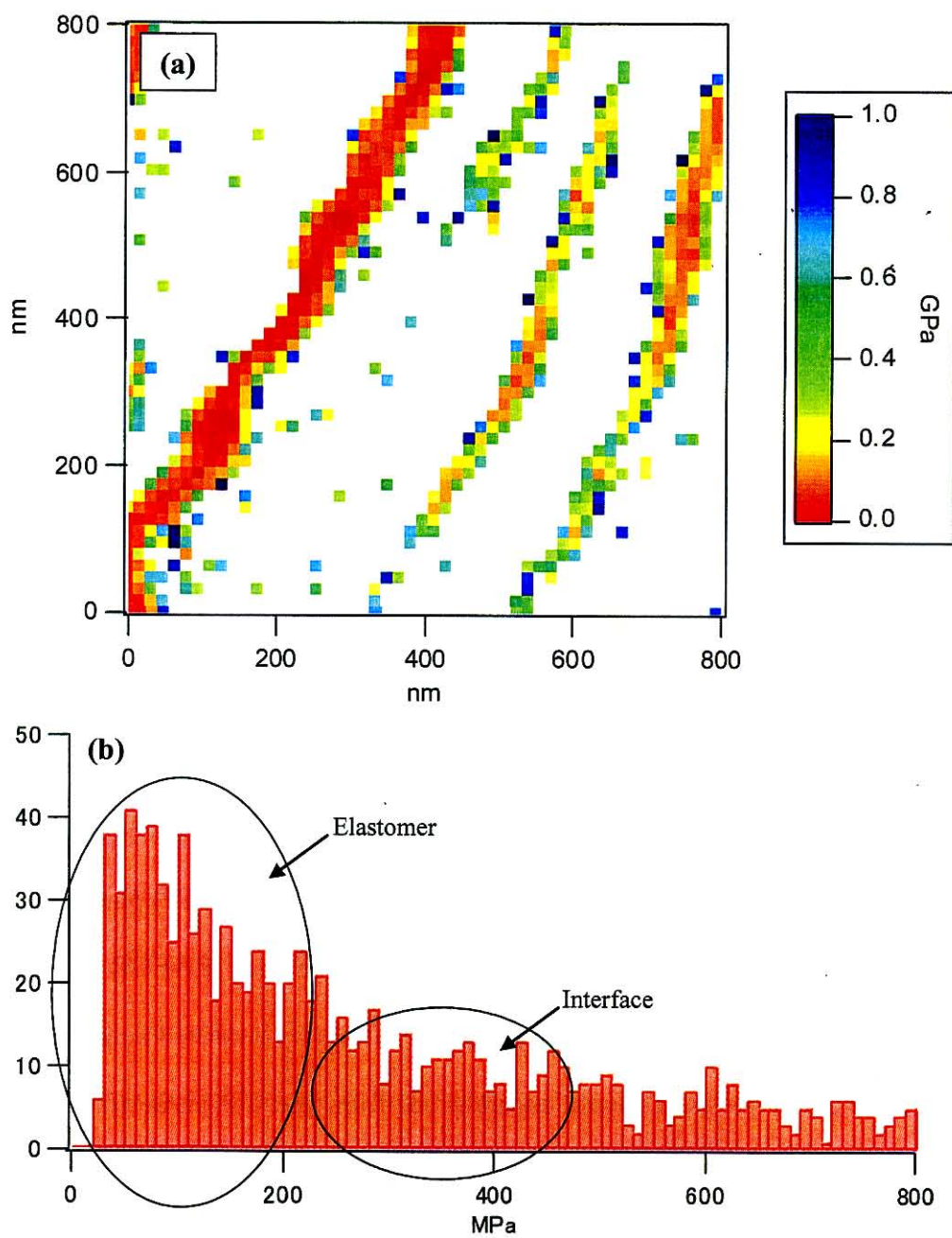
Figure 5: Elastic modulus distribution of the injection blend without annealed. (a) mapping image and (b) the corresponding histogram.
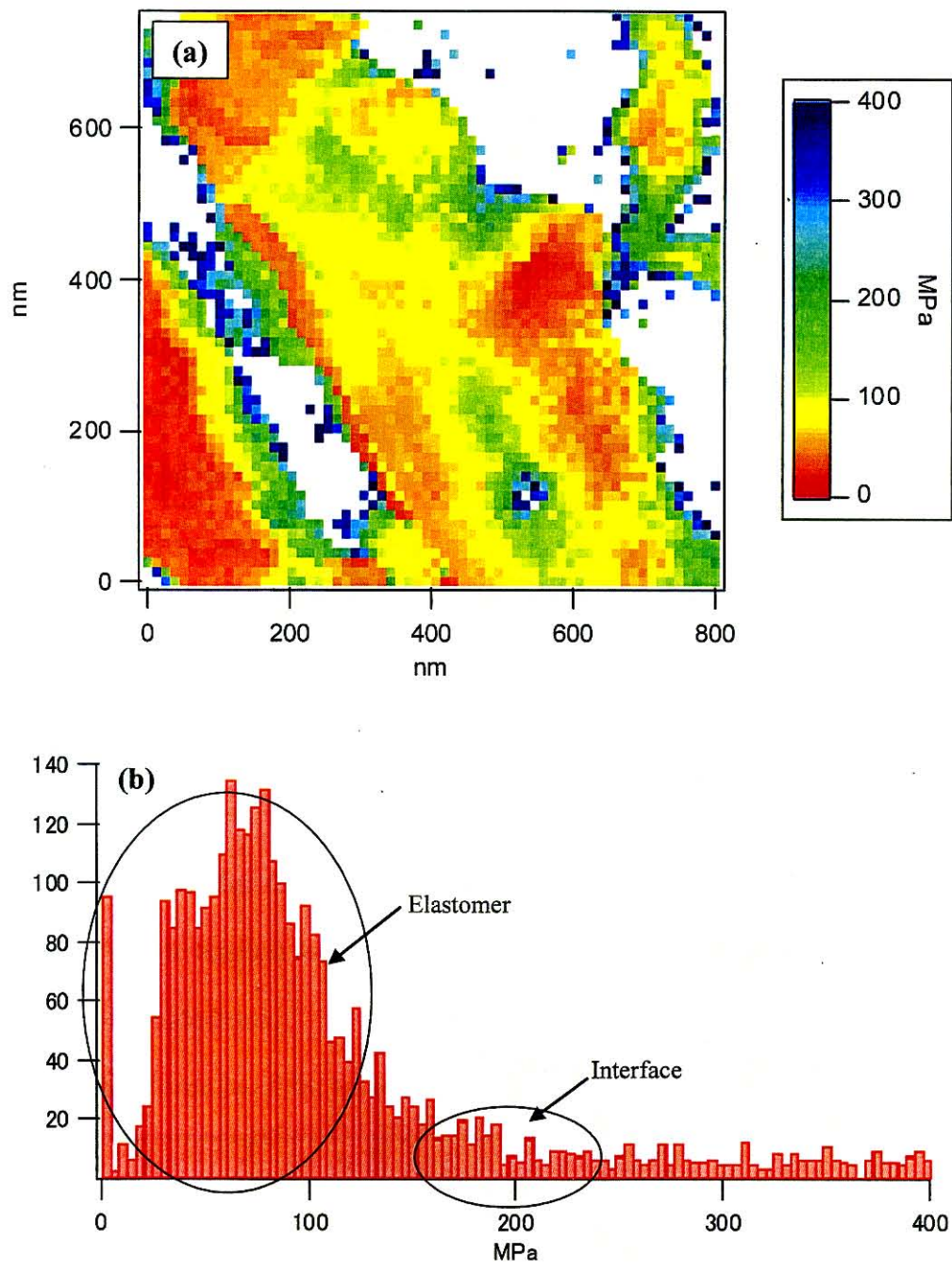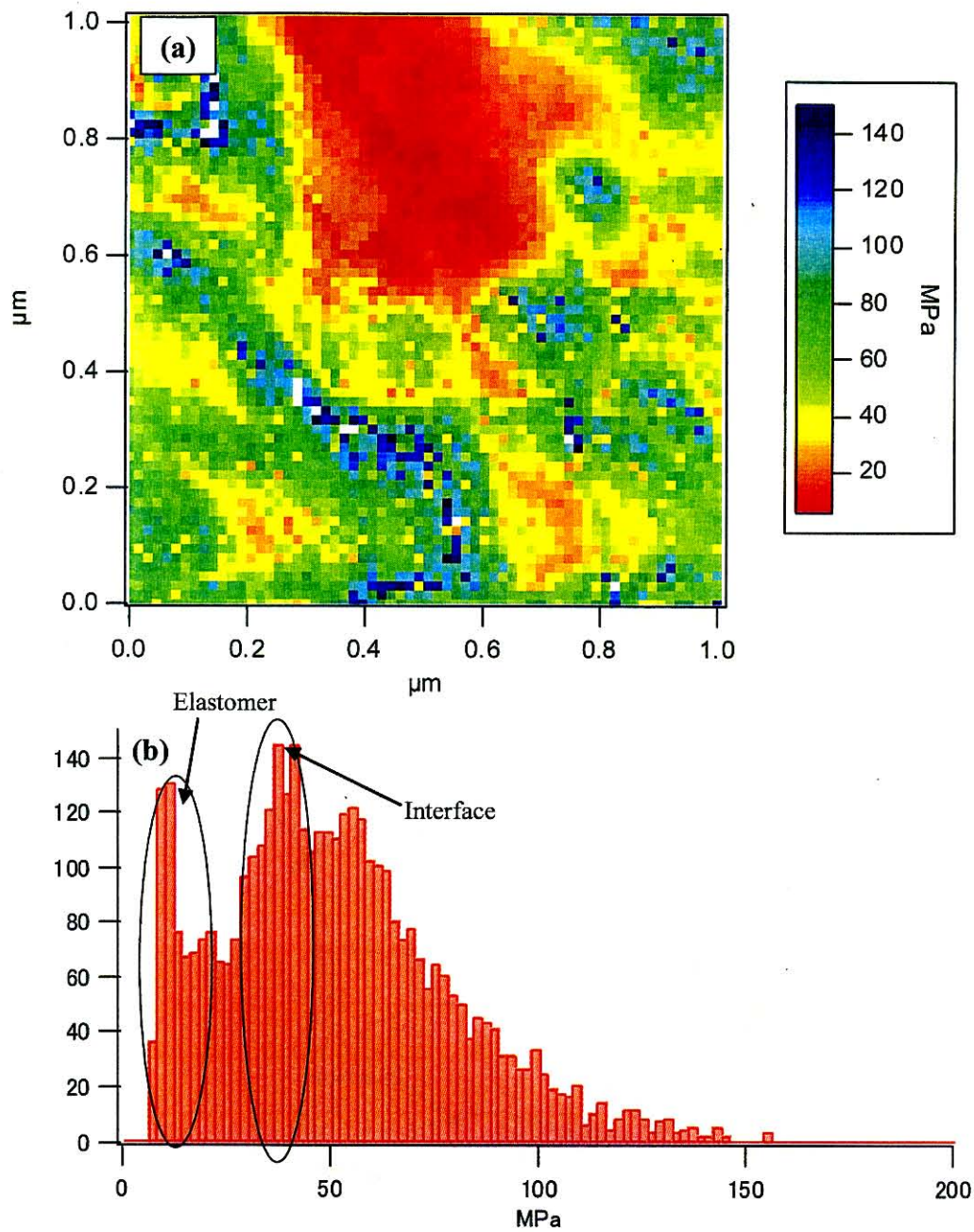
Figure 6: Elastic modulus distribution of the injection blend annealed at 100 °C. (a) mapping image and (b) the corresponding histogram.

Figure 7: Elastic modulus distribution of the injection blend annealed at 155 °C. (a) mapping image and (b) the corresponding histogram.

4-3. Correlation of nano-scale elastic modulus with CLTE behavior:

The above results reveal that the local elastic moduli of the EOR domains as well as the matrix change with the shape of the EOR domains, and with the thermal history of the specimen. In this section, we will investigate how such local change in the physical property could have an influence on the bulk property, the CLTE in this study.

4-3-1. Correlation of the difference in the nano-physical property by the shape of the EOR domain with the CLTE behavior:

Figure 8 shows the CLTE behavior of the injection (fibrous EOR) and the compression (spherical EOR) specimen. Both specimens were annealed at 100 °C before CLTE measurement. The CLTE of the injection is suppressed to be lower value at every temperature than that of the compression.

As indicated in Figs. 2-3, the elastic modulus inside the EOR for the injection-molded specimen exhibited much higher value and broader distribution compared with that for the compression one. In other words, the taut EOR molecules having the higher tension would exist more in the injection-molded blend than in the compression-molded one.

Another formula of the tension by the entropic elasticity is given by equation (12)

$$f = -T\left(\frac{\partial S}{\partial l}\right)_{T,V} \cong T\left(\frac{\partial f}{\partial T}\right)_{l,V} \qquad (12)$$

where S, l and V denote entropy, length and volume. Hence, the tension which is responsible for a recovery strain increases with temperature increase.

In this case, the tension (the recovery strain), which could make the dimension of specimen shrink, would exert more strongly in the injection blend than in the compression one. Hence, the difference in the CLTE behavior between the two blends

would reflect on the difference in recoverable force based on the rubber-elasticity.
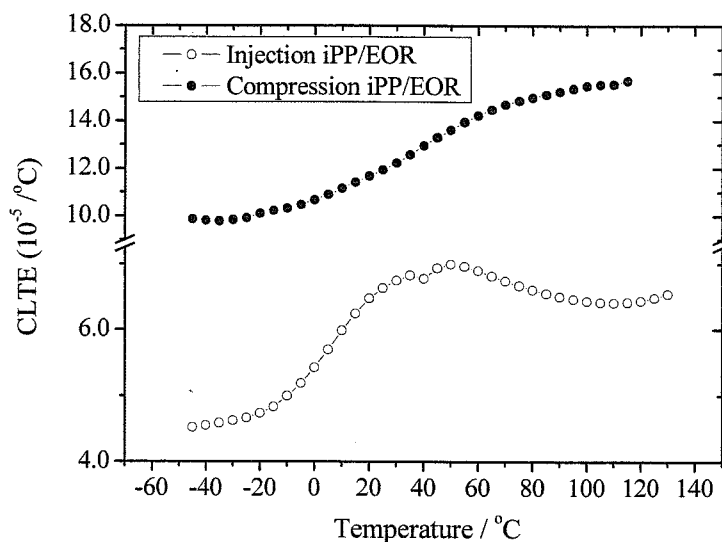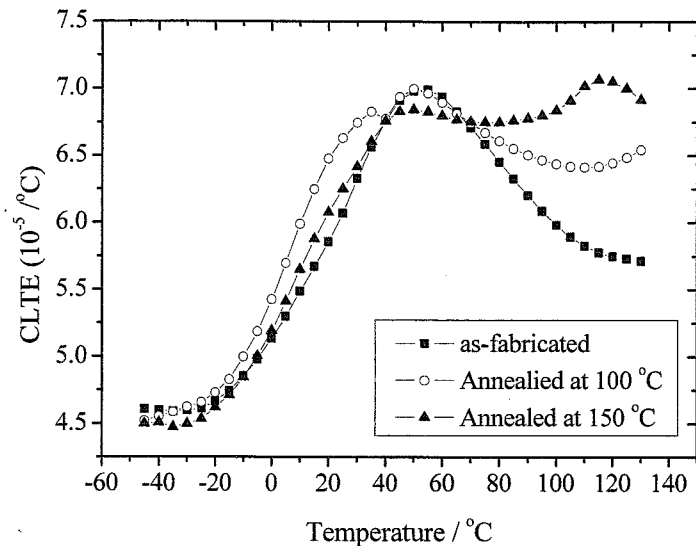

Figure 8: CLTE behavior of (a) injection-molded specimen and (b) compression-molded specimen. Both are annealed at 100 °C before use.

4-3-2. Relationship between the nano-physical property and the CLTE behavior of the injection-molded specimen with different thermal history;

Figure 9 shows the CLTE behavior annealed at various annealing temperatures. An inflection point around 50 °C, which corresponds to the T_m of EOR, is observed in all cases. Before this temperature, the CLTE monotonically increases, and no major difference in the CLTE behavior is found in spite of changing the thermal history. Above this temperature, the CLTE begin to decrease. The as-fabricated specimen exhibits the largest CLTE decrease, and in the specimen annealed at 155 °C the CLTE

levels off instead of decreasing.

Figure 9: CLTE behavior of the injection-molded specimen with different annealing temperature; (a) as-fabricated, (b) annealed at 100 °C and (c) at 155 °C.

To understand the CLTE behavior above the inflection point, the difference in the rubber-elastic effect is also applicable to this case by taking the difference in the local stress accumulated inside the EOR domains in the specimens with different thermal history into consideration.

In the EOR domains in the as-fabricated specimen as seen in Fig. 5, the distribution of the elastic modulus in the EOR is broader, and very high modulus (stress) area with 400 MPa can be observed, which would be caused by highly elongated molecular chains upon injection-molding. As increasing the annealing temperature (Figs. 6-7), the modulus distribution becomes narrower with decrease in the high stress area. The stress relaxation by the rubber-elastic effect is operative more effectively at higher temperature [30].

It is not clear at present that the reason why no difference in the CLTE is found below 50 °C in spite that the rubber-elastic effect might be operative even at the temperature below 50 °C which is above the Tg of EOR (-50 °C). One plausible factor for it is the arrays of the EOR domains with stacking lamella-sheet along ND (Chaps. 2-5), by which the motion of the EOR would be restricted at low temperatures due to being surrounded by the rigid iPP matrix.

5. Conclusions

In this Chapter, we investigated the local elastic modulus of the iPP/EOR blend by the AFM. It was found that the local elastic modulus in the EOR was greatly dependent on the shape of the EOR domains. In addition, the annealing treatment on the injection specimen had a great influence on the elastic modulus distribution not only in the EOR domains but also in the iPP matrix. The difference in the CLTE behavior between the injection and compression specimens or between the injection specimens with different annealing treatments was reasonably understood by taking the difference in the local stress accumulated inside the EOR domains into consideration.

6. References

[1] Magonov S.N., Elings V. and Padkov V.S.; *Polymer*, 1997, **38**, 227

[2] Pearce R. and Vansco J.; *Polymer*, 1998, **39**, 1237

[3] Sikes H.D. and Schwartz D.K.; *Science*, 1997, **278**, 1604

[4] Magonov S.N. and Godovsky Y.K.; *Am. Lab.*, 1998, **30**, 15

[5] Jia Y and Schäffer T.E.; *Langmuir*, 2004, **20**, 10038

[6] Lemieux M., Usov D., Minko S., Stamm M., Shulha H. and Tsukruk V.V.;
Macromolecules, 203, **36**, 7244

[7] Haga H., Sakai S., Kawabata K., Ito E., Ushiki T. and Sanbongi T.; *Ultramicroscopy*,
2000, **82**, 253

[8] Sun Y., Akhremitchev B.B. and Walker G.L.; *Langmuir*, 2004, **20**, 5837

[9] Chong A.C. and Lam D.C.C.; *J. Mater. Sci.*, 1999, **14**, 4103

[10] Nukaga H., Fujinami S., Watabe H., Nakajima K. and Nishi T.; *Jpn. J. Appl. Phys.*,
2005, **3B**, 5425

[11] Nakajima K., Kawaguchi H., Lee J.C., Kageshima M., Ikehara T. and Nishi T.;
Jpn. J. Appl. Phys., 1997, **36**, 3850

[12] Fujinami S., Nukaga H., Nakajima K. and Nishi T.; *Hyomen Kagaku*, 2006, **27**, 530

[13] Rixman M., Dean D., Macias C. and Ortiz C.; *Langmuir*, 2003, **19**, 6202

[14] Ortiz C. and Hadziioannou G.; *Macromolecules*, 1999, **32**, 780

[15] Al-Mawaali S., Bemis J., Akhremitchev B.B., Janesko B. and Walker G.C.;
J. Phys. Chem., 2001, **105**, 3965

[16] Pavoor P.V., Bellare A., Storm A., Yang D. and Cohen R.E.; *Macromolecules*, 2004,
37, 4865

[17] Vanlandingham M.R., Mcknight S.H., Plamese G.R., Elings J.R., Huang X., Bagetti T.A., Edujee R.F. and Gillespe J.W.; *J. Adhesion*, 1997, **64**, 31

[18] Akhremitchev B.B. and Walker G.C.; *Langmuir*, 1999, **15**, 5630

[19] Nakajima K., Fujinami S., Nukaga H., Watabe H., Kitano H., Ohno N., Kaneko M. and Nishi T.; *Kobunshi Ronbunshu*, 2005, **62**, 476

[20] Cappella B., Kaliappan S.K. and Sturm H.; *Macromolecules*, 2005, **36**, 1874

[21] Tomasetti E., Legras R. and Nysten B.; *Nanotechnology*, 1998, **9**, 305

[22] Hertz H.; *J. Reine. Angew. Math.*, 1882, **92**, 156

[23] Johnson K.L, Kendall K. and Roberts A.D.; *Proc. R. Soc. London, Ser. A*, 1971, **324**, 301

[24] Kubo R.; *"Gomu Dansei (Rubber Elasticity)"*, Shokabo Pub. Co. Ltd., Tokyo, Japan, 1948

[25] Lee J.K., Lee J.H., Lee K.H. and Jin B.S.; *J. Appl. Polym. Sci.*, 2001, **81**, 695

[26] Inaba N., Sato K., Suzuki S. and Hashimoto T.; *Macromolecules*, 1986, **19**, 1690

[27] Inaba N., Yamada T., Suzuki S. and Hashimoto T.; *Macromolecules*, 1988, **21**, 407

[28] Sano H., Yui H., Li H.and Inoue T.; *Polymer*, 1998, **21**, 5265

[29] Huang C.I., Chang C.P., Shimizu K. and Han C.C.; *J. Polym. Sci., Part B: Polym. Phys.*, 2004, **42**, 2995

[30] Anthony R.L., Caston R.H. and Guth E.; *J. Phys. Chem.*, 1942, **46**, 826

7. Acknowledgement

Chapter 8:

Conclusions

In this thesis, the studies on the anisotropy in the linear thermal expansion coefficient for isotactic polypropylene (iPP) and thermoplastic elastomer (TPE) binary blends were collected.

In Chapter 2, using iPP and poly(ethylene-*co*-octene) rubber (EOR) blend as a typical rubber toughened iPP blend, the CLTE behavior was reported. In the injection-molded iPP/EOR blend, large anisotropy in the CLTE was observed; low CLTEs both along flow- (FD) and transverse-to-flow direction (TD) while high CLTE along normal-to-flow direction (ND). The EOR domains were arranged as lamella-like sheets stacked normal to ND. In addition to it, large crystal axis orientation was found; b-axis with high thermal expansion was exclusively oriented to the ND. The effect both of the arrays of the EOR domains and the crystal axis orientation cooperatively induced the CLTE anisotropy.

In Chapter 3, three-dimensional structures of the EOR domains were confirmed to be lamella-like sheets in shape using transmission electron microtomography (TEMT). Irregular structures with wavy or broken bands were observed more frequently along TD compared with FD, which would lead to a bit higher CLTE in TD than that in FD.

In Chapter 4, the difference in the CLTE anisotropy depending on the array of the EOR domain was described using various injection-molded iPP/EOR blends consisting

189

of EOR (fixed) as an elastomer and various iPP materials with different viscosities. The arrays of the EOR domains were controlled by changing viscosity ratio of EOR to iPP, and as the viscosity ratio increases, the arrays changed to be spherical to lamella-like sheets. The blend with the lamella-like sheet arrays showed the largest CLTE anisotropy whereas the one with the spherical arrays showed no anisotropy thus isotropic CLTE. The WAXD pole figure analysis revealed that in the blend with the lamella-sheet arrays, c- and b-axis oriented exclusively to the FD and the ND, respectively. On the other hand, the blend with the spherical arrays showed no crystal axis orientation. The anisotropy of the CLTE in terms of the lamella-sheet array blend was estimated by introducing the effect of the crystal axis orientation and the retraction due to minimizing the interfacial tension at elevated temperatures.

In Chapter 5, the correlation of the CLTE anisotropy with the chemical composition of TPE to be combined with iPP was reported using various injection-molded iPP and TPE blends comprising the iPP (fixed) and various ethylene-based TPEs with different chemical compositions. The CLTE anisotropy, in particular, the CLTE in FD, was greatly dependent just on the co-unit content of the TPE not on its chemical composition. The blend with the TPE having higher co-unit content exhibited lower CLTE in FD. Hence, the correlation of the compatibility between the iPP and the TPE with the CLTE in the FD was firstly clarified. According to this context, POM and DMTA analysis revealed that the allocation of the iPP amorphous regions as a result of spinodal decomposition played an important role on the CLTE in FD.

In Chapter 6, real-time morphological change in iPP/EOR blend at variable temperatures was observed using an atomic force microscopy (AFM) with a heater accessory. Two types of the blends fabricated by different methods, the injection- and

the compression-molding were employed, and their morphologies by the AFM phase image were compared. The injection blend (Blend-I) with fibrous EOR morphology showed an abnormal morphological change in the iPP matrix phase; the crystalline area began to increase while the amorphous area to decrease above 40 $^\circ$C, and it was facilitated further at elevated temperatures, resulting in almost no phase image contrast at 100 $^\circ$C. The SAXS and DSC analysis revealed the surface melting of imperfect crystallites resulting from rapidly cooling during the injection-molding would occur in the Blend-I. The surface melting would reduce the difference in the adhesive force between the crystal and the amorphous regions, thus giving rise to disappearance of the phase image contrast at higher temperatures.

In Chapter 7, the local elastic modulus and its distribution in the iPP/EOR blend was investigated using the AFM technique. The elastic modulus in the EOR was greatly dependent on the shape of the EOR domains and the thermal history of the specimens. The difference in the CLTE behavior between the injection and compression specimens or between the injection specimens with different annealing treatments was reasonably understood by taking the difference in the local stress accumulated inside the EOR domains into consideration.

List of Publications

Chapter 2; "Anisotropy in Thermal Expansion in Rubber Toughened Polypropylene –

Injection Molded System –"

Ono M., Washiyama J., Nakajima K. and Nishi T.

Polymer J., 2004, **36**, 563-566

Chapter 3; "Study on Three dimensional Structures in Injection-molded

iPP/Ploy(ethylene-*co*-octene) by Transmission Electron Microtomography"

Ono M., Nishioka H., Jinnai H., Nakajima K. and Nishi T.

e-Journal Soft Mater., 2006, **2**, 56-61

Chapter 4; "Anisotropic Thermal Expansion in Polypropylene/Poly(ethylene-*co*-octene)

Binary Blends: Influence of Arrays of Elastomer Domains"

Ono M., Washiyama J., Nakajima K. and Nishi T.

Polymer, 2005, **46**, 4899-4908

Chapter 5; "Filler-less Polypropylene/Elastomer Blends with Extremely Low Thermal Expansion"

Ono M., Nakajima K. and Nishi T.

Kautschuk Gummi Kunstsoffe, 2006, **11-06**, 574-581

J. Appl.Polym.Sci., (Submitted)

Chapter 6; Manuscript in preparation

Chapter 7; Manuscript in preparation

Acknowledgement

The studies collected in this thesis were carried out at Professor Nishi laboratory at Graduate School of Polymeric & Organic materials of Tokyo Institute of Technology during 2004 to 2007. It was the year 2003 when the author had started to co-develop these studies with Professor Nishi. Looking back on that time up to now, the author can't get off his mind that his studies were accomplished thanks to many people.

Firstly, the author expresses his deep gratitude to Professor Toshio Nishi for helpful suggestions, useful discussions, magnificent supervision and critical reading of the manuscript. His gentle looking and positive encouragement has made the author relieved whenever the author was depressed. The author is sincerely grateful to Dr. Ken Nakajima of the above laboratory for his invaluable suggestions, fruitful discussions and sincere encouragement. He gave polite instructions on the AFM measurements, techniques and theories to the author, an utter beginner of AFM. Without his advice, the author couldn't complete these studies, in particular, the studes in Chapters 6-7. The author would like to express his deep gratitude to Associate Professor Hiroshi Jinnai at Graduate School of Kyoto Institute of Technology for helping the TEMT measurement in Chapter 3 in this thesis and strictly reviewing the manuscript concerning Chapter 3.

Special thanks must be given to all the members of Nishi Laboratory from 2004 up to now. In particular, Dr. So Fujinami, with whom the author is contemporary and thus shared a lot, always helped the author with many things including the AFM